Structures and properties of liquid crystals and related molecules from computer simulation

Cheung, David Lai Gwai

Structures and Properties of Liquid Crystals and Related Molecules from Computer Simulation

David Lai Gwai Cheung

Ph.D. Thesis

University of Durham

Chemistry Department

October 2002

Submitted in partial fulfilment of the requirements
for the degree of Doctor of Philosophy

Abstract

Structures and Properties of Liquid Crystals and Related Molecules from Computer Simulation

David Lai Gwai Cheung

Computer simulations provide a powerful tool for the investigation of liquid crystalline phases. In this thesis the ability of simulations to calculate accurately the values of material parameters of liquid crystal molecules is investigated.

An all-atom force field for liquid crystal molecules is developed using first principles density functional theory calculations on small organic molecules, which encompass key structural features of a range of common liquid crystalline molecules. Molecular dynamics simulations of these 'fragment' molecules are carried out in the liquid phase to test the force field parameters by determining densities and heats of vapourisation. Good agreement is found between experimental values and those calculated from simulation.

Equilibrium molecular dynamics (MD) calculations were then performed for the nematogen *n*-4-(trans-*n*-pentylcyclohexyl)benzonitrile (PCH5). These simulations were performed using a fully atomistic model for several temperatures. The MD trajectories were used to obtain densities, order parameters, and values for the rotational viscosity coefficient γ_1. Several methods of obtaining γ_1 were tested based on the director angular velocity correlation function, the director mean-squared displacement, and statistical mechanics methods based on the rotational diffusion model. Good agreement is obtained between experimental values of γ_1 and those found from simulation.

Further MD simulations of PCH5 using a 216 molecule system and the force field derived in this thesis were carried out to calculate the flexoelectric coefficients e_s and e_b for PCH5. The temperature dependence of e_s and e_b was examined along with

the separate contributions to e_s and e_b arising from the electrostatic and van der Waals interactions. The calculated values of e_s and e_b are consistent with available experimental data. The van der Waals and electrostatic contributions are found to be of similar magnitude and opposite sign.

Declaration

The material contained within this thesis has not previously been submitted for a degree as the University of Durham or any other university. The research within this thesis has been conducted by the author unless indicted otherwise.

David Lai Gwai Cheung

October 2002

Acknowledgments

There are a great many people and organisations who have helped me during the three and a bit years of my research. Firstly I would like to thank the UK Engineering and Physical Sciences Research Council for the provision of a postgraduate studentship. I would also like to thank the EPSRC for grants toward the provision of the high power computers used throughout this work. I am greatly indebted t the University of Durham, the British Liquid Crystal Society, and the Royal Society of Chemistry for providing funds to attend many conferences during my Ph.D., providing valuable opportunities for interaction with fellow researchers. I would also like to thank Prof. Mikhail Osipov (Strathclyde) and Prof. Friederike Schmid (Bielefeld) for advice and conversations about my work.

Academically there are many people I have become indebted to. This work would not have been possible without the help and encouragement of my supervisors, Dr Mark Wilson and Dr Stewart Clark. I would also like to thank Dr Lydia Heck for assistance in all matters computational, as well as the staff of the University of Durham Information Technology Service. A big thank you is owed to my colleagues past and present in the Computational Chemistry group and the Condensed Matter Theory Group for helpful advice and stimulating discussions. I would especially like to thank Lorna Stimson for being an absolute gem throughout my time in Durham.

Finally on a more personal note I would like to thank my family for their love and support throughout my study. I am indebted to Dave and Cath, and Rich, for providing various beds and floors during the final stage of writing up and everyone else who have made my time in Durham a time to be treasured. And last, and certainly not least, I would like to thank Wendy for all her love, support, and friendship.

Nothing amuses more harmlessly than computation, and nothing is oftener applicable to real business or speculative enquiries

Samuel Johnson, 1783

As long as there were no machines, programming was no problem at all; when we had a few weak computers, programming became a mild problem and now that we have gigantic computers, programming has become an equally gigantic problem. In this sense the electronic industry has not solved a single problem, it has only created them—it has created the problem of using its product.

Edsger W. Dijkstra, 1972

Contents

List of Figures

List of Tables

Chapter 1

Introduction to Liquid Crystals

1.1 Introduction

For many years matter was thought to exist in three phases: solid, liquid, and gas. However, this picture is not entirely correct. Certain materials, mostly organic, do not have a single solid to liquid translation. Instead they show one or more intermediate phases. These phases are called *liquid crystalline* phases, or *mesomorphic* phases (*mesophases*). These show features intermediate between those of a crystalline solid and a liquid. In a crystal the molecules are located at regular points in space; there is translational order. In a liquid this translational ordering of molecules does not exist. Mesophases may be obtained in two different ways. First the translational order can be confined to one or two dimensions rather than three dimensions, resulting in a *smectic phase*. Alternatively, for non-spherical molecules molecular orientations may be considered. Translational order may be retained but the molecular orientations become disordered, resulting in a *plastic crystal* or the translational order may be lost and the orientational order retained, resulting in *nematic* phase.

The liquid crystalline state has been known for over one hundred years [1]. Its discovery is generally credited to Friedrich Reinitzer. Reinitzer noted that cholesteryl

benzoate had two melting points [2]; at the first the crystal melted into a cloudy liquid and at the second the liquid became clear. Another key moment in the history of liquid crystals was George Friedel's work on the classification of liquid crystal phases [3]. This marked the acceptance of liquid crystals as a separate phase of matter, distinct from the liquid and crystalline phases from which it gets its name. He also introduced the term *mesophase* (meaning 'in-between' phase) as an alternative name for liquid crystal phases and the term *mesogen* for the molecules that form these phases.

1.2 Liquid Crystal Phases

Liquid crystal phases are formed by a wide variety of molecules [4]. They can be divided into two classes, thermotropic and lyotropic. Transitions to thermotropic phases are initiated by changes in temperature, while those to lyotropic phases can also be initiated by changes in concentration.

1.2.1 Thermotropic Phases

Thermotropic liquid crystals can generally be formed by prolate (calamitic) molecules or oblate (discotic) molecules. Liquid crystal phases formed by calamitic molecules fall into three different categories: nematic, chiral nematic, and smectic.

Nematic Liquid Crystal Phase

The simplest liquid crystal phase is called the nematic phase (N). It is characterized by a high degree of long range orientational order but no translational order. Molecules in a nematic phase spontaneously order with their (for calamitic molecules) long axes roughly parallel. A schematic diagram of a nematic phase is shown in Fig. 1.1. An uniformly aligned nematic has a preferred direction, often described in terms of a unit vector called the director, $\mathbf{n}$. More generally a bulk

nematic will contain domains. The orientation of the director is constant in each domain but is different in different domains. Viewed under a polarizing microscope the defect regions linking these domains appear as dark threads [5]

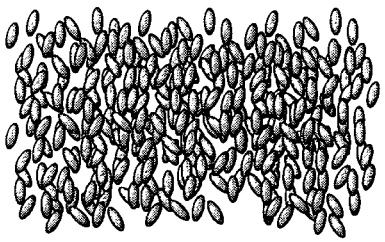

Figure 1.1: Schematic diagram of a nematic liquid crystal

Chiral Nematic Liquid Crystal Phase

Chiral molecules can also form nematic phases called chiral nematic (or cholesteric) phases (N*). This phase shows nematic ordering but the preferred direction rotates throughout the sample. The axis of this rotation is normal to the director. An example of this is shown in Fig. 1.2. The distance over which the director rotates by 360° is called the chiral pitch and is generally of the order of hundreds of nanometres, the wavelength of visible light. A non-chiral nematic phase can be thought of as a chiral nematic with an infinite pitch.

Smectic Liquid Crystal Phases

Smectic phases have further degrees of order compared to the nematic phase. In the simplest smectic phase, the smectic-A (SmA) phase, the molecules order into layers, with the layer normal parallel to the director. Within the layers, liquid like structure remains, as shown in Fig. 1.3.

Closely related to the SmA phase is the smectic-C (SmC) phase. Here the molecules form a layer structure but the long axes of the molecules, and hence the director, lies at an angle to the layer normal, as shown in Fig. 1.4. There are many

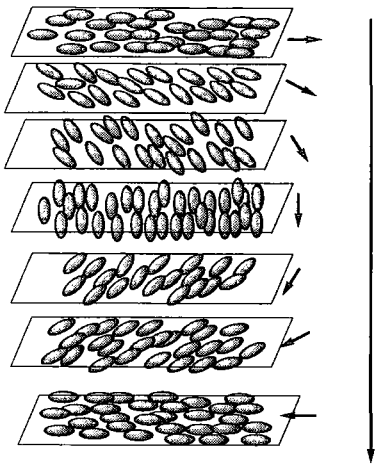

Figure 1.2: Schematic diagram of a chiral nematic liquid crystal

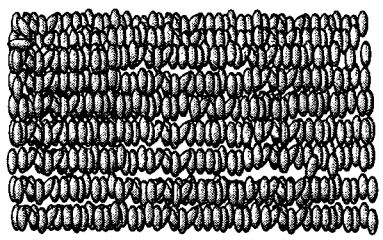

Figure 1.3: Schematic diagram of a smectic-A liquid crystal

other smectic phases which have long range order within the layers [6]. Smectic phases can also be formed by chiral molecules, leading to chiral smectic phases.

Discotic Liquid Crystal Phases

Liquid crystal phases formed by discotic molecules fall into three different categories: discotic nematic, discotic chiral nematic, and columnar [7]. The discotic nematic is similar in structure to the calamitic nematic, although in this case the short axes of the molecules tend to lie parallel. The same holds for the discotic chiral nematic phases.

Columnar phases are the discotic equivalent of the smectic phase. Here the

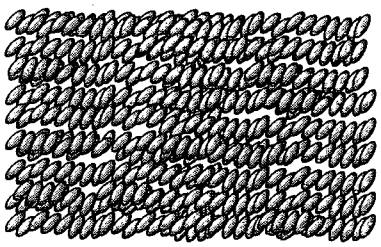

Figure 1.4: Schematic diagram of a smectic-C liquid crystal

molecules form columns. In the simplest case the short axes of the molecules lie parallel to the axis of the column and the columns are randomly distributed in space. More complicated discotic phases exist, where the short molecular axes lie at an angle to the column and translational order exists between the columns, analogous to the more complicated smectic phases.

Other Thermotropic Phases

Most of the phases exhibited by low molecular mass liquid crystals are described above. Recently however there has been much interest in the so-called 'banana' phases formed by bent-core molecules [8]. Some of these phases are chiral although the molecules forming them are achiral.

Some high molecular mass polymers, liquid crystalline polymers (LCP), can also form liquid crystal phases [9]. These fall into two categories depending on where the mesogenic part of the molecule is located. If the mesogenic unit is contained within the main polymer chain then it is termed a main chain liquid crystal polymer (MCLCP). If it is attached to a side chain of the polymer then it is termed a side chain liquid crystal polymer (SCLCP). As well as depending on the nature of the mesogenic core, the mesophases formed by these materials are dependent on the flexibility of the polymer backbone and (for SCLCP's) the side chain.

Closely related to LCP's are dendritic liquid crystals [10, 11]. These molecules consist of a central core with the mesogenic units attached to flexible spacers that

radiate out from the core.

1.2.2 Lyotropic Liquid Crystal Phases

Lyotropic liquid crystal phases are formed by amphiphilic molecules [12]. These often consist of a polar head group attached to one or more non-polar chains and are often known as *surfactants* (surface active agents). A schematic is shown in Fig. 1.5. When these are dissolved in an appropriate solvent they self-assemble so the polar (hydrophilic) heads protect the non-polar (hydrophobic) tails. These structures are known as micelles. At low surfactant concentrations these are roughly spherical, as shown in Fig. 1.6. As the surfactant concentration increases then other phases are formed [13]. These include the hexagonal phase where the amphiphiles form cylinders that pack in a hexagonal array and the lamellar phase where the amphiphiles form a bilayer structure.

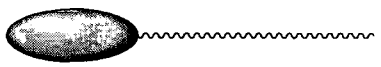

Figure 1.5: Schematic diagram of an amphiphilic molecule

1.3 Liquid Crystal Order

For the simplest liquid crystal phase, the nematic phase, the order can be characterized in terms of a preferred direction and a degree of order. The preferred direction is usually denoted by a unit vector called the director $\mathbf{n}$. The degree of order is denoted by an order parameter, $\bar{P}_2$, which takes on a value between 0 for a completely disordered phase and 1 for a completely ordered phase. These are commonly found from the second rank ordering tensor [14]

$$Q_{\alpha\beta} = \frac{1}{N_m}\sum_{i=1}^{N_m}\left(\frac{3}{2}\hat{u}_{i\alpha}\hat{u}_{i\beta} - \frac{1}{2}\delta_{\alpha\beta}\right), \ \alpha,\beta = x,y,z, \tag{1.1}$$

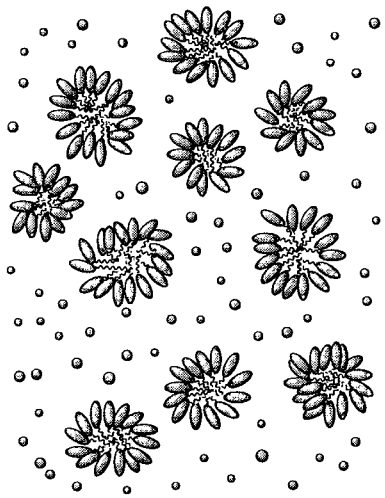

Figure 1.6: Schematic diagram of micelles.

where $\hat{\mathbf{u}}_i$ are the long axis of the molecule, N_m is the number of molecules, and $\delta_{\alpha\beta}$ is the Kronecker delta function. $Q_{\alpha\beta}$ is symmetric and traceless. Diagonalization of $Q_{\alpha\beta}$ gives three eigenvalues λ_+, λ_0 and λ_- (with $\lambda_+ > \lambda_0 >= \lambda_-$) which sum to zero. For an uniaxial system the eigenvalues are related by

$$\lambda_- = \lambda_0 = -\frac{1}{2}\lambda_+. \tag{1.2}$$

$\mathbf{n}$ is then given by the eigenvector associated with λ_+ and conventionally $\bar{P}_2 = \lambda_+$. Alternatively, the order parameter can be defined as $\bar{P}_2 = -2\lambda_0$ [15]. This is useful in the vicinity of a phase transition as the first definition gives small positive values of $\bar{P}_2$ in the isotropic phase (of the order of $1/\sqrt{N}$) while the second gives values that fluctuate about 0.

An alternative definition of $\bar{P}_2$ is

$$\begin{aligned} \bar{P}_2 &= \langle P_2(\mathbf{n}.\mathbf{u})\rangle \\ &= \langle P_2(\cos\theta)\rangle \\ &= \left\langle \frac{3}{2}\cos^2\theta - \frac{1}{2}\right\rangle \end{aligned} \tag{1.3}$$

where $\theta = \mathbf{n}.\hat{\mathbf{u}}$ is the angle between the molecular axis and the director and $P_2(x)$

is the second Legendre polynomial. In (1.3) the angled brackets denote an average over all molecules. The definition of $\bar{P}_2$ in terms of a Legendre polynomial allows the definition of other order parameters corresponding to the other Legendre polynomials.

A more complete description of the order in a nematic phase can be obtained from the orientational distribution function (ODF). This function gives the probability of finding a molecule at a certain angle to the director. An example is shown in Fig. 1.7.

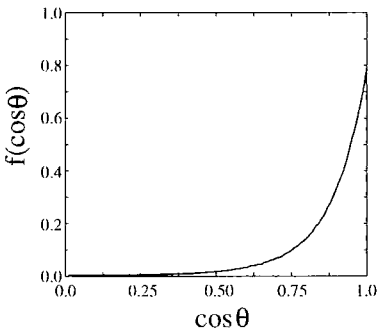

Figure 1.7: Orientational distribution function for a nematic liquid crystal. Here the ODF is plotted as a function of $\cos\theta$, where θ is the angle between the molecular axis and the director.

Like any function the ODF can be expanded in terms of a complete set of orthogonal functions. Expanding it in terms of Legendre polynomials gives [16]

$$\begin{aligned} f(\cos\theta) &= \sum_l c_l P_l(\cos\theta) \\ &= \sum_l \frac{2l+1}{2} \bar{P}_l P_l(\cos\theta) \end{aligned} \tag{1.4}$$

where $\bar{P}_l$ are the order parameters. Thus knowledge of the ODF in principle provides the order parameters. For non-ferroelectric nematics the ODF is symmetric about 0. Thus, the odd terms in the expansion in (1.4) are zero and hence so are the odd order parameters.

A typical plot of the temperature dependence of the order parameter is shown in Fig. 1.8. At the low end of the nematic range $\bar{P}_2$ generally takes a value of about 0.7-0.8. As the temperature is raised it falls to a value of about 0.3-0.4 just above the nematic-isotropic transition. It then drops discontinously to 0 at the transition.

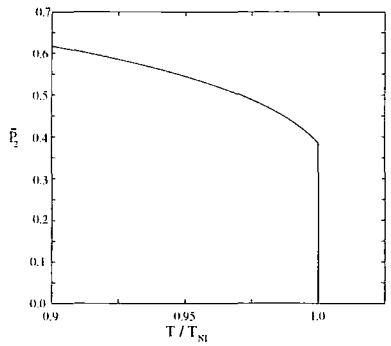

Figure 1.8: Typical temperature dependence of the nematic order parameter $\bar{P}_2$ with temperature. T_{NI} is the nematic-isotropic transition temperature.

The description of order in a chiral nematic phase is the same as that for a nematic with the additional feature that the preferred direction, the director $\mathbf{n}$, rotates in space. If the axis of rotation of $\mathbf{n}$ is taken to be along the z direction then $\mathbf{n}$ can be written as

$$\mathbf{n}(z) = \left(\cos\left(\frac{2\pi}{\lambda}z\right), \sin\left(\frac{2\pi}{\lambda}z\right), 0\right) \tag{1.5}$$

where λ is the chiral pitch.

Additional order parameters appear for smectic phases. In the Sm-A phase it is necessary to introduce a translational order parameter to describe the ordering into layers. For Sm-C phases a tilt order parameter appears, which can just be the average tilt angle for the molecules.

As the order parameters are key properties for identifying different mesophases, there has been much interest in determining them from experiment. Common methods for determining $\bar{P}_2$ include birefringence, diamagnetic, and dielectric measurments and NMR spectroscopy [17]. Raman scattering can be used to determine

$\bar{P}_4$ in addition to $\bar{P}_2$ [17]. It is possible to obtain the entire ODF using X-ray [18] or neutron diffraction [19]. For surfaces and interfaces, where the odd rank order parameters ($\bar{P}_1$, $\bar{P}_3$, etc) may be non-zero, second harmonic generation may be used to determine these [17]. As the chiral pitch in chiral nematic liquid crystals is typically of the order of visible light, it can be measured by scattering of visible light. Translational order in smectic liquid crystals can be examined using X-ray diffraction [16]

1.4 Structure-Property Relationships in Liquid Crystals

Since their discovery considerable work has gone into trying to understand the properties of liquid crystals and how these relate to molecular structure. Despite this there exists only a poor understanding of how changes in molecular structure affect material properties. For liquid crystals this is complicated by several factors. Firstly, liquid crystal phases are formed by materials from the whole spectrum of chemical classes: organic, organometallic, and biological molecules can all form liquid crystal phases. Secondly, mesogenic molecules are generally quite large. A typical low mass mesogen will have from about 40-100 atoms. For liquid crystalline polymers and dendrimers this can be closer to a few thousand atoms. Liquid crystals tend to be flexible. This inhibits crystallization, preventing the direct transition from an isotropic liquid to a crystalline solid. It also leads to a large degree of conformational freedom, so properties are generally determined by more than just the equilibrium structure. Finally liquid crystal molecules often contain disparate parts (such as alkyl and perfluoroalkyl chains) that can have a large effect on the phase behaviour [20]. Investigation of these factors by experimental or theoretical means should hopefully lead to a better understanding of structure-property relationships in liquid crystals.

In principle the relationship between molecular structure and macroscopic properties can be investigated through the synthesis of series of similar mesogenic compounds. This however can be time consuming and may involve many difficult and expensive syntheses. Thus, the ability to determine the properties of a molecular structure before synthesis would be desirable. It is here that simulations can play an important role. Simulations on general molecular models can be used to find features that can lead to a particular property or phase [21]. Atomistic simulations can be used to determine material properties of a particular molecular structure.

1.5 Overview and Scope of Thesis

The aim of this thesis is to determine material properties of a typical nematic liquid crystal from computer simulations. Atomistic potentials have been used throughout. This allows the direct comparison between values of properties calculated from simulation with those found from experimental measurements. Consistency between these results provide confidence that the methods employed are accurate and have the potential to be used for the prediction of these properties.

Chapter 4 describes the derivation of potential functions and parameters from *ab initio* density functional theory calculations. Accurate representation of intra and intermolecular interactions are required for good quality simulations. Specifically for liquid crystals, molecular flexibility in the form of internal rotations plays a highly important role in determining phase behaviour, so much effort has been put into accurately determining parameters for these. The resulting potential functions have been tested using liquid state molecular dynamics simulation and gas phase Monte Carlo simulations to determine thermodynamics properties. These are in good agreement with experiment.

In chapter 5 the rotational viscosity coefficient, γ_1, is calculated by equilibrium molecular dynamics simulations. Several techniques have been employed in this

study. Comparison between these methods and experimental values has been made.

Finally, chapter 6 describes the calculation of the flexoelectric coefficients, e_s and e_b, for a nematic liquid crystal. Despite being important in many areas of liquid crystal phenomonology these are hard to determine from experiment. Thus it is hoped that simulation may provide a route to these, increasingly important, parameters.

A variety of different computational methods have been used in this thesis. The theory of the *ab initio* calculations employed in chapter 4, as well as details of their practical implementation are given in chapter 2. Chapter 3 outlines the theory and practical details of molecular dynamics and Monte Carlo methods used in chapters 4-6 as well as a review of simulations of liquid crystalline systems.

Chapter 2

Electronic Structure Calculations

2.1 Introduction

The aim of an electronic structure calculation is to calculate properties of a system from only the knowledge of the constituent atoms. When done without explicit recourse to experimental data (with the exception of the use of fundamental constants and comparison with experimental results), these can be termed *ab initio* calculations. Most properties of interest can be related to changes in energy of the system of interest. For example, the ground state geometry of a molecule is found from considering the change in energy of a molecule with regard to the change in the positions of the atomic nuclei.

Traditionally electronic structure calculations, using methods such as the wave-function based Hartree-Fock method [22, 23], have found the energy of a system by solving the time-independent Schrödinger equation

$$\left[\sum_{i=1}^{N} -\frac{\hbar^2}{2m_i}\nabla_i^2 + V(\mathbf{r}_1, .., \mathbf{r}_N)\right] \Psi(\mathbf{r}_1, .., \mathbf{r}_N) = E\Psi(\mathbf{r}_1, .., \mathbf{r}_N), \tag{2.1}$$

where N is the number of particles (electrons and nuclei) with position vectors $\mathbf{r}_i$, or symbolically

$$\mathcal{H}(\mathbf{r}_1, ..., \mathbf{r}_N)\Psi(\mathbf{r}_1, .., \mathbf{r}_N) = E\Psi(\mathbf{r}_1, .., \mathbf{r}_N), \tag{2.2}$$

where $\mathcal{H}$ is the Hamiltonian given by

$$\mathcal{H}(\mathbf{r}_1, ..., \mathbf{r}_N) = \left[\sum_{i=1}^{N} -\frac{\hbar^2}{2m_i}\nabla_i^2 + V(\mathbf{r}_1, .., \mathbf{r}_N)\right]. \tag{2.3}$$

Electronic structure calculations have proved useful in many areas of condensed matter physics and chemistry, especially with the rapid growth in computer power. An alternative to wavefunction based methods, *Density Functional Theory* (DFT) has, over the past 20 years, become widely used. DFT provides an (in principle) exact method for calculating the energy of a system of interacting electrons in terms of a set of single electron equations. In certain cases the accuracy of DFT calculations rival those of more computationally demanding quantum chemical calculations [24] and this has seen it become widely used in physics and chemistry, a fact recognized in the award of part of the 1998 Nobel prize in chemistry to Walter Kohn for his work in the development of DFT [25].

This chapter reviews DFT calculations used in Chapter 4 for the calculation of conformational energies of liquid crystal fragments. First, the Born-Oppenheimer approximation is discussed in §2.2. This allows the separation of a problem consisting of the positions of a set of electrons and nuclei into separate electronic and nuclear parts. Next, the DFT method is introduced in §2.3, discussing the Hohenberg-Kohn theorem that provides the justification for using the electron density as the central quantity in electronic structure calculations and the Kohn-Sham equations that provide a route to using DFT in practical calculations. Also briefly discussed are exchange-correlation functionals that allow the Kohn-Sham equations to be written as a set of single electron equations. For numerical and computational calculations the unknown wavefunction and charge density are usually expanded in a set of basis functions and these are discussed in §2.4. For calculations that employ a plane wave basis set, the electron-nuclei interaction is usually treated by pseudopotentials as discussed in §2.5. Finally the implementation of the methods used in this work for the calculation of energies and structures is given in §2.6.

2.2 Born-Oppenheimer Approximation

There is a large difference between the masses of electrons and nuclei. For the simplest nuclei, a single proton, the ratio of nuclei to electron masses is approximately 2000. Due to this, there is a large difference in the timescales of electronic and nuclear motion. This is the motivation for the Born-Oppenheimer approximation. The difference in the masses allows the electrons to respond almost instantaneously to the motion of the nuclei. This allows the separation of the Hamiltonian into nuclear $\mathcal{H}_n$ and electronic $\mathcal{H}_e$ parts

$$\mathcal{H}(\mathbf{r}_1,..,\mathbf{r}_n,\mathbf{R}_1,..,\mathbf{R}_N) = \mathcal{H}_n(\mathbf{R}_1,..,\mathbf{R}_N) + \mathcal{H}_e(\mathbf{r}_1,..,\mathbf{r}_n;\mathbf{R}_1,..,\mathbf{R}_N) \tag{2.4}$$

where $\mathbf{r}_i$ are the electronic coordinates and $\mathbf{R}_I$ are the nuclear coordinates. $\mathcal{H}_e$ depends parametrically on the nuclear coordinates. The wavefunction can then be taken to be the product of the electronic and nuclear parts

$$\Psi(\mathbf{r}_1,..,\mathbf{r}_n,\mathbf{R}_1,..,\mathbf{R}_N) = \Psi_e(\mathbf{r}_1,..,\mathbf{r}_n;\mathbf{R}_1,.,\mathbf{R}_N)\Psi_n(\mathbf{R}_1,..,\mathbf{R}_N). \tag{2.5}$$

This separation of the Hamiltonian into a sum of nuclear and electronic parts and the wavefunction into a product of nuclear and electronic parts allows the separation of the Schrödinger equation. Electronic structure calculations aim to solve the electronic Schrödinger equation (SE) as a function of the nuclear coordinates.

One picture that arises from the Born-Oppenheimer approximation is that of the nuclei moving on a *Potential Energy Surface* (PES) that is a solution to the electronic SE. In principle the PES can be determined from electronic structure calculations although, due to the large number of calculations that would be involved, it is unfeasible to construct global PES from calculations. Instead this tends to be restricted to areas near potential minima.

2.3 Density Functional Theory

The motivation of Density Functional Theory (DFT) [26, 27] is that the ground state properties of a system can be described by considering the ground state charge density. The density can be found from the electronic wavefunction $\Psi(\mathbf{r}_1, \mathbf{r}_2, ..., \mathbf{r}_n)$, by

$$\rho(\mathbf{r}_1) = \int \Psi^*(\mathbf{r}_1, \mathbf{r}_2, .., \mathbf{r}_n)\Psi(\mathbf{r}_1, \mathbf{r}_2, .., \mathbf{r}_n)\, d\mathbf{r}_2..d\mathbf{r}_n. \tag{2.6}$$

This has an obvious advantage over the wavefunction approach; for a N electron system, the wavefunction is a complex function of $3N$ variables ($4N$ if spin is included), while the charge density is a function of 3 (4) variables. The usefulness of DFT arises as the ground state properties of a system are determined by the ground state density, which for a given number of electrons is a unique function of the potential.

The earliest work in this spirit was that of Thomas and Fermi [28, 29]. Here the energy was given by the kinetic energy of a uniform electron gas and the classical electrostatic interaction between the electrons and nuclei for an electron gas of a given energy. This was then extended by adding the exchange energy of the electrons from the work of Dirac. This Thomas-Fermi (TF) theory gave poor results due to the large approximations made in kinetic energy [29]. It was the work of Kohn, Hohenberg, and Sham [26, 27] that provided a route to useful calculations, which will be discussed in the following sections. Whereas the TF approach involves the electron density only, the Kohn-Sham (KS) approach reintroduced wavefunctions. These can be found from solving one-electron equations involving an exact kinetic energy functional and a local effective potential.

2.3.1 Hohenberg-Kohn Theorem

Consider a potential $v(\mathbf{r})$ that gives an electron density $\rho(\mathbf{r})$. Now assume there is another potential $v'(\mathbf{r})$ that gives the same density. These potentials would give two

Hamiltonians $\hat{H}$ and $\hat{H}'$ that have the same ground state density but would have different wavefunctions Ψ and Ψ', with $\hat{H}\Psi = E_0\Psi$ and $\hat{H}'\Psi = E_0'\Psi'$. Then by the variational principle

$$\begin{aligned} E_0 &< \langle\Psi'|\hat{H}|\Psi'\rangle \\ &< \langle\Psi'|\hat{H}'|\Psi'\rangle + \langle\Psi'|\hat{H} - \hat{H}'|\Psi'\rangle \\ &< E_0' + \int \rho(\mathbf{r})[v(\mathbf{r}) - v'(\mathbf{r})]d\mathbf{r}. \end{aligned} \tag{2.7}$$

Similarly

$$\begin{aligned} E_0' &< \langle\Psi|\hat{H}'|\Psi\rangle \\ &< \langle\Psi|\hat{H}|\Psi\rangle + \langle\Psi|\hat{H}' - \hat{H}|\Psi\rangle \\ &< E_0 \quad \int \rho(\mathbf{r})[v(\mathbf{r}) - v'(\mathbf{r})]d\mathbf{r}. \end{aligned} \tag{2.8}$$

Adding (2.7) and (2.8) together gives the contradiction $E_0 + E_0' < E_0 + E_0'$ [26]. Thus, it can be deduced that no two different $v(\mathbf{r})$ can give rise to the same $\rho(\mathbf{r})$, i.e. the density is a unique functional of the potential. This shows that it is possible to rewrite the Schrödinger equation in terms of the density.

2.3.2 Kohn-Sham Equations

While the Hohenberg-Kohn theorem shows it is possible to use the ground state density to calculate properties of the system, it does not provide a way of finding the ground state density. A route to this is provided by the Kohn-Sham equations [27]. To derive these equations consider the ground state energy, given as a functional of the charge density

$$E\left[\rho(\mathbf{r})\right] = T\left[\rho(\mathbf{r})\right] + \int \rho(\mathbf{r})v(\mathbf{r})\, d\mathbf{r} + E_{ee}. \tag{2.9}$$

The first term in (2.9) is the kinetic energy, the second is the interaction with the external potential, including the electron-nuclei interaction, and the last is the

electron-electron interaction which can be written as

$$E_{ee}\left[\rho(\mathbf{r})\right] = \frac{1}{2}\int \frac{\rho(\mathbf{r})\rho(\mathbf{r}')}{|\mathbf{r}-\mathbf{r}'|}\, d\mathbf{r}d\mathbf{r}' + E_{xc}\left[\rho(\mathbf{r})\right]. \tag{2.10}$$

The first term on the right hand side of (2.10) is the electron-electron electrostatic interaction while the second is the non-classical exchange-correlation energy.

Kohn and Sham derived a set of single particle SEs by reintroducing wavefunctions ψ_i, with

$$\rho(\mathbf{r}) = \sum_{i=1}^{n} \psi_i^*(\mathbf{r})\psi_i(\mathbf{r}) \tag{2.11}$$

where n is the number of electrons. The kinetic energy is given by

$$T\left[\rho(\mathbf{r})\right] = -\frac{\hbar^2}{2m}\sum_{i}^{n}\langle\psi_i|\nabla^2|\psi_i\rangle \tag{2.12}$$

If the wavefunctions are required to be orthonormal, i.e.

$$\int \psi_i^*(\mathbf{r})\psi_j(\mathbf{r})d\mathbf{r} = \delta_{ij} \tag{2.13}$$

then we can define a functional of the wavefunctions

$$\Omega\left[\psi_i\right] = E\left[\rho(\mathbf{r})\right] - \sum_i\sum_j \epsilon_{ij}\int \psi_i^*(\mathbf{r})\psi_j(\mathbf{r})d\mathbf{r} \tag{2.14}$$

where ϵ_{ij} are Lagrange multipliers to ensure the wavefunctions are orthonormal. Minimization of $\Omega\left[\psi_i\right]$ with respect to $\psi_i^*(\mathbf{r})$ gives the Kohn-Sham equations

$$\left[-\frac{\hbar^2}{2m}\nabla^2 + v_{eff}(\mathbf{r})\right]\psi_i(\mathbf{r}) = \epsilon_i\psi_i(\mathbf{r}) \tag{2.15}$$

$$v_{eff}(\mathbf{r}) = v(\mathbf{r}) + \int \frac{\rho(\mathbf{r}')}{|\mathbf{r}-\mathbf{r}'|}d\mathbf{r}' + v_{xc}(\mathbf{r}), \tag{2.16}$$

where $v_{xc}(\mathbf{r})$ is the exchange-correlation potential given by

$$v_{xc}(\mathbf{r}) = \frac{\delta E_{xc}}{\delta\rho(\mathbf{r})}. \tag{2.17}$$

On going from (2.14) to (2.15) a unitary transform is performed to ensure the wavefunctions $\phi_i(\mathbf{r})$ are orthonormal [30]. As can be seen (2.15) is of the same form as the single particle Schrödinger equation with an effective local potential v_{eff} defined in (2.16). This is in contrast to the Hartree-Fock equations [22], in which there is a non-local potential in the one-electron equations.

2.3.3 Exchange-Correlation Potentials

The third term in the effective potential (2.16) is the *exchange-correlation potential.* This is of central importance in the accuracy of DFT calculations, and there has been much work in finding accurate forms of v_{xc} [31].

2.3.3.1 Local Density Approximation

The simplest approximation is to assume that the density can be treated locally as an uniform electron gas; the exchange correlation energy at each point in the system is the same as that of an uniform electron gas of the same density. This approximation was originally introduced by Kohn and Sham [27] and holds for a slowly varying density. Using this approximation the exchange-correlation energy for a density $\rho(\mathbf{r})$ is given by

$$E_{xc}^{LDA} = \int \rho(\mathbf{r})\epsilon_{xc}(\rho)d\mathbf{r}, \tag{2.18}$$

where $\epsilon_{xc}(\rho)$ is the exchange-correlation energy per particle of an uniform electron gas of density ρ. The exchange-correlation potential is then given by [30]

$$v_{xc}^{LDA}[\rho(\mathbf{r})] = \frac{\delta E_{xc}^{LDA}}{\delta\rho(\mathbf{r})} = \epsilon_{xc}(\rho) + \rho(\mathbf{r})\frac{\partial\epsilon_{xc}(\rho)}{\partial\rho}. \tag{2.19}$$

This can then be inserted into (2.16) for use in calculations.

For practical use of the LDA in calculations it is necessary to determine the exchange-correlation energy for an uniform electron gas of a given density. It is common to split $\epsilon_{xc}(\rho)$ into exchange and correlation potentials $\epsilon_{xc}(\rho) = \epsilon_x(\rho)+\epsilon_c(\rho)$. The exchange potential is given by the Dirac functional [32]

$$\epsilon_x[\rho(\mathbf{r})] = -\frac{3}{4}\left(\frac{3}{\pi}\right)^{\frac{1}{3}}\rho(\mathbf{r}). \tag{2.20}$$

Accurate values for $\epsilon_c(\rho)$ have been determined from Quantum Monte Carlo (QMC) calculations [33]. These have then been interpolated to provide an analytic form for $\epsilon_c(\rho)$ [34]

2.3.3.2 Generalized Gradient Approximations

As the LDA approximates the energy of the true density by the energy of a local constant density, it fails in situations where the density undergoes rapid changes such as in molecules. An improvement to this can be made by considering the gradient of the electron density, the so-called Generalized Gradient Approximation (GGA). Symbolically this can be written as

$$E_{xc} = E_{xc}[\rho(\mathbf{r}), \nabla\rho(\mathbf{r})]. \tag{2.21}$$

This can lead to a large improvement over LDA results with accuracy approaching that of correlated wavefunction methods such as MP2 and in some cases surpassing these [24].

While there is only one LDA there are several different parameterizations of the GGA. Some of these are semi-empirical, in that experimental data (e.g. atomization energies) is used in their derivation. Others are found entirely from first principles. A commonly used functional is the PW91 functional, due to Perdew and Yang [35,36].

2.4 Basis Sets

Both wavefunction and density functional methods aim to compute properties of interest without recourse to experimental data. Doing this requires finding the wavefunction. As this is generally unknown, it is usual to expand it in terms of a set of known functions. A single electron wavefunction can be written as

$$\psi_i(\mathbf{r}) = \sum_{j=1}^{\infty} c_j \phi_j(\mathbf{r}), \tag{2.22}$$

where $\phi_j(\mathbf{r})$ are members of a complete set of functions. Obviously it is impossible to use an infinite number of basis functions so the sum in (2.22) is taken over a finite number of functions. This introduces another source of error into the calculations as it is not then possible to describe components of Ψ along the missing functions.

Any family of functions could, in principle, be used as basis functions. Ideally the basis functions should have the same limiting behaviour as the real wavefunction, for an isolated atom or molecules they should decay to zero, and they should be computationally inexpensive.

2.4.1 Localized Basis Sets

For isolated atoms and molecules the wavefunction exponentially decays to zero at large distances. This implies that the basis functions used for these calculations should do likewise. Atomic orbitals are basis functions that have this property and come in two forms: Slater type orbitals (STO) and Gaussian type orbitals (GTO).

STOs have the following form (in spherical coordinates) [23]

$$\phi_{STO}^{nlm\zeta}(r,\theta,\phi) = \alpha Y_{lm}(\theta,\phi) r^{n-1} e^{-\zeta r} \tag{2.23}$$

where α is a normalization constant, $Y_{lm}(\theta,\phi)$ is a spherical harmonic. l, m, a n are quantum numbers, and ζ determines the radius of the orbit. The exponential dependence on distance is the same as for the hydrogen atom. GTOs have a similar form (again in spherical coordinates)

$$\phi_{GTO}^{nlm\zeta}(r,\theta\,\phi) = \alpha Y_{lm}(\theta,\phi) r^{(2n-2-l)} e^{-\zeta r^2}. \tag{2.24}$$

In both cases the angular dependence of the wavefunction is contained in the spherical harmonics,where the l, m values determine the type of the orbital (e.g. $l = 0$ is a s type orbital, $l = 1$ a p orbital, etc).

The chief difference between STO and GTO is the power of r in the exponent. The r^2 dependence in the exponent in the GTOs is a poorer representation than that of the STO. GTOs also have a zero slope at the nucleus ($r = 0$) whereas STOs have a cusp. GTOs also fall off more rapidly with distance than STOs. These factors suggest that more GTOs are needed to form a suitable basis set than STOs, roughly three times as many are needed to achieve the same accuracy [23].

However, GTOs are computationally more efficient than STOs: the factor r in the exponent requires taking a square root ($r = \sqrt{x^2 + y^2 + z^2}$) which is computationally very slow. This computational efficiency more than compensates for the additional number of functions needed, so GTOs are more commonly used in calculations.

The size of the basis set has a large bearing on the accuracy of the calculation. The smallest basis set possible is the minimum basis set which contains only enough functions to contain all the electrons in the neutral atoms. Increasing the number of basis functions improves the quality of the calculation. Additional higher angular momentum (d, f orbitals) basis functions may also be added to attempt to account for polarization effects.

2.4.2 Plane Wave Basis Sets

For periodic systems the potential has the property

$$V(\mathbf{r} + n\mathbf{a}) = V(\mathbf{r}) \tag{2.25}$$

where $\mathbf{a}$ is a lattice vector and n is an integer. Using Bloch's theorem [37] the wavefunction can be written as a product of a cell periodic part and a wavelike part

$$\psi_i(\mathbf{r}) = e^{i\mathbf{k}.\mathbf{r}} f_i(\mathbf{r}). \tag{2.26}$$

Due to its periodicity $f(\mathbf{r})$ can be expanded as a set of plane waves

$$f_i(\mathbf{r}) = \sum_{\mathbf{G}} c_{i,\mathbf{G}} e^{i\mathbf{G}.\mathbf{r}} \tag{2.27}$$

where $\mathbf{G}$ are reciprocal lattice vectors. Thus the electronic wave functions can be written as

$$\psi_i(\mathbf{r}) = \sum_{\mathbf{G}} c_{i,\mathbf{G}} e^{i(\mathbf{k}+\mathbf{G}).\mathbf{r}}. \tag{2.28}$$

As in the localized case an infinite number of basis functions would be needed to exactly recreate the real wavefunction. The number of wavefunctions used is controlled by the largest wave vector in the expansion in (2.27). This is equivalent

to imposing a cut-off on the kinetic energy as the kinetic energy of an electron with wavevector $\mathbf{k}$ is given by

$$E_k = \frac{\hbar^2|\mathbf{k}|^2}{2m}. \tag{2.29}$$

Plane wave basis sets can also be applied to non-periodic systems such as isolated molecules. To accomplish this the molecule is placed at the centre of a periodic supercell. If the supercell is large enough the interactions between the molecules in neighbouring cells becomes negligible. This is illustrated in Fig. 2.1.

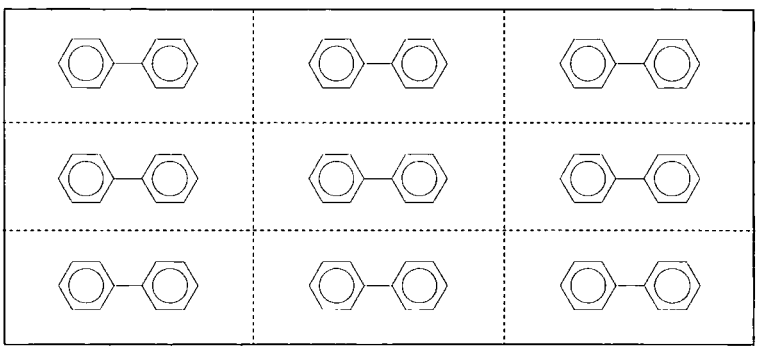

Figure 2.1: Supercell geometry for an isolated molecule. The dashed line encloses the periodic supercell.

As wavefunctions in isolated molecules bear little resemblance to plane waves many more plane waves are needed compared to a set of STOs or GTOs. However, the Kohn-Sham equations take on a very simple form using plane waves [38]

$$\left\{\sum_{\mathbf{G}'}\frac{\hbar^2}{2m}|\mathbf{k}+\mathbf{G}|^2\delta_{\mathbf{G}\mathbf{G}'} + V_{en}(\mathbf{G}-\mathbf{G}') + V_{ee}(\mathbf{G}-\mathbf{G}') + V_{XC}(\mathbf{G}-\mathbf{G}')\right\} c_{i,\mathbf{k}+\mathbf{G}'} = c_{i,\mathbf{k}+\mathbf{G}}\epsilon_i, \tag{2.30}$$

where $V_{en}(\mathbf{G}-\mathbf{G}')$, $V_{ee}(\mathbf{G}-\mathbf{G}')$, and $V_{XC}(\mathbf{G}-\mathbf{G}')$ are the Fourier transforms of the electron-nuclei, electron-electron Coulomb, and exchange-correlation potentials in (2.15) and (2.16).

Plane wave basis sets also have a few other advantages over Slater or Gaussian functions. These include

- the same basis set can be used for all atomic species,

- convergence toward completeness can easily be tested,
- plane waves do not depend on nuclear positions so, unlike localized basis sets, correction terms are not needed for the calculation of forces (see §2.6.2).

Due to these advantages, *ab initio* work presented here use a plane wave basis set.

2.5 Pseudopotentials

When using a plane wave basis set, the region close to an atomic nucleus requires special attention. This is due to two main factors. The first is that the electron-nucleus potential varies as $\frac{1}{r}$ so it diverges as $r \to 0$. Secondly, to ensure the valence electron wavefunctions are orthogonal to the core electron wavefunctions (as required by the exclusion principle) the valence wavefunctions must oscillate rapidly within the core region. These factors lead to large kinetic energies hence the need for large numbers of plane waves. Also a large number of plane waves are needed to describe the tightly bound core states.

These problems can be circumvented by the use of the *pseudopotential* approximation. This is motivated by the observation that most physical properties are determined by the valence electrons. The pseudopotential approximation exploits this by removing the core electrons and combining the interaction between the core and valence electrons and the strong nuclear valence electron interaction into a weaker pseudopotential [39]. Within the core region the valence wavefunctions are then replaced by smoother nodeless pseudo-wavefunctions that are identical to the real wavefunctions outside the core region. This reduces the complexity of the problem in a number of ways. Firstly, removing the core electrons means fewer wavefunctions need to be calculated. Secondly, as the potential no longer diverges toward $-\infty$ and the valence wave functions are smoother within the core region, fewer plane waves are needed to adequately describe the valence wavefunctions. To ensure that a pseudopotential calculation reproduces the same energy differences as

an all-electron calculation it is necessary for the pseudo-wavefunctions to be identical to the all-electron wavefunctions outside the core. This condition is called 'norm-conservation'.

There are a number of different schemes for generating a pseudopotential, two of the most commonly used including the Kleinman-Bylander [40] and Vanderbilt or ultrasoft pseudopotentials [41]. Typically, generation of a pseudopotential proceeds as follows. Firstly a cut-off distance for the core and an exchange-correlation potential is chosen. A form for the pseudopotential is also chosen; the most general form is

$$V_{pp} = \sum_{lm} Y_{lm}(\theta, \phi) V_l(r) Y^*_{lm}(\theta, \phi), \tag{2.31}$$

where $Y_{lm}(\theta, \phi)$ are spherical harmonics and $V_l(r)$ is the pseudopotential for the lth angular momentum component. Then an all-electron calculation is performed. An initial set of parameters for the pseudopotential is chosen and the eigenvalues and wavefunctions calculated. The eigenvalues and wavefunctions from the pseudopotential calculation are compared to those found from the all-electron calculation. If these are equal then a self-consistent pseudopotential has been generated. Otherwise a new set of parameters is chosen and the above process is repeated.

The use of plane wave basis sets with pseudopotentials is often referred to the *Pseudopotential-Plane Wave* method [42]. While it originally arose for the study of crystalline systems, it has also been applied to non-periodic systems such as molecules [43] and polymers [44]. The pseudopotential-plane wave method is also commonly used in *ab initio* molecular dynamics simulation schemes such as the Car-Parrinello method [45].

2.6 Practical Electronic Structure Calculations

This section outlines the details of how the calculations are performed using the plane wave pseudopotential method.

2.6.1 Single Point Energy Calculations

A single point energy (SPE) calculation calculates the wavefunction and charge density, and hence the energy, of a particular (arbitrary) arrangement of nuclei. The total energy functional of a system of electrons and nuclei can be written as

$$E[\rho(\mathbf{r_i}), \mathbf{R}_I] = T_e[\rho(\mathbf{r_i})] + T_n + E_{en}[\rho(\mathbf{r_i}), \mathbf{R}_I] + E_{ee}[\rho(\mathbf{r_i})] + E_{nn}(\mathbf{R}_I) \qquad (2.32)$$

where $T_e[\rho(\mathbf{r_i})]$ is the electronic kinetic energy given in (2.12), T_n is the nuclear kinetic energy, E_{en} is the electron-nuclei interaction given in (2.9), E_{ee} is the electron-electron interaction and E_{nn} is the nuclei-nuclei interaction. E_{ne} is described using pseudopotentials §2.5 while for a fixed set of nuclear positions T_n is zero and E_{nn} is a constant. Thus a SPE calculation is reduced to finding the charge density that minimizes the total energy functional, i.e. solving the Kohn-Sham equations.

The minimization of the total energy functional can be done in a number of ways. One method proceeds by direct diagonalization of the matrix equation (2.30). Starting from an initial trial density E_{ee} is calculated and inserted into (2.30). A new density is then calculated by inverting the matrix equation (2.30). If this new density gives an energy that is consistent with the old density (if the change in energy between iterations is smaller than a given tolerance) it is then inserted into the total energy functional and the energy calculated. Otherwise this new density is used to calculate a new E_{ee}. This is repeated until the density and potential are consistent with each other, within a given tolerance.

The matrix diagonalization method has the disadvantage that the computational cost of matrix diagonalization scales as the number of plane waves cubed. An alternative method is to minimize the energy functional directly [46]. The energy functional is a functional of the density, which is determined by the expansion coefficients $c_{i,\mathbf{k}+\mathbf{G}}$. The ground state density is found from the set of $c_{i,\mathbf{k}+\mathbf{G}}$ that minimize the energy functional. Standard functional optimization methods [47] can then be used to find the minima of the total energy functional. The simplest of these

techniques is the method of *Steepest Descents* (SD) [47]. The SD method produces a series of points $\{\mathbf{P}_i\}$

$$\mathbf{P}_{i+1} = \mathbf{P}_i + \lambda_i \mathbf{h}_i \tag{2.33}$$

where

$$\mathbf{h}_i = -\nabla f(\mathbf{P}_i). \tag{2.34}$$

In this case $\mathbf{P}_i$ are sets of plane wave expansion coefficients and $f(\mathbf{P})$ is the energy functional. The scalar λ_i in (2.33) is the distance along the direction $\mathbf{h}_i$ from $\mathbf{P}_i$ that a minima is located. The SD method proceeds by moving in the steepest downhill direction from a point $\mathbf{P}_i$ until a minima along that direction is located at point $\mathbf{P}_{i+1}$. The steepest downhill direction from $\mathbf{P}_{i+1}$ is then determined ($-\nabla f(\mathbf{P}_{i+1})$) and the minima located along that direction is found. This is repeated until the change in the function is lower than a preset tolerance. The speed at which the SD method will find a minima is limited as at each step only the information at that point is taken into account. It is easy to think of examples where this will lead to slow convergence. A better method is the *Conjugate Gradients* (CG) method [46–48]. It differs from the SD method in that each search direction is conjugate to the last one. The CG method assumes that the function can be approximated by a quadratic form

$$f(\mathbf{x}) \approx \frac{1}{2}\mathbf{x}.\mathbf{A}.\mathbf{x} \tag{2.35}$$

where $\mathbf{A}$ is the Hessian given by

$$A_{ij} = \left.\frac{\partial^2 f}{\partial x_i \partial x_j}\right|_{\mathbf{x}=\mathbf{x}_0}. \tag{2.36}$$

The CG method produces a series of points as in (2.33) but $\mathbf{h}_i$ is given by

$$\mathbf{h}_i = \begin{cases} \mathbf{g}_i, \ i = 0 \\ \mathbf{g}_i + \frac{\mathbf{g}_i.\mathbf{g}_i}{\mathbf{g}_{i-1}.\mathbf{g}_{i-1}}\mathbf{h}_{i-1}, \ i > 0 \end{cases} \tag{2.37}$$

where $\mathbf{g}_i = -\nabla f(\mathbf{P}_i)$. Using the quadratic form (2.35) the step needed to get to the minima in the direction $\mathbf{h}_i$ is given by [47]

$$\lambda_i = \frac{\mathbf{h}_i.\mathbf{g}_i}{\mathbf{h}_i.\mathbf{A}.\mathbf{h}_i}. \tag{2.38}$$

This however can be found from a one-dimensional minimization along $\mathbf{h}_i$, i.e. without explicitly calculating the Hessian. As the Hessian is an $N \times N$ matrix, for DFT calculations with $N = 10^5 - 10^6$ plane waves the CG method has a large advantage over methods that explicitly use the Hessian. The CG method will find a minimum of an N dimensional function in N iterations. When using the CG and SD methods to minimize the total energy functional , the requirement that the wavefunctions are to be orthonormal places an additional constraint on the minimzation. For a DFT calculation with 10^5 plane waves this is still a monumental task. The number of iterations required can be substantially reduced by preconditioning the function [46].

2.6.2 Geometry Optimization

While a single point energy calculation gives information on a single molecular structure, the aim of geometry optimization is to generate the optimal (lowest energy) structure of a molecule from an arbitrary starting state. As the motion of the nuclei and the electrons can be separated using the Born-Oppenheimer approximation a geometry optimization typically proceeds as a set of single point energy calculations. For the initial starting geometry a SPE calculation is performed. The forces on the nuclei can be calculated from the wavefunction using the Hellmann-Feynman theorem [49]. The force on a nucleus I with position $\mathbf{R}_I$ is

$$\mathbf{F}_I = -\left\langle \frac{\partial E}{\partial \mathbf{R}_I} \right\rangle \tag{2.39}$$

where E is the energy. This force can then be used to find the ground state positions of the atoms. The forces can be used to calculate a *molecular dynamics* trajectory (see §3.4.3). As the forces point toward a (at least local) minimum in the energy integrating the equations of motion for the nuclei will move the nuclei toward an equilibrium structure. Alternatively, functional optimization techniques such as those described in §2.6.1 may be used. Due to the smaller size of the problem, Hessian based methods [47] may also be used for this.

Two points should be made about the above method. Firstly, an error is introduced into the Hellman-Feynman forces if the basis set is incomplete, called the Pulay force [50]. However, for a plane wave basis set the wavefunctions do not depend on the nuclear positions, hence this error is zero, as long as the electronic system has converged to the ground state. For situations where the cell shape changes analogous Pulay stresses arise [51]. Secondly, the above procedure will find the nearest (in configuration space) point at which the forces are zero. Thus if a poor starting point is chosen it may find a local rather than a global minimum in the potential energy surface or if the starting point is an energy maximum it may remain there. This procedure can also be rather time consuming with many SPE calculations needed to find the minima. Thus it is common to perform an initial energy minimization using molecular mechanics calculations (§3.4.1) to get to the vicinity of a minima and then perform a full *ab initio* geometry optimization.

2.7 Use of *Ab Initio* Calculations in This Thesis

The *ab initio* methods described in this chapter have been used in chapter 4 to calculate the structures and conformational energies of a series of small organic molecules. Electron-ion interaction are evaluated using ultra-soft (Vanderbilt) pseudopotentials and the exchange-correlation energy was calculated using the PW91 functional. The calculations were performed using the CASTEP program [38, 52]. Conformational energies were calculated using the conjugate gradients method outlined in §2.6.1, while equilibrium structures were calculated using the method described in §2.6.2.

Chapter 3

Computer Simulation Methods

3.1 Introduction to Computer Simulations of Liquids

The first computer simulation of liquid was performed almost half a century ago by Metropolis, Rosenbluth, Rosenbluth, Teller, and Teller [53]. While crude by modern standards, this first simulation saw the use of the *Metropolis Monte Carlo* method that is still in use today. This method, outlined in §3.4.2 aims to sample the configuration space and calculate the properties of a system by randomly sampling from the possible states of the system. Monte Carlo methods are widely used in many different areas of science outside of molecular simulations.

Within a few years, the first Monte Carlo simulations were followed by the first *molecular dynamics* simulations [54–56]. In these studies the equations of motion are solved numerically. Tracing the study of the time evolution of a system allows the study of time dependent phenomena such as diffusion. The molecular dynamics method is discussed in §3.4.3.

These early simulations used hard sphere potentials. A further step was the use of the Monte Carlo and molecular dynamics methods with more realistic potentials.

The hard-sphere potential was replaced by spatially varying potentials [57–60] with both attractive and repulsive terms. Simulations of molecules were also performed, with either anisotropic single site potentials or a collection of atoms bonded together.

While early simulations were restricted to small numbers of particles and simple interaction models, they were able to convincingly simulate simple liquids and provided valuable insights into the liquid state, such as the long time behaviour of transport properties [61]. With increasing computer power and improvements to simulation techniques both the size and complexity of the systems studied has grown. It is possible to study up to 1000s of molecules with atomistic detail or up to a million simpler molecules on large supercomputers and even single processor workstations able to handle up to 10^4 particles (atoms or molecules). This increase in power has also allowed the variety of systems studied to grow. Computer simulation techniques are now well established in many areas of science.

3.2 Computer Simulations of Liquid Crystal Phases

Liquid crystals have many interesting and useful properties and so have attracted great attention from both experimentalists and theorists. Studies of liquid crystals have also contributed to the study of phase transitions and critical phenomena and analogues can be found between liquid crystal systems and systems found elsewhere in science [62].

Computer simulations have played a valuable role in bridging the gap between theory and experiment. Theoretical studies tend to be based around simple models; aiming to reduce the complexity of the problem but retaining the essential physics. Thus, it is often difficult to compare theoretical predictions with experimental results. However, computer simulations can provide essentially exact results for these simple models, and hence can be used as a test of theory.

Computer simulation also provides a route from the microscopic detail (atomic masses, atomic charges, etc) to the macroscopic details (equations of state, materials properties, etc). They also allow the straight forward elucidation of detail at the microscopic scale, which can be hard (if not impossible) to probe from experiment. For instance the structure of a fluid is easily found from simulation but somewhat more difficult from experiment. Additionally, it also provides a route to determine properties in situations out of the reach of experiment, such as high pressures or temperatures. However, in all these cases, predictions of properties are dependent on a good model of the interactions between particles.

Simulation of liquid crystalline systems can present some particular challenges. One is the reduced symmetry of liquid crystalline phases compared to simple liquids. This complicates the description of the structures and dynamics of liquid crystal phases. The reduced symmetry of the molecules implies the simulation model used should reflect this shape anisotropy. As well as being highly anisotropic, molecules that form liquid crystal phases often contain groups that are hard to model, such as polar or polarizable groups, or a combination of rigid and flexible groups. Many interesting phenomena in liquid crystals occur over long periods of time; for example the formation of a nematic phases from an isotropic liquid occurs over tens of nanoseconds. Molecular reorientation in nematic phases can be an order of magnitude slower. These timescales are on the edge of what can be achieved using current computer power. In a similar manner many interesting phenomena occur over large length scales, and involve many ten or hundreds of thousands of molecules. These problems however, have not prevented many successful simulations of liquid crystal phases, which have greatly contributed to our present understanding of liquid crystals.

3.3 Model Potentials for Liquid Crystal Phases

The potentials used in simulations of liquid crystals have varied widely, from simple models commonly used to test basic theories of liquid crystal structure and dynamics to more complicated atomistic models used to simulate *real* liquid crystal systems. The earliest simulations of liquid crystals used a lattice model, the Lebwohl-Lasher model [63]. This represented molecules (or groups of molecules) as vectors on a lattice. While this highly idealized model allows the simulation of large system sizes, it neglects important features such as translational freedom and molecular structure.

3.3.1 Hard Models

The simplest model of a liquid is the hard sphere model where the molecules are taken to be spheres of radius r_0 that interact through a hard wall potential

$$V(r) = \begin{cases} \infty, & r \leq r_0 \\ 0\ , & r > r_0 \end{cases} . \tag{3.1}$$

This can be generalized to liquid crystals by replacing the spheres with an appropriate non-spherical shape, such as ellipsoids and spherocylinders for calamitic molecules and oblate ellipsoids and cut spheres for discotics [64, 65] examples of which are shown in Fig. 3.1. The hard wall or *excluded volume* interaction arises from the strong repulsion between molecules as their electron clouds begin to overlap. This short range interaction is sufficient to give rise to ordered phases. However, due to the lack of attractive interactions the phase behaviour is controlled by the density and molecular shape not by temperature. Thus these systems do not form thermotropic phases in the strictest sense although the phases formed are typical of a thermotropic system.

Hard body potentials are extremely simple models and have greatly increased the understanding of the effect molecular shape has on liquid crystal phases. Simulations

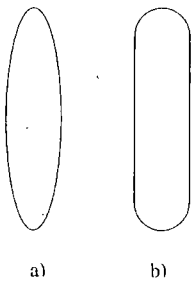

Figure 3.1: Hard (a) ellipsoid, and (b) spherocylinder.

of hard spheres have shown two phases; solid and fluid. When the length to breadth ratio is increased (for rod shaped particles) or decreased (for disk shaped particles) a nematic phase arises [66, 67]. This occurs at a length to breadth ratio of 3:1 or 1:3 for hard ellipsoids. For hard spherocylinders with length to breadth ratios of at least 4 to 1 nematic and smectic phases are observed [68].

3.3.2 Soft Models

To understand the effect of attractive forces, such as dispersion or electrostatic interactions, it is necessary to replace the hard wall potential with one that allows the molecules to inter-penetrate (allows $r \leq r_0$). These are often termed *soft models.* For liquids a simple model is the Lennard-Jones potential [69]

$$V_{LJ}(r) = 4\epsilon_{ij}\left[\left(\frac{\sigma_{ij}}{r}\right)^{12} - \left(\frac{\sigma_{ij}}{r}\right)^{6}\right] \tag{3.2}$$

where ϵ_{ij} is the well depth and σ_{ij} is the distance at which $V_{LJ} = 0$. Both ϵ_{ij} and σ_{ij} are constants that depend on the molecules taking part. A plot of a typical Lennard-Jones potential is shown in Fig. 3.2.

This can be generalized to liquid crystals if ϵ_{ij} and σ_{ij} are made functions of the orientations of the molecules [70]. The most common soft model for simulating liquid crystals is the Gay-Berne (GB) potential [71]. This has the form

$$V_{GB}(\mathbf{r}_{ij}, \mathbf{u}_i, \mathbf{u}_j) = 4\epsilon^{GB}(\mathbf{r}_{ij}, \mathbf{u}_i, \mathbf{u}_j)\left[\left(\frac{\sigma^{GB}}{r - \sigma(\mathbf{r}_{ij}, \mathbf{u}_i, \mathbf{u}_j) + \sigma^{GB}}\right)^{12} -\right.$$

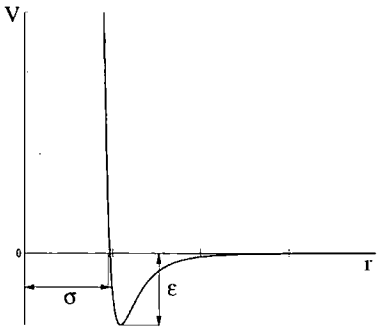

Figure 3.2: The Lennard-Jones potential.

$$\left(\frac{\sigma^{GB}}{r-\sigma(\mathbf{r}_{ij},\mathbf{u}_i,\mathbf{u}_j)+\sigma^{GB}}\right)^6\Bigg] \tag{3.3}$$

where $\mathbf{r}_{ij}$ is the intermolecular vector and $\mathbf{u}_i$ and $\mathbf{u}_j$ are the orientation vectors. A schematic diagram of the orientation vectors is shown in Fig. 3.3. The orientational dependent well depth $\epsilon(\mathbf{r}_{ij},\mathbf{u}_i,\mathbf{u}_j)$ is given by

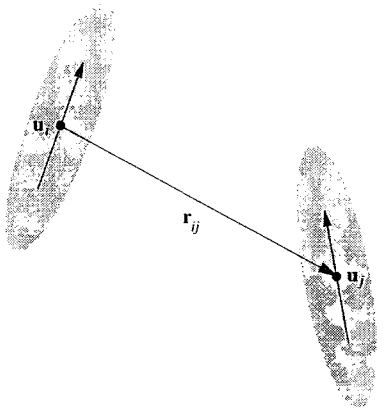

Figure 3.3: Schematic diagram showing definitions of $\mathbf{u}_i$, $\mathbf{u}_j$, and $\mathbf{r}_{ij}$ for a pair of Gay-Berne molecules.

$$\epsilon^{GB}(\mathbf{r}_{ij},\mathbf{u}_i,\mathbf{u}_j)=\epsilon_0\epsilon^{GB}\left(\mathbf{u}_i.\mathbf{u}_j\right)^{\nu}\epsilon'^{GB}\left(\mathbf{U}_i,\mathbf{u}_j,\mathbf{r}_{ij}\right)^{\mu} \tag{3.4}$$

where

$$\epsilon^{GB}\left(\mathbf{u}_i.\mathbf{u}_j\right)=\left[1-\chi^2\left(\mathbf{u}_i.\mathbf{u}_j\right)^2\right]^{\frac{1}{2}} \tag{3.5}$$

and

$$\epsilon'^{GB}\left(\mathbf{u}_i, \mathbf{u}_j, \mathbf{r}_{ij}\right) = \left[1 - \frac{\chi'}{2}\left(\frac{\left(\mathbf{r}_{ij}.\mathbf{u}_i\right)^2 + \left(\mathbf{r}_{ij}.\mathbf{u}_j\right)^2 - 2\chi'\left(\mathbf{r}_{ij}.\mathbf{u}_i\right)\left(\mathbf{r}_{ij}.\mathbf{u}_j\right)\left(\mathbf{u}_i.\mathbf{u}_j\right)}{1 - \chi^2\left(\mathbf{u}_i.\mathbf{u}_j\right)^2}\right)\right]. \tag{3.6}$$

The orientationally dependent width is given by

$$\sigma(\mathbf{r}_{ij}, \mathbf{u}_i, \mathbf{u}_j) = \sigma_0\left[1 - \chi\left(\frac{\left(\left(\mathbf{r}_{ij}.\mathbf{u}_i\right)^2 + \left(\mathbf{r}_{ij}.\mathbf{u}_j\right)^2 - 2\chi(\mathbf{r}_{ij}.\mathbf{u}_i)(\mathbf{r}_{ij}.\mathbf{u}_j)\left(\mathbf{u}_i.\mathbf{u}_j\right)\right)}{1 - \chi^2\left(\mathbf{u}_i.\mathbf{u}_j\right)^2}\right)\right]. \tag{3.7}$$

In the above, χ depends on the well width anisotropy

$$\chi = \left[\frac{\kappa - 1}{\kappa + 1}\right], \tag{3.8}$$

where κ is the ratio σ_{ee}/σ_{ss}. σ_{ee} is the end-to-end contact distance and σ_{ss} is the side-by-side contact distance. χ' is the well depth anisotropy, given by

$$\chi' = \left[\frac{\kappa' - 1}{\kappa' + 1}\right] \tag{3.9}$$

where $\kappa' = \epsilon_{ss}/\epsilon_{ee}$. ϵ_{ee} is the end to end well depth and ϵ_{ss} is the side to side well depth. The Gay-Berne potential plotted for some different fixed molecular orientations are shown in Fig. 3.4.

The exact form of the Gay-Berne potential is determined by the four parameters μ, ν, κ, and κ' [72]. The original formulation, which was designed to mimic a line of four Lennard-Jones sites with a length to breadth ratio (κ) of 3, had the parameters κ=3, κ'=5, ν=1, and μ=2. Varying these parameters gives rise to an infinite number of Gay-Berne potentials. These have been shown to give rise to stable nematic and smectic phases. Discotic phases can also be studied by setting κ and κ' to be less than unity. The effects of adding electrostatic and chiral interactions to the Gay-Berne potential have also been studied [72, 73].

When hard and soft potentials are simple shapes, such as ellipsoids or spherocylinders, they can be joined so as to create more complicated geometries, examples of which are shown in Fig. 3.5. For instance bent-core (banana shaped) molecules

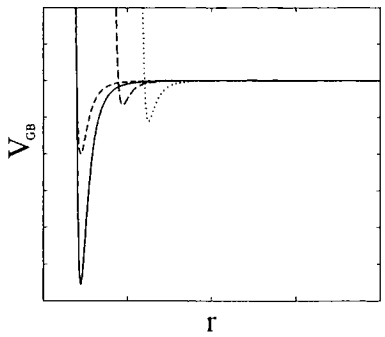

Figure 3.4: The Gay-Berne potential, with $\kappa = 3$, $\kappa' = 5$, $\mu = 1$, and $\nu = 2$, for molecules in the end to end, side to side, cross, and T configurations. The side-by-side configuration is shown by the solid line, the cross configuration is shown by the dashed line, the T configuration is shown by the long dashed line, and the end-to-end configuration is shown by the dotted line.

can be formed by joining two spherocylinders or Gay-Berne units at an angle [74,75] (Fig. 3.5a). Likewise a Gay-Berne unit and a Lennard-Jones atom can be joined to create a wedge shaped molecule [76–78] (Fig. 3.5b). Arbitrarily shaped molecules can be formed from a Gay-Berne like potential by expanding ϵ and σ as a set of angular dependent functions. This approach has been used to simulate a tear-drop shaped liquid crystal [79].

3.3.3 Atomistic Models

Atomistic models are the most detailed models used in simulation of all but the smallest molecules. Here molecules are represented as a number of atomic sites connected by chemical bonds. The interaction between these atoms is described by a potential, commonly known as a *force field*, which includes terms to describe bond stretches, bond angle bends, torsional rotations and non-bonded interactions. Additional terms to describe coupling between different distortions (e.g. coupling between a torsional rotation and a bond stretch) or other interactions such as hydrogen bonding may also be present.

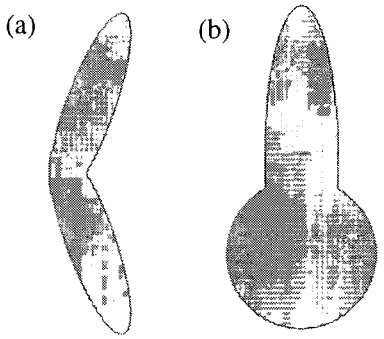

Figure 3.5: Examples of molecules formed by fusing Gay-Berne and Lennard-Jones particles: (a) shows a banana shaped molecule formed from two Gay-Berne molecules, (b) shows a wedge formed from a Gay-Berne and a Lennard-Jones particle.

The exact form of each term can vary from force field to force field. Bond stretches are usually described by a Taylor expansion of the energy about the equilibrium bond length l_0

$$V(l) = V(l_0) + \frac{1}{2}\left(\frac{\partial^2 V}{\partial l^2}\right)_{l=l_0}(l-l_0)^2 + \frac{1}{6}\left(\frac{\partial^3 V}{\partial l^3}\right)_{l=l_0}(l-l_0)^3 + \ldots, \tag{3.10}$$

where l is the bond length. The linear term in the above expansion is missing as the force $(-\frac{\partial V}{\partial l})$ is zero at equilibrium. As bond stretches are of a large energy, this is often truncated at the quadratic term

$$\Delta V(l) = \frac{1}{2}k_l(l-l_0)^2, \tag{3.11}$$

where $\Delta V(l) = V(l) - V(l_0)$ and $k_l = \left(\frac{\partial^2 V}{\partial l^2}\right)_{l=l_0}$. Similar terms are used for bond angle bending. Torsional rotations are modelled by a Fourier series

$$V(\tau) = \frac{1}{2}(V_1(1+\cos\tau) + \frac{1}{2}V_2(1-\cos 2\tau) + \frac{1}{2}V_3(1+\cos 3\tau), \tag{3.12}$$

where V_i are the torsional force constants.

The non-bonded interactions are usually divided into Van der Waals and electrostatic interactions. The electrostatic interaction is modelled by point charges on

the atoms interacting through Coulomb's law

$$V = \frac{1}{4\pi\epsilon_0}\frac{q_i q_j}{r_{ij}}, \tag{3.13}$$

although it is sometimes modelled as the interaction of point multipoles on atoms. There is a large range of different functional forms for the Van der Waals interaction. The simplest is the Lennard-Jones potential (3.2) although in some cases the exponent on the repulsive (r^{-12}) term varies. Another commonly used form is the Hill or Buckingham potential

$$V(r_{ij}) = A_{ij}\exp(-B_{ij}r_{ij}) - \frac{C_{ij}}{r_{ij}^6}. \tag{3.14}$$

Atomistic models allow the incorporation of molecular flexibility into a simulation. This flexibility can have a large effect on the properties of molecules such as liquid crystals and polymers. For example the flexible tails of low molecular mass liquid crystal molecules inhibit the formation of crystal lattices allowing the formation of liquid crystal phases in the first place. They also allow the direct comparison between simulation and experiment.

Atomistic models however, are much more computationally expensive than single site models. A typical low molecular mass mesogen has between 40-100 atoms, so the computational cost of representing a liquid crystalline molecule in this way is thousands of times higher than using a single site model (the computational cost of simulation scales, roughly, with the number of interaction sites squared). The computational effort involved in atomistic simulations can be reduced by eliminating unimportant atoms, usually hydrogen, by absorbing them into the other atoms.

While there have been many atomistic simulations of liquid crystals [80–107] the large computational cost restricts these to small system sizes (between 100-200 molecules) and short timescales (about 1 ns). Of these only one [99] has shown the formation of a nematic phase from an isotropic liquid; this took about 12 ns. However, with increasing computer power atomistic simulations of up to 1000 liquid crystal molecules are now possible [106, 107].

Most atomistic simulations to date have been performed on bulk nematic phases. However, there have been a few simulations of smectic systems [89,100,101,103,104]. Due to the larger size of these smectogenic molecules, simulations are typically of about 100 molecules, with as few as 12 [101] begin employed in one study. There have also been simulations of chiral nematic [85] and lyotropic liquid crystals [80]. Simulations have also been employed to study nematic droplets [107], free standing liquid crystalline films [89] and liquid crystals near surfaces [86, 90].

3.3.4 Hybrid Models

A compromise between single site models §3.3.2 and atomistic §3.3.3 models is provided by so called hybrid models. Here a molecule is represented by a number of rigid units joined together. This allows the modelling of flexibility of atomistic models with a lower computational cost. The rigid units can interact through either hard [108] or soft [109–112] potentials. Models of this kind have been used to study various liquid crystalline systems such as liquid crystal dimers [110], both main chain [111] and side chain liquid crystal polymers, and liquid crystal dendrimers.

The interaction potential for the Gay-Berne-Lennard-Jones (GB-LJ) hybrid model is similar to that of an atomistic model

$$\begin{aligned} E &= \sum_{bond} E_{bond} + \sum_{angle} E_{angle} + \sum_{tors} E_{tors} + \\ &\quad \sum_{non-bonded} E_{elec} + \sum_{LJ} E_{LJ-LJ} + \\ &\quad \sum_{GB} E_{GB-GB} + \sum_{GB-LJ} E_{GB-LJ}. \end{aligned} \tag{3.15}$$

The bond stretching, bond angle bending, torsional rotation, electrostatic, and Lennard-Jones terms take the same form as in §3.3.3, while the Gay-Berne term is the same as that in §3.3.2. The Gay-Berne-Lennard-Jones term is taken from the work of Cleaver *et al* [113].

Early examples of this model used hard spheres joined together to simulate liquid crystal systems. Later Gay-Berne units were used to model the rigid mesogenic core

of molecules while chains of Lennard-Jones particles modelled alkyl chains [110,112]. One interesting simulation involved replacing the phenyl rings of cyanobiphenyl liquid crystals by spheres [88,91].

3.4 Simulation Methods

3.4.1 Molecular Mechanics

This is the simplest and most common technique used in computer modelling of molecules. It focuses on finding low energy states of molecules. A typical molecular mechanics (MM) calculation [114] involves the following steps:

- Build a trial structure.
- Minimize the energy of molecule by varying internal degrees of freedom.
- Adjust internal coordinates (e.g. torsional angles), and reminimize the energy to find other low energy states.

This gives a set of molecular conformations that correspond to potential energy minima. One of these should be the global energy minima. Molecular properties can then be found by averaging over the different states, e.g. for a property A the average is given by

$$\langle A \rangle = \frac{\sum_i A_i \exp\left(-\frac{E_i}{k_B T}\right)}{\sum_i \exp\left(-\frac{E_i}{k_B T}\right)}, \tag{3.16}$$

where E_i is the energy of the i th conformation relative to the ground state. The value of A_i can be calculated either from the force field used in the molecular mechanics calculation or the molecular mechanics conformation can be used in an *ab initio* or semi-empirical calculation. The latter approach allows for the calculation of properties not available from classical calculations such as polarizabilities.

While MM is simple to implement, for large molecules, such as liquid crystalline molecules, there can be a large number of possible conformations and so finding

the global energy minima can be difficult. In such cases it is also difficult to know whether all conformations have been found. This problem can be over come by using more sophisticated methods of sampling the conformations of the molecule. Two well established methods for this, Monte Carlo (MC) and molecular dynamics (MD) simulations are outlined in the following sections.

3.4.2 Monte Carlo

Monte Carlo simulations aim to explore the conformation space of a system in order to determine the equilibrium average of some property A. This could, in principle, be achieved by evaluating the integral

$$\langle A \rangle = \int A(\mathbf{r}) P(\mathbf{r}) \, d\mathbf{r}, \tag{3.17}$$

where the probability distribution function $P(\mathbf{r})$ is given by

$$P(\mathbf{r}) = \frac{\exp\left(-\frac{E(\mathbf{r})}{k_B T}\right)}{\int \exp\left(-\frac{E(\mathbf{r})}{k_B T}\right) \, d\mathbf{r}}, \tag{3.18}$$

where $E(\mathbf{r})$ is the energy of the system with coordinates $\mathbf{r}$. The denominator in (3.18) is the partition function of the system.

While (3.17) and (3.18) can not be evaluated analytically, they could in principle be calculated using a numerical integration procedure. However, for all but the very smallest system this would involve an unfeasible number of calculations. Alternatively the integrals could be evaluated by sampling different configurations of the system to provide a representative sample of all the states. In its crudest form this would consist of making random changes to the coordinates of the system. From the energies calculated at each move, $A(\mathbf{r})P(\mathbf{r})$ can then be estimated and $\langle A \rangle$ can be found. This approach is flawed as each different configuration would contribute equally to the integral. Since $P(\mathbf{r})$ is proportional to the Boltzmann factor, only low energy configurations make a significant contribution to the integrals. However, a large number of configurations have a small Boltzmann factor due to high energy

overlaps between molecules. Thus only a small proportion of configuration space corresponds to low energy configurations where there are no overlaps and which correspond to physically observed states. Therefore many of the generated configurations would have little or no influence and so proper sampling would not have been achieved.

The sampling problem above can be solved by employing importance sampling, which is the essence of the *Metropolis Monte Carlo* method. This method is so wide spread that it is usually referred to simply as the *Monte Carlo* (MC) method. The crucial feature is that it biases the generation of configurations to those that make a significant contribution to (3.18). Specifically it generates a series of states with a Boltzmann distribution and counts them equally. This differs from the crude method outlined above which generates states with equal probability and then assigns them a Boltzmann weight.

The simulation must have a procedure for generating new configurations so that at the end of the simulation the appropriate probability distribution has occurred. This is achieved by setting up what is known as a Markov chain [115], which satisfies the following conditions

- The outcome of each trial belongs to a finite set of possible outcomes
- Each trial depends only on the outcome of the trial that precedes it.

These conditions are required to produce the correct limiting distribution, i.e. to produce the correct ensemble averages.

3.4.2.1 Metropolis Monte Carlo

For an atomic fluid, the Metropolis Monte Carlo method is quite simple to implement. At each MC step a new configuration is generated. This consists of making a random change to the coordinates of a randomly chosen atom. The size of the move is controlled by a parameter δr_{max}, so that $-\delta r_{max} < \delta r < +\delta r_{max}$. After the

move the energy of the new configuration, E_n is calculated and compared to the old energy, E_m. If $E_n < E_m$ the move is then accepted and the new energies, etc, are included in the statistics. If $E_n > E_m$ the move is accepted with a probability given by

$$\wp = \exp\left(-\frac{\delta e_{mn}}{k_B T}\right), \tag{3.19}$$

where $\delta E_{mn} = e_n - E_m$. In practice this means a random number, ζ, is generated and compared with $\wp$. If $\wp > \zeta$ then the move is accepted and the new energies, etc, are included in the statistics. If $\wp < \zeta$ the move is rejected and the old energies, etc, are retained and added into the statistics. For a hard body potential $\wp = 1$ where there are no overlaps, and $\wp = 0$ when two or more molecules overlap.

The maximum size of the move δr_{max} is usually chosen to give an acceptance ratio (number of accepted moves divided by the total number of moves) of around 50%. This can be adjusted during the equilibration period of the simulation to yield a desired acceptance ratio (changing δr_{max} during the actual production run destroys the Markov chain).

While the above is appropriate for constant temperature and volume (NVT) the Monte Carlo method is easily extended to other ensembles. For isothermal-isobaric Monte Carlo the volume is allowed to fluctuate. Thus there are now two different trial moves: a particle translation and a volume change. Once a new state has been produced, the quantity δH_{nm} is calculated

$$\delta H_{nm} = \delta E_{nm} + P(V_n - V_m) - N k_B T \ln\left(\frac{V_n}{V_m}\right) \tag{3.20}$$

where $E_{nm} = E_n - E_m$, and V_n and V_m are the new and old volume respectively. The first two terms on the right hand side of (3.20) are the enthalpy change between m and n. Moves are then accepted with a probability

$$\wp = \min\left(1, \exp(-\frac{\delta H_{nm}}{k_B T})\right). \tag{3.21}$$

3.4.2.2 Molecular Monte Carlo

Monte Carlo simulations of molecules are performed in a similar manner to those of atomic systems. However, there are different degrees of freedom to consider and so additional Monte Carlo moves are required.

For rigid molecules it is necessary to consider orientational as well as translational degrees of freedom. These are usually combined into a single trial move consisting of a centre of mass translation and a rotation around the centre-of-mass. A translational move is performed by randomly displacing the centre of mass of the molecule. An orientational move is then performed by randomly changing the orientation of the molecule. In order to perform rotational moves, it is necessary to have a set of coordinates to describe the molecular orientation. One such set are the Euler angles [116]. These are described in terms of a sequence of rotations of a set of Cartesian axes about the origin. The first is through an angle ϕ about the z axis. This is followed by a rotation of θ about the new x axis and then a final rotation of ψ about the new z axis. The change in orientation can then be achieved through random changes in these angles.

For flexible molecules, changes to the internal coordinates occur along side translational and rotational moves. Again we need a set of coordinates to describe the molecular conformations. This is commonly done in terms of internal coordinates, the bond lengths, bond angles, and dihedral angles in each molecule. As for rigid molecules, these are usually combined into a single trial move. A Monte Carlo move for a flexible molecule could then consist of a centre of mass displacement, and rotation of the molecule about its centre of mass, and then a change in an internal dihedral angle, bond angle and bond length.

3.4.3 Molecular Dynamics

While the Monte Carlo method generates configurations from a particular ensemble at random, the molecular dynamics method generates configurations by solving

the classical equations of motion for a N body system interacting through a particular potential function $V(\mathbf{r}_1, ., \mathbf{r}_N)$. These equations of motion are then given by Newton's laws

$$m_i \frac{\partial^2 \mathbf{r}_i}{\partial t^2} = \mathbf{F}_i, \tag{3.22}$$

where $\mathbf{F}_i$ is the force of the i th particle and is found from

$$\mathbf{F}_i = -\nabla_i V(\mathbf{r}_1, .., \mathbf{r}_N). \tag{3.23}$$

The time evolution of the system is then determined by solving the second- order differential equation (3.22) for each particle in the system. This then gives rise to successive sets of coordinates and velocities.

The first molecular dynamics simulations where performed on hard discs (2-d) and hard spheres (3-d). In these simulations, the particles underwent free-flight between collisions. The collisions were perfectly elastic and the velocities of the particles after each collision were determined by applying the principles of conservation of momentum.

For more realistic models of particle interactions, the forces vary smoothly as a function of position. Under the influence of a continuous potential the motions of all the particles become coupled together, giving rise to a many body problem that cannot be solved analytically. Thus, a numerical approach, the *finite difference* method is used to solve the equations of motion.

The general idea of the *finite difference* approach is that time can be broken down into a series of discrete steps of length δt. Given the molecular positions and velocities at a time t we attempt to find these at a later time $t + \delta t$ with a sufficient accuracy. Then we can attempt to use these new positions and velocities to calculate positions and velocities at time $t + 2\delta t$. Thus the equations of motion are solved on a step-by-step basis.

3.4.3.1 Integration Algorithms

The step-by-step solution of the equations of motion using a finite difference approach is performed by the use of an integration algorithm. One common algorithm is the Verlet algorithm [59]. This is derived from a Taylor expansion of the positions about time t

$$\mathbf{r}(t+\delta t) = \mathbf{r}(t) + \mathbf{v}(t)\delta t + \frac{1}{2}\mathbf{a}(t)\delta t^2 \tag{3.24}$$

$$\mathbf{r}(t-\delta t) = \mathbf{r}(t) - \mathbf{v}(t)\delta t + \frac{1}{2}\mathbf{a}(t)\delta t^2. \tag{3.25}$$

Adding (3.24) and (3.25) gives

$$\mathbf{r}(t+\delta t) = 2\mathbf{r}(t) - \mathbf{r}(t-\delta t) + \mathbf{a}(t)\delta t^2. \tag{3.26}$$

As can be seen, the Verlet algorithm is time-reversible (i.e. $\mathbf{r}(t+\delta t)$ and $\mathbf{r}(t-\delta t)$ are interchangeable in (3.26). Also the velocities are absent from (3.26) but can be calculated from

$$\mathbf{v}(t) = \frac{\mathbf{r}(t+\delta t) - \mathbf{r}(t-\delta t)}{2\delta t}. \tag{3.27}$$

This is necessary for the calculation of the kinetic energy. (3.26) is accurate to order δt^4 while (3.27) is accurate to order δt^2. The Verlet algorithm is simple and compact to code and the time-reversal symmetry leads to good energy conservation. However, the velocities are not well handled. Also (3.26) involves the addition of a small number onto a large number, which can introduce numerical inaccuracies.

Two alternative formulations of the Verlet algorithm have been proposed to remedy this shortcoming. The first is the leapfrog algorithm

$$\mathbf{r}(t+\delta t) = \mathbf{r}(t) + \mathbf{v}\left(t+\frac{1}{2}\delta t\right)\delta t \tag{3.28}$$

$$\mathbf{v}\left(t+\frac{1}{2}\delta t\right) = \mathbf{v}\left(t-\frac{1}{2}\delta t\right) + \mathbf{a}(t). \tag{3.29}$$

Here the mid-step velocities are calculated using (3.29) and then these are using to calculate the new positions using (3.28). The velocity at time t may then be

calculated from

$$\mathbf{v}(t) = \frac{1}{2}\left(\mathbf{v}\left(t + \frac{1}{2}\delta t\right) + \mathbf{v}\left(t - \frac{1}{2}\delta t\right)\right). \tag{3.30}$$

Another alternative is the velocity Verlet algorithm. This takes the form

$$\mathbf{r}(t + \delta t) = \mathbf{r}(t) + \mathbf{v}(t)\delta t + \frac{1}{2}\mathbf{a}(t)\delta t^2 \tag{3.31}$$

$$\mathbf{v}(t + \delta t) = \mathbf{v}(t) + \frac{1}{2}[\mathbf{a}(t) + \mathbf{a}(t + \delta t)] \tag{3.32}$$

This is implemented in two stages. First the positions are advanced using (3.31). The mid-step velocities are then calculated from the acceleration at time t by

$$\mathbf{v}\left(t + \frac{1}{2}\delta t\right) = \mathbf{v}(t) + \frac{1}{2}\mathbf{a}(t)\delta t. \tag{3.33}$$

The accelerations at time $t + \delta t$ are then calculated and the velocity move is completed

$$\mathbf{v}(t + \delta t) = \mathbf{v}\left(t + \frac{1}{2}\delta t\right) + \frac{1}{2}\mathbf{a}(t + \delta t)\delta t. \tag{3.34}$$

3.4.3.2 Molecular Dynamics of Molecular Systems

Most molecules are non-spherical. Thus it becomes necessary to consider motions other than just centre of mass motion. How this is done depends on whether the molecules are treated as rigid units or are flexible. For a rigid molecule, it is natural to divide molecular motion into a centre of mass translation and a rotation about the centre of mass. The rotational motion is governed by a torque about the centre of mass. As in Monte Carlo simulations of rigid molecules, the orientation can be described by Euler angles. Alternatively the orientation can be described by the *quaternion* method. Here the orientation is described by a quaternion, a four dimensional unit vector (q_0, q_1, q_2, q_3). In terms of the Euler angles, the quaternions are defined as [115]

$$\begin{aligned} q_0 &= \cos\frac{1}{2}\theta\cos\frac{1}{2}(\phi + \psi) \\ q_1 &= \sin\frac{1}{2}\theta\cos\frac{1}{2}(\phi - \psi) \end{aligned}$$

$$\begin{aligned} q_2 &= \sin\frac{1}{2}\theta \sin\frac{1}{2}(\phi - \psi) \\ q_3 &= \cos\frac{1}{2}\theta \sin\frac{1}{2}(\phi + \psi)\,. \end{aligned} \tag{3.35}$$

The quaternion scheme is computationally simpler and avoids singularities that appear in the equations of motion for the Euler angles. The equations of motion for the quaternions can be solved using a modified leapfrog algorithm [115].

To simulate a realistic molecular system, the internal degrees of freedom, such as torsional motions, have to be accounted for. These torsional motions are important in long chain molecules. However, the internal degrees of freedom act over a range of different frequencies, from the fast bond stretching motions to the slower torsional motions. This wide range of motions leads to difficulties in simulating molecular systems: the fast bond stretching modes require a very short time step. Thus it is common to constrain certain degrees of freedom, commonly bond lengths, while others are left free to evolve under the influence of intra and intermolecular forces.

To constrain bond lengths in a MD simulation it is necessary to adjust the equations of motion to eliminate forces acting to change bond lengths. One such method for this is the SHAKE algorithm [117]. Here, the particles are moved under the influence of the unconstrained forces. The constraints are applied iteratively until the new positions of the atoms satisfies the constraints within a set tolerance.

3.4.3.3 Molecular Dynamics and Ensembles

As the above equations generate trajectories with constant energy (within computer accuracy), as it stands MD utilizes the microcanonical (NVE) ensemble. However, it is often of more interest to perform simulations in other ensembles, commonly the canonical (constant temperature NVT) ensemble or the isothermal-isobaric (constant pressure NpT) ensemble. To do this requires modifications to the standard equations of motion.

3.4.3.4 Constant Temperature (NVT) Molecular Dynamics

Simulations at constant temperature are important for studying the behaviour of systems at different temperatures. There have been a number of different approaches for performing constant temperature (NVT) MD. As the temperature of a system is related to the average kinetic energy of the particles, the temperature can be controlled by scaling the velocities, i.e. at each time step the velocities are scaled according to $\mathbf{v}' = \chi\mathbf{v}$. One such thermostat in this spirit is the Berensden thermostat [118]. Here the velocity rescaling parameter, χ, is given by

$$\chi = \left[1 + \frac{\delta t}{\tau}\left(\frac{T}{T_0} - 1\right)\right] \tag{3.36}$$

where δt is the time step, T is the current temperature, T_0 is the desired temperature, and τ is a time constant. Another method, similar to velocity rescaling is to constrain the velocities by a Gaussian constraint method [119, 120]. Alternatively, the temperature can be held constant by a heat bath. In this method, originally due to Anderson [121], the velocity of a randomly selected particle is replaced by one chosen from the Maxwell-Boltzmann distribution. This is equivalent to a collision with a particle in an imaginary heat bath.

A final possibility is the extended system method. Similarly to the Anderson thermostat, the system is assumed to be in contact with a heat bath. However, in this case the interaction between the simulated system and the heat bath is modelled by an interchange of energy between them. In the original formulation of this method due to Nosé [122], this was handled by an extended Hamiltonian, with an extra degree of freedom s, which acts as a time scaling parameter. Hoover then reformulated this without the extra degree of freedom [123]. The equations of motion for this thermostat are

$$\dot{\mathbf{r}} = \frac{\mathbf{p}}{m} \tag{3.37}$$

$$\dot{\mathbf{p}} = \mathbf{f} - \zeta\mathbf{p} \tag{3.38}$$

$$\dot{\zeta} = \frac{gk_BT_0}{Q}\left(\frac{T}{T_0} - 1\right), \tag{3.39}$$

where ζ is a friction coefficient, g is the number of degrees of freedom, and Q is the thermal inertia coefficient, which describes the rate of energy exchange between the system and the heat bath.

3.4.3.5 Constant Pressure (NpT) Molecular Dynamics

Many experiments are performed at constant temperature and pressure, so the isothermal-isobaric (NpT) ensemble is commonly used for MD simulations. Many of the methods used for controlling the temperature of a simulation can be adapted to control the pressure, with the pressure being controlled by changing the size of the simulation cell (see §3.5.1). The change in the simulation cell can be isotropic where the cell shape remains unchanged or anisotropic where the cell shape changes. One simple method due to Berensden *et al.* involves coupling the system to a pressure bath. At each step the volume of the box is scaled by a factor of η and so the centre of mass coordinates are scaled by a factor of $\eta^{\frac{1}{3}}$, i.e. $\mathbf{r}' = \eta^{\frac{1}{3}}\mathbf{r}$. The system is then made to obey the equation

$$\dot{P} = \frac{P_0 - P}{\tau_P} \tag{3.40}$$

where P is the current pressure, P_0 is the desired pressure, and τ_P is time constant.

Barostats in the spirit of the Nosé-Hoover thermostat have also been proposed. One such barostat that generates proper NpT ensemble averages has been proposed by Melchionna *et al* [124]. Here the equations of motion are given by

$$\dot{\mathbf{r}} = \frac{\mathbf{p}}{m} + \eta(\mathbf{r} - \mathbf{r}_{com}) \tag{3.41}$$

$$\dot{\mathbf{p}} = \mathbf{f} - (\eta + \zeta)\mathbf{p} \tag{3.42}$$

$$\dot{\zeta} = \frac{1}{\tau_T^2}(\frac{T}{T_0} - 1) \tag{3.43}$$

$$\dot{\eta} = \frac{1}{Nk_BT_0\tau_P^2}V(P - P_0) \tag{3.44}$$

$$\dot{V} = 3\eta V, \tag{3.45}$$

where $\mathbf{r}_{com}$ are the system centre of mass coordinates, and τ_T and τ_P are the thermostat and barostat time constants.

3.4.4 Monte Carlo or Molecular Dynamics

The choice between Monte Carlo and molecular dynamics is largely determined by the phenomenon under investigation. For a simulation of a gas or other low density systems, Monte Carlo simulations are preferable [125]. There can be large energy barriers (often several k_BT) to torsional rotations in molecules which can lead to molecules being trapped in a few low energy conformations in a MD simulation, leading to poor conformational sampling. In contrast, the random moves in a MC simulation can easily lead to barrier crossings. For a liquid simulation MD becomes favourable. Here molecular collisions exchange energy between molecules, enabling barrier crossings, improving the ability of MD to sample conformations. For a MC simulation, there is a large probability of selecting random moves for which two or more molecules overlap (especially for rotations near the centre of molecules with long tails such as liquid crystals), leading to large number of rejected moves and a decrease in efficiency of sampling. However, the ability of MC to make unphysical moves, for example to flip a molecule around, can in some cases compensate for this. MD also handles collective motions better than MC. However, recently methods such as Configurational Bias Monte Carlo and Hybrid Monte Carlo have been developed to improve the performance of MC simulations [126].

There are some situations where only one method is appropriate. Determination of transport properties such as viscosity coefficients, is largely only possible using MD, as MC lacks an objective definition of time (except in some special cases such as the bond fluctuation model for polymers). On the other hand MC can be used for simulations with varying particle numbers (Grand Canonical Monte Carlo) by adding moves for the creation and destruction of particles.

3.5 Practicalities

3.5.1 Periodic Boundary Conditions

Computer simulations using atomistic potentials are typically performed on small systems, usually of the order of a few hundred molecules. Assuming a simple cubic lattice, of 1000 molecules, 488 lie on the surface. These molecules would experience different forces than the other molecules. To try and counteract this surface effect it is common to invoke periodic boundary conditions. Here the system is surrounded by an infinite number of identical systems, as shown in Fig. 3.6. In the course of the simulation the molecules in each of the boxes move in the same way. Hence if a molecule leaves the simulation box at one side, an identical molecule enters the box at the other.

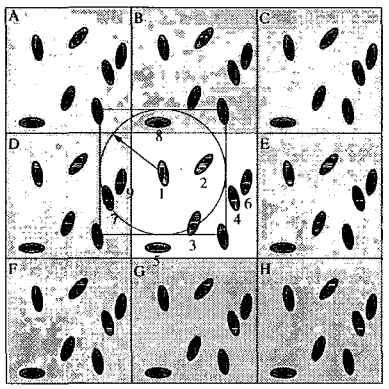

Figure 3.6: Periodic boundary conditions. The center box (white) is shown along with its first periodic images (shaded). The circle round molecule 1 is of radius $\frac{l_{box}}{2}$ while the box encompasses the nearest periodic image of each of the other molecules.

Periodic boundary conditions are usually used in conjunction with the minimum image convention for short ranged forces. Here we only consider interactions between each molecule and the closest periodic image of its neighbours. Short ranged forces are often truncated to increase computational efficiency (see next section). For consistency with the minimum image convention this cut-off distance must be less

than or equal to half the box length.

Periodic boundary conditions can sometimes have an effect on the system under consideration. This is especially pronounced for small system sizes and for properties with a large long range contributions, such as light scattering factors. They also inhibit long wavelength fluctuations that are important near phase transitions. However, they have little effect on equilibrium properties.

The most commonly shaped simulation cell is cubic or cuboidal. It is also possible to use cells of other shapes, such as the rhombic dodecahedron or the truncated octahedron. For studying surfaces it is common to retain periodicity in two dimensions, while discarding it in the direction perpendicular to the surface.

3.5.2 Long Range Interactions

Non-bonded interactions can be divided into two classes; short and long range interactions. Formally a force is defined to be short ranged if it decreases with distance quicker than r^{-d} where d is the dimensionality of the system (usually 3). Short ranged interactions are commonly dealt with by imposing a cut-off to the potential $V(r)$, r_c, beyond which $V(r)$ is set to 0. This can be justified by the speed at which a short range force decays with distance. As long as r_c is chosen to be sufficiently large, the cut-off will only imposes a slight perturbation on the system (although r_c has to be less than half the box length to be consistent with the minimum image convention). Correction formulae can be applied to quantities such as the pressure or energy to correct for this.

Long range forces present more of a problem. As they are infinite ranged, the simulation cell and all its periodic images must be considered. In principle for a large enough system screening by neighbouring molecules would diminish the effect of the potential. However, this would occur over a range of several tens or hundreds of nanometres while current simulations typically have box lengths of the order of nanometres. Thus to account for long range interactions in systems that can be

reasonably simulated we must consider the effect of the periodic images. In this case the Coulombic interaction for a set of point charges is

$$U_{coul} = \frac{1}{4\pi\epsilon_0} \sum_{\mathbf{n}} \left(\sum_{i=1}^{N-1} \sum_{j=i+1}^{N} q_i q_j |\mathbf{r}_{ij} + \mathbf{n}|^{-1} \right) \tag{3.46}$$

where $\mathbf{n}$ are the lattice vectors $\mathbf{n} = (n_x L_x, n_y L_y, n_z L_z)$. This sum is conditionally convergent; the result depends on the order the terms are summed in.

The Ewald sum [115, 127] is commonly used to model the effect of long range forces. It was originally developed for the study of ionic crystals. The Ewald sum decomposes the sum in (3.46) into two rapidly convergent sums

$$\sum \frac{1}{r} = \sum_{m} \frac{F(m)}{r} + \sum_{n} \frac{1 - F(n)}{r}. \tag{3.47}$$

Physically the Ewald sum works by surrounding each point charge in the system by a charge distribution of equal magnitude and opposite sign. This is commonly taken to be a Gaussian distribution, although this choice is arbitrary. The counter-charge screens the original potential making it short ranged. This is then summed in real space. Then a second imaginary charge distribution of opposite sign to the first (and of the same sign as the point charges) is added to cancel out the screening charge. As this screening distribution is a smooth function, its Fourier transform is rapidly convergent. Thus this second is summed in reciprocal space. Two further terms are present in the Ewald sum. The first is the *self* term. This cancels the interaction between a point charge and its own screening distribution and is a constant. The second is the *surface* term.This accounts for the dipolar layer that appears at the surface of a sphere in a vacuum. The final potential energy is then

$$\begin{aligned} U_{coul} &= \frac{1}{2} \sum_{i=1}^{N} \sum_{j=1}^{N} q_i q_j \frac{\mathrm{erfc}(\alpha|\mathbf{r}_{ij} + \mathbf{n}|)}{|\mathbf{r}_{ij} + \mathbf{n}|} \\ &+ \frac{1}{\pi L^3} \sum_{\mathbf{k} \neq \mathbf{0}} q_i q_j \frac{4\pi^2}{k^2} \exp\left(-\frac{k^2}{4\alpha^2}\right) \cos(\mathbf{k}.\mathbf{r}_{ij}) \\ &- \frac{\alpha}{\pi^{\frac{1}{2}}} \sum_{i=1}^{N} q_i^2 + \frac{2\pi}{3L^3} \left| \sum_{i=1}^{N} q_i \mathbf{r}_i \right|^2 . \end{aligned} \tag{3.48}$$

The Ewald sum is possibly the most common method for evaluating long-range interactions in simulations. However, it can be expensive for large systems due to its $\mathcal{O}(N^{\frac{3}{2}})$ scaling. Thus several, cheaper, alternative methods have been proposed. One such technique is the Particle-Particle Particle-Mesh method (PPPM) [128] which scales as $\mathcal{O}(N \ln N)$. In this interactions at short range are directly calculated. Interactions at long range are evaluated by interpolating the charges onto a mesh. The Poisson equation can then be solved on this mesh to calculate the potential and forces. There are several variants of this technique that use different methods for discretizing the charges onto a mesh [129]. Another set of alternatives to the Ewald sum are the Fast Multipole Methods (FMM). These work by breaking the system into cells. The potential and force on each molecule are evaluated by considering the interaction between the molecule and each of these cells, where the distribution of charges in each of these cells are approximated by a multipole expansion. For a large enough system size this has been shown to scale as $\mathcal{O}(N)$, although due to a large prefactor, these methods only become favourable for systems of about 100000 particles [130]. Another alternative to the Ewald sum is the reaction field method [115, 131]. Here contributions from molecules within a cavity of radius r are calculated explicitly. Molecules outside this are considered to form a dielectric continuum producing a reaction field within the cavity.

3.6 Analysis of Simulation Data

After a simulation is performed the accumulated data has to be analysed to produce useful information. While calculating specific quantities can require some very specialized analysis, some quantities calculated from simulation are quite general and are outlined below.

3.6.1 Radial Distribution Functions

The structure of a liquid can be characterized by a radial distribution function (RDF) $g(r_i, r_j)$. This gives the probability of finding a molecule, i, at a position r_i and a molecule, j, at a position r_j. For a simple liquid this becomes $g(r_{ij})$ where r_{ij} is the intermolecular separation. $g(r_{ij})$ is defined to be

$$g(r_{ij}) = \frac{V}{N^2} \langle \delta(r - r_{ij}) \rangle \tag{3.49}$$

where $\delta(r)$ is the Dirac delta function. The $\frac{V}{N^2}$ prefactor normalizes the RDF relative to an ideal gas of the same density. For use in a simulation, the delta function is replaced by a function that is equal to one when the separation is in the range $r - \delta r, r + \delta r$ and equal to zero otherwise. An example RDF is shown in Fig. 3.7. For a liquid crystal it is common to calculate the components of the RDF parallel

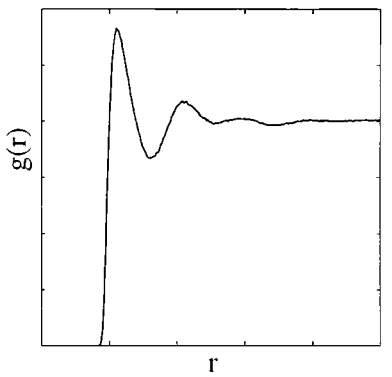

Figure 3.7: Example radial distribution function

and perpendicular to the director, $g_{\parallel}(r)$ and $g_{\perp}(r)$. $g_{\parallel}(r)$ is useful for identifying smectic phases; the layer structure of smectic phases shows up as a periodic variation of $g_{\parallel}(r)$, while $g_{\perp}(r)$ identifies smectic phases with in-layer order.

For an atomistic model it is possible to define $g(r)$ either in terms of the molecular centre-of-mass or in terms of site-site RDFs with a different RDF for each possible combination of atom types. Thus for a simulation of water, there would be three different RDFs $g_{OO}(r)$, $g_{OH}(r)$, and $g_{HH}(r)$. These are related to the structure factor of the fluid and hence to observable quantities.

3.6.2 Orientational Correlation Functions

For systems made up of non-spherical molecules it is possible to calculate orientational (OCF) or angular correlation functions that depend on the relative orientations of the molecules. OCFs of interest include

$$g_l(r) = \langle P_l(\cos\gamma_{ij})\rangle_{r-\delta r, r+\delta r}\ ,\ l = 1, 2 \tag{3.50}$$

where γ_{ij} is the angle between the axes of the ith and jth molecules. $g_1(r)$ is related to the dielectric properties of polar liquids [132], while $g_2(r)$ is related to the scattering of depolarized light [133, 134]. Both are evaluated from simulation in a similar manner to the RDF.

3.6.3 Nematic Director and Order Parameters

As described in §1.3 the nematic phase is characterized by a preferred direction $\mathbf{n}$ and an order parameter $\bar{P}_2$. These can be found from the second rank ordering tensor (§1.3)

$$Q_{\alpha\beta} = \frac{1}{N_m}\sum_{i=1}^{N_m}\frac{3}{2}\hat{u}_{i\alpha}\hat{u}_{i\beta} - \frac{1}{2}\delta_{\alpha\beta} \tag{3.51}$$

where $\hat{\mathbf{u}}$ is a unit vector associated with each molecule and N_m is the number of molecules. The nematic director is the eigenvector associated with the largest eigenvalue of $Q_{\alpha\beta}$, which is usually taken to be $\bar{P}_2$. $\bar{P}_2$ is sometimes defined to be the middle eigenvalue multiplied by minus two [15].

For a rigid molecule $\mathbf{u}$ is easily defined in terms of the molecular axes. For flexible molecules a number of definitions have been used [135]. Probably the most common is to identify the molecular axis with the long axis found from the inertia tensor

$$I_{\alpha\beta} = \sum_{i=1}^{N_a} m_i(r_i^2\delta_{\alpha\beta} - r_{i\alpha}r_{i\beta}) \tag{3.52}$$

where $\mathbf{r}_i$ and m_i are the positions relative to the molecular centre-of-mass and the masses of the atoms respectively, and the sum runs over all the atoms in a particular

molecule. The long axis **u** is then the eigenvector associated with the smallest eigenvalue of $I_{\alpha\beta}$. Alternatively for polar molecules the molecular axis can be identified with the dipole axis or from the bond polarizabilty tensor [135]. A final method involves associating the molecular axis with a particular group within the molecule. This can be extended to finding the order parameters for different groups within a molecule [136].

The orientational distribution function (ODF) can be found from simulation in a similar manner to the RDF. Once the director is known, $\hat{\mathbf{u}}.\mathbf{n}$ can be calculated and collected into histogram bins.

3.6.4 Diffusion

Fluid states can be distinguished from solid states by monitoring the rate at which molecules diffuse through the system, which is measured by the diffusion coefficient D. From simulation D can be calculated in two ways. The first involves integrating the velocity auto-correlation function

$$D = \frac{1}{3}\int_0^\infty \langle \mathbf{v}(t).\mathbf{v}(0)\rangle \, dt, \tag{3.53}$$

where $\mathbf{v}(t)$ is the centre-of-mass velocity of a molecule. The second uses the corresponding Einstein relation

$$2tD = \frac{1}{3}\left\langle |\mathbf{r}(t) - \mathbf{r}(0)|^2 \right\rangle, \tag{3.54}$$

where $\mathbf{r}(t)$ is the centre-of-mass position of a molecule. To improve statistics both (3.53) and (3.54) are averages over all molecules in the system and over many different time origins. When using (3.54) care must be taken to avoid switching attention between periodic images of the same molecule. For liquid crystals the centre-of-mass diffusion can be separated into components parallel and perpendicular to the director and so two different diffusion coefficients, $D_{\parallel}$ and $D_{\perp}$, can be defined.

3.7 Use of Simulation Techniques

In the following chapters many of the simulation techniques described in this chapter will be employed. For the validation of the force field parameters calculated in chapter 4, liquid state molecular dynamics simulations using the NpT ensemble are used. Gas phase simulations using the Monte Carlo method are also used. In chapters 5 and 6 molecular dynamics simulations of the mesogen PCH5 are performed, also in the NpT ensemble. For the MD simulations, temperature and pressure are controlled using the Nosé-Hoover thermostat and the Hoover barostat. All simulations use fully atomistic potentials, with long-range electrostatic interactions evaluated using the Ewald sum.

Chapter 4

Parameterization and Validation of a Force Field for Liquid Crystal Molecules

4.1 Introduction

There has been much interest in simulating bulk phases of materials, such as liquids and liquid crystals. While much work has been done using simple single site potentials, recent increases in computer power has led to a large number of studies of bulk liquid crystal phases using atomistic potentials [100, 137, 138]. At the heart of an atomistic simulation is the potential, often called a *force field.* Using a force field, the energy of the molecule and the forces on its constituent atoms can be calculated from atomic positions. This is a fully classical potential, the electrons being considered implicitly in terms of the potential field or *potential energy surface* on which the atoms move: a great simplification compared to quantum mechanical calculations.

4.2 The Molecular Mechanics Force Field

For any calculation in science a model must be constructed, which must in some way approximate reality. The underlying model for a molecular mechanics calculation, as well as classical atomistic MD or MC simulations, is that the energy of a molecule can be described in terms of a function called the *force field* that depends only on the atomic positions, a highly simplifying assumption. Obviously this function must provide a good description of the forces acting within the molecule. For organic molecules one such function is the valence force field [114], by which the energy of the molecule may be determined in terms of the internal co-ordinates, bond lengths, bond angles, dihedral angles, as well as the Cartesian co-ordinates of the atoms. This is illustrated schematically in Fig. 4.1. Due to the ubiquity of the valence force field, the term force field is usually taken to refer to a valence force field.

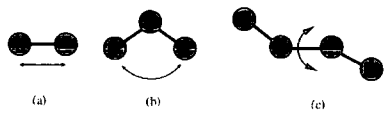

Figure 4.1: Schematic diagram of force field terms. a) Bond stretching, b) bond angle bending, and c) dihedral rotation.

There are many different force fields which use different forms for the various interactions within and between molecules. The particular form of a force field depends on the accuracy required for its intended purpose and this will be discussed further in §4.3. Force field parameters can be found from either experimental or theoretical data and methods for this are discussed in §4.4. A key property for both the force field form and the force field parameters is that those for a particular atom or group of atoms should be the same for different molecules, i.e. they should be *transferable*. Without this property a different force field would have to be constructed for each different molecule. This notion of transferability underlies much of chemistry and can be seen to hold in many cases. For example the stretching

frequencies of carbon-hydrogen bonds are largely independent of molecular environment, as are C-H bond lengths. Subdividing these into bonds between hydrogen and carbon atoms with different hybridisations leads to even stronger agreement.

4.3 Functional Form of a Force Field

4.3.1 Bond Stretching Interactions

To find a functional form for bond stretching interactions it is helpful to consider how the energy of a bond changes with its length. The energy of a bond is lowest at a particular *natural* or *reference* length. If the bond is then compressed the electron clouds of the two atoms forming it will gradually overlap. This leads to a rapid increase in energy. If the bond is stretched beyond equilibrium the energy starts to increase. Eventually however, the bond disassociates. A plot of this is shown in Fig. 4.2. For small deviations from the equilibrium bond length the energy can be written as a Taylor expansion in $r - r_0$, with r_0 representing the equilibrium bond length

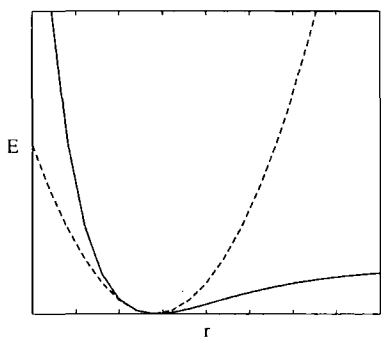

Figure 4.2: Potential energy curve for a bond stretch (bold line). The dotted line shows the harmonic approximation to the bond stretching potential

$$E(r) = E(r_0) + \left.\frac{dE}{dr}\right|_{r=r_0} (r-r_0) + \frac{1}{2}\left.\frac{d^2E}{dr^2}\right|_{r=r_0} (r-r_0)^2 + \frac{1}{6}\left.\frac{d^3E}{dr^3}\right|_{r=r_0} (r-r_0)^3 + \ldots \quad (4.1)$$

In its simplest form (4.1) is terminated at the $(r - r_0)^2$ term. This is called the harmonic approximation. Setting $E(r_0) = 0$, and noting that at $r = r_0$ the force and hence first derivative of the energy is zero, we have

$$E_{str}(r) = \frac{1}{2}k_r(r - r_0)^2 \tag{4.2}$$

where k_r is the harmonic force constant given by

$$k_r = \left.\frac{d^2E}{dr^2}\right|_{r=r_0}. \tag{4.3}$$

The reference bond length r_0 is often called the *equilibrium* bond length. This is slightly misleading as the reference bond length is the bond length when all the other force field terms are set to 0, while the *equilibrium* bond length is the bond length for the minimum energy configuration of the molecule (i.e. when $E_{ff} = 0$).

The forces between bonded atoms are very high in comparison to other forces. This is the justification for using the harmonic approximation. It is important to remember that this is an approximation to the *real* bond stretching potential and that for large deviations from r_0 the harmonic approximation no longer holds true. For situations where the bond lengths may deviate far from r_0 or to accurately calculate molecular structures and vibrational frequencies it is necessary to go beyond the harmonic approximation and include higher order terms usually up to $(r - r_0)^4$. While increasing the range of validity of (4.1), $E(r)$ will still tend to ∞ as $r \to \infty$, so it remains unphysical. One potential which satisfies the exact conditions outlined above is the Morse potential [139]

$$E_{str}(r) = D\left(1 - \exp(-\alpha(r - r_0))\right)^2 \tag{4.4}$$

where D is the dissociation energy and $\alpha = \sqrt{\frac{k}{2D}}$.

4.3.2 Bond Angle Bending Interactions

For bond angle bending it is also common to use a harmonic potential

$$E_{bend}(\theta) = \frac{1}{2}k_\theta(\theta - \theta_0)^2, \tag{4.5}$$

where k_θ is the angle bending force constant, θ is the actual bond angle and θ_0 is the reference bond angle. The energy needed to distort an angle away from equilibrium is much lower than that needed to distort a bond, so consequently bond angle bending force constants tend to be proportionally smaller than those for bond stretching. As with the bond stretching potential, the accuracy can be improved by including higher order terms.

4.3.3 Torsional Angle Interactions

Torsional angle rotations are arguably the most important of the intramolecular terms in a force field. As such it is surprising that some early force fields omitted torsional angle interactions and instead tried to model rotational barriers by a combination of non-bonded interactions. Torsional angle interactions are different to stretching and bending interactions in two important ways. The first is that internal rotation barriers are low compared to other interactions, meaning that changes in dihedral angles can be large, and secondly the torsional potential, E_{tors} is periodic through a 360° rotation. The former implies that it would be inappropriate to approximate E_{tors} by a Taylor series. In addition the E_{tors} can take on very different forms depending on the atoms forming it. Thus the functional form chosen should be able to model a wide variety of different potentials.

It is most common to model the torsional interaction using a Fourier series

$$E_{tors}(\tau) = \sum_n \frac{1}{2} V_n \cos(n\tau) \tag{4.6}$$

where V_n are the torsional rotation force constants and τ is the current torsional angle. It is customary to shift the zero of the potential and to include phase factors giving

$$E_{tors}(\tau) = \sum_n \frac{1}{2} V_n (1 + \cos(n\tau + \delta_n)). \tag{4.7}$$

The phase angles δ_n are usually chosen so that terms with positive V_n have minima at 180° (i.e. for odd n $\delta_n = 0°$ and for even n $\delta_n = 180°$). The first three of these

are shown in Fig. 4.3.

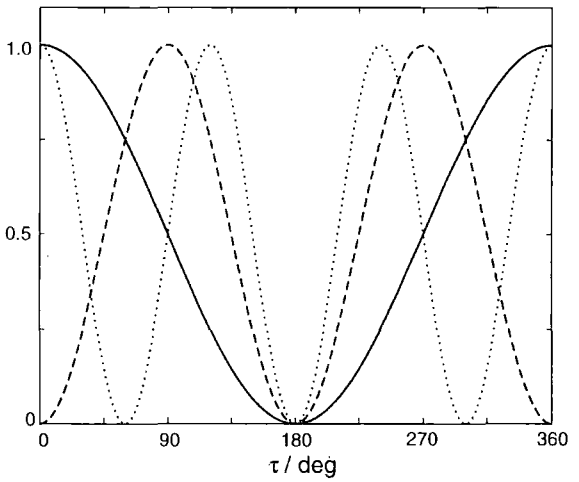

Figure 4.3: $n = 1$ (bold), $n = 2$ (dashed), and, $n = 3$ (dotted) Fourier components

The number of terms needed in the Fourier series depends on the complexity of the torsional potential and the desired accuracy. For modelling organic compounds three terms are generally used in the series. The symmetry of particular molecular fragments can result in some of the V_n being zero.

Closely related to the torsional interaction are the out-of-plane bending interactions. If we take four atoms (A,B,C,D) that form three angles (A-B-C, A-B-D, and C-B-D) then there can be an energy cost for moving B off the plane formed by A, C, and D. This can be accounted for in force fields in one of two main ways. The first approach uses a harmonic potential of the form

$$E_{oop} = \frac{1}{2} k_{oop} \chi^2, \tag{4.8}$$

where χ is the angle between the plane containing the atoms A, C, and D and the A-B, B-C, and B-D bonds. The second approach models E_{oop} as an improper torsion using a Fourier series potential as in (4.7) usually only retaining the $n = 2$ term.

The angles τ and χ used to define the torsional rotation and out of plane bending angles are shown in Fig. 4.4.

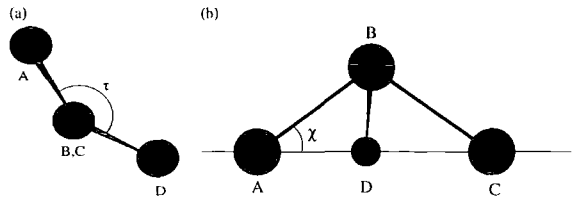

Figure 4.4: Definition of angles (a) τ in torsional rotations and (b) χ in out of plane bending.

4.3.4 Non-bonded Interactions

In addition to the bonded interactions between atoms described above, force fields also contain non-bonded interactions. Non-bonded interactions act between atoms in the same molecule and those in other molecules. Force fields usually divide non-bonded interactions into two: electrostatic interactions and Van der Waals interactions.

The electrostatic interaction arises due to the unequal distribution of charge in a molecule. A simple example is the hydrogen fluoride (HF) molecule, where the hydrogen atom is slightly positive and the fluorine is slightly negative. Within the force field framework this uneven distribution of charge can be modelled by placing point charges at each of the atomic sites. Due to charge conservation for a neutral molecule these sum to zero. Thus in the previous example we would have $q_F = -q_H$. The interaction between these point charges is generally modelled by a Coulomb potential

$$E_{elec} = \frac{1}{4\pi\epsilon_0}\frac{q_i q_j}{r_{ij}} \tag{4.9}$$

where ϵ_0 is the permitivitty of free space, q_i are atomic charges, and r_{ij} is the distance between i and j. An alternative approach used in some force fields is to model the electrostatics using point dipoles on the atoms or bonds. This can be extended by placing point multipoles on the atomic sites, a method called *Distributed Multipole Analysis* (DMA) [140].

Within a force field framework, the van der Waals interaction is commonly taken

consist of the all the interactions between atoms (or molecules) that are not covered by the electrostatic interaction [114][1] .Thus in this case it includes dispersion, repulsion, and induction, among other interactions [140]. The dispersion interaction arises due to correlations between electrons in different atoms. This leads to a lowering of the energy and hence an attraction. The repulsion interaction arises when the electron clouds of two atoms or molecules overlap. This arises from Coulomb repulsion between the electrons as they are all negatively charged and from the exclusion principle. The induction interaction arises due to the distortion of the charge distribution of an atom or molecule in the field of its neighbours.

To obtain a reasonable functional form for E_{vdw} it is again constructive to consider its behaviour with distance. At small distances the atomic repulsion leads to large positive values of E_{vdw} that tend toward infinity as the distance goes to zero. At large distances the dispersion interaction gives small negative values that go to zero as the distance goes to infinity. One of the most common forms for E_{vdw} that encompasses this behaviour is the Lennard-Jones (LJ) potential [69], which has the form

$$E_{vdw}^{LJ} = \frac{A_{ij}}{r_{ij}^{12}} - \frac{C_{ij}}{r_{ij}^{6}}, \tag{4.10}$$

where A_{ij} and C_{ij} are suitable constants. E_{vdw}^{LJ} can alternatively be given as

$$E_{vdw}^{LJ} = 4\epsilon_{ij}\left[\left(\frac{\sigma_{ij}}{r_{ij}}\right)^{12} - \left(\frac{\sigma_{ij}}{r_{ij}}\right)^{6}\right], \tag{4.11}$$

where ϵ_{ij} is the Van der Waals well depth and σ_{ij} is the distance at which $E_{vdw}^{LJ} = 0$. σ_{ij} is related to the minimum energy distance r_{ij}^{*} by

$$r_{ij}^{*} = 2^{\frac{1}{6}}\sigma_{ij}. \tag{4.12}$$

[1]There is considerable confusion over the precise definition of the Van der Waals interaction. Three different definitions can be used. The first is that the Van der Waals interaction consists of the London (dispersion) interaction. The second, quoted by Stone (c.f. pg. 2, [140]) is the Van der Waals interaction consists of all attractive and repulsive forces between molecules. The third, and the one used throughout this thesis, is that the van der Waals interaction are all the non-bonded interactions that are not directly electrostatic [23, 114].

The constants in (4.10) are related to ϵ_{ij} and σ_{ij} by $A_{ij} = 4\epsilon_{ij}\sigma_{ij}^{12}$ and $C_{ij} = 4\epsilon_{ij}\sigma_{ij}^{6}$. The r^{-6} dependence of the dispersion term arises from considering the interaction between two point multipoles and only considering the leading dipole-dipole term. Averaging this over all orientations gives a r^{-6} behaviour. There are no physical arguments for choosing the repulsive term to vary as r^{-12}: this arises due to computational expediency.

A more rigorous choice for the repulsive part of the potential would be an exponential term. The repulsive potential is dominated by the overlap between electron clouds on different atoms. As the electron density falls off roughly exponentially with distance from the nuclei, this repulsive interaction should have an exponential dependence with distance [140]. This leads to the Hill or Buckingham potential [141]

$$E_{vdw}^{Hill} = A_{ij} \exp\left(-B_{ij} r_{ij}\right) - \frac{C_{ij}}{r_{ij}^{6}}. \tag{4.13}$$

where A_{ij}, B_{ij}, and C_{ij} are constants. As can be seen in (4.13) E_{vdw}^{Hill} retains the long range r^{-6} dependence of the Lennard-Jones potential. As $r \to 0$ the Hill potential goes through a maxima then rapidly falls to $-\infty$.

One final form occasionally used for E_{vdw} is the Morse potential (4.4). While this abandons the explicit r^{-6} dependence for the dispersion interaction, this is included within the exponential term, along with the other terms in the induced multipole-induced multipole series. Fig. 4.5 shows the Lennard-Jones, Hill, and Morse potentials.

As well as acting between atoms on different molecules, the non-bonded interactions also act between atoms within the same molecule. However atoms in the same molecule can occasionally become very close to each other, leading to large values for the non-bonded energy and forces, especially Van der Waals, so special measures are some times needed to accommodate this. Atoms that are bonded to one another, 1-2 bonded, normally have their non-bonded interactions neglected, as are atoms that are bonded to a common atom, 1-3 bonded, although sometimes these are considered; when considered these are often called Urey-Bradley terms [114].

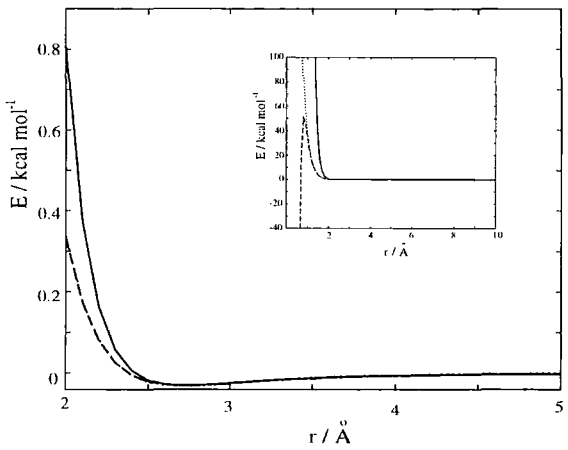

Figure 4.5: Plot of Lennard-Jones (solid line) and Hill (dashed line) potentials in the vicinity of the potential minima. Inset shows behaviour of the Lennard-Jones, Hill, and Morse potentials as $r \rightarrow 0$. In the inset the Morse potential is shown by the dotted line, while the Lennard-Jones and Hill potentials are the same as in the main figure.

The treatment of atoms that are 1-4 bonded, i.e. the two outermost atoms in a dihedral, varies from force field to force field. When the non-bonded interactions between these atoms are included they are often scaled by a factor to prevent the Van der Waals interaction overwhelming the torsional interaction.

4.3.5 Other Terms

While the above terms are common to all force fields and are often able to determine structures in a satisfactory manner, occasionally other terms are present in force fields to account for effects not covered by the terms above.

One common group of extra terms are cross terms. They describe coupling between different internal degrees of freedom. As an example of this consider the water molecule. If the H-O-H angle is squeezed, the H-O bonds stretch slightly due to repulsion between the hydrogens. Cross terms can be added to the potential to account for these effects. These are usually written as Taylor series of the individual

co-ordinates. For example the stretch-bend potential for the MM3 force field for a bond angle consisting of atoms i, j, and k is [142]

$$E_{sb} = 2.5228 k_{sb}(\theta_{ijk} - \theta_{ijk0})\left[(r_{ij} - r_{ij0})(r_{jk} - r_{jk0})\right] \tag{4.14}$$

where k_{sb} is the stretch-bend force constant. In (4.14) θ_{ijk} and θ_{ijk0} are the current and reference bond angles and r_{ij} and r_{ij0} are the current and reference bond lengths. The factor of 2.5228 in (4.14) is a conversion factor (k_{sb} is in mdyne Å^{-2} and E_{sb} is in kcal mol^{-1}). Other terms describing coupling between other internal motions can also be used.

Another modification made to some force fields describes electronegative or conjutative effects. This is the modification of an interaction between atoms by another atom not directly involved. For example C-C bonds become shortened if an electronegative atom is bonded to either carbon atom. This effect can be modelled by changing the reference bond length

$$r_{ij0} = r_{ij0} + \delta r_k. \tag{4.15}$$

4.3.6 Choosing the Form of a Force Field

The precise form of a force field is strongly influenced by the accuracy needed for its intended purpose. Some force fields are intended for simulations of bulk phases (e.g. the AMBER force field [143]. These generally have a simple form with harmonic terms for bond stretching and bending and usually a Lennard-Jones term for the Van der Waals interaction. Other force fields such as the MM4 force field [144–147] of Allinger are designed to determine structures and vibrational frequencies. Thus more accurate high order polynomials are used for bond stretches and bends and a Hill potential (or occasionally a Morse potential) is used for the Van der Waals interaction. There are many different terms for these different types of force fields. Simple force fields are often termed class 1 force fields or diagonal force fields. The latter comes from spectroscopy, the only non-zero terms in the force constant matrix

being on the diagonal. More complicated force fields are often termed class 2 and class 3 force fields.

Another decision to be made in regard to the form of a force field is whether all atoms will be considered (an all-atom force field) or whether unimportant atoms, usually hydrogens, are neglected (an united-atom force field). These neglected atoms are accounted for by increasing the size of the atoms they are bonded to, usually by increasing the Van der Waals radius. This provides a large saving in computer time. This can be taken further by replacing entire groups of atoms by a single site [88, 91] and logically leads to hybrid models, such as the Lennard-Jones-Gay-Berne (LJ-GB) model. Neglecting the hydrogen atoms, however leads to a poorer representation of electrostatic effects, such as the charge separation around phenyl rings. An interesting compromise used by Glaser *et al.* [148] is to use an all atom description for hydrogen atoms bonded to phenyl rings and a united atom description for hydrogen atoms in aliphatic groups.

4.4 Force Field Parameterization

Once a particular form for a force field has been chosen, the force parameters have to be determined. Even for a simple force field to be used for modelling a small number of systems this can be a large undertaking. For example to parameterize a simple diagonal force field for alkane molecules there needs to be:

- two parameters (force constant and equilibrium bond length) for the two different bond types (C-C and C-H),
- two for each of the three different angle types (C-C-C, C-C-H, and H-C-H),
- three for each different dihedral type (C-C-C-C, H-C-C-C, H-C-C-H),
- two Van der Waals parameters for the three different combination of atoms (C-C, C-H, H-H)

- up to five different charges.

So twenty-five different parameters are needed for a force field with only two atom types. For a more complicated force field with more atom types, the number of different parameters needed grows rapidly. For example, the MM2 force field [149] has 3722 different parameters for 30 atom types [23].

These parameters have to be chosen against some model of *reality*. Traditionally this is taken from experimental data. For some molecules, such as alkanes, experimental data is plentiful. For other classes of molecules data is more scarce. Even when experimental data is available, some force field parameters can be hard to determine from it. Bond lengths and angles can be determined from crystallography. Van der Waals can be determined from crystal structures. However, torsional potentials can be hard to determine, as are atomic charges.

Recently some force fields have been parameterized using data from electronic structure calculations, e.g. the Merck Molecular Force Field [150] or the Quantum Mechanical Force Field [151]. This allows the determination of force field parameters for molecules where little or no data exists. It also allows the determination of parameters in a consistent fashion. Whereas experimental data relevant to one set of parameters may be available in the gas phase, while that for another may be available for a solid, parameters from electronic structure calculations can all be found from the same phase (usually the gas phase). This can be important as there can be large differences in molecular structure in different phases. For example the dihedral angle in biphenyl is planar in the crystal while in the liquid and gas phase it is around 45°. Full torsional potentials can be determined from electronic structure calculations. Partial atomic charges can also be found from calculations. However, there are several different methods to find charges, with little agreement between them [152].

The hardest parameters to determine, whether from experimental or quantum chemical data, are the Van der Waals parameters. As these determine intermolecular

interactions these are highly important for determining condensed phase properties. Van der Waals parameters are often found from experimental crystal structures. They can also be calculated from high level (correlation corrected) *ab initio* calculations. However, Van der Waals parameters calculated from gas phase *ab initio* calculations can neglect interactions involving three or more atoms (3-body interactions). These can have a large contribution to the energy of a system, so neglecting these leads to large errors in the calculated values of some quantities. Another method has been used by Jorgensen *et al* in deriving the Optimized Parameters for Liquid Simulation (OPLS) parameter set [153, 154]. Here initial guesses were made for the Van der Waals parameters. Monte Carlo simulations were then performed on pure liquids and the Van der Waals parameters were adjusted to reproduce experimental values of thermodynamic quantities such as density and heats of vapourisation. As these parameters were fit to condensed phase properties, they implicitly include many body interactions. They are often referred to as *effective two body* potentials.

4.5 Review of Current Force Fields

Since the first force fields were developed there have, in the main, been two strands. The first strand aims to make accurate predictions of molecular structures and properties. This is exemplified by the work of Allinger and co-workers in the development of the Molecular Mechanics force fields. The early members of this family, MM1 [155], MM2 [149], have been largely superseded by the MM3 [142, 156, 157] and MM4 force fields [144–147]. These have been parameterized against experimental data, specifically heats of formation and vibrational frequencies. To accurately reproduce experimental results a complicated functional form is needed. The MM3 force field has a total of nine different interactions [142], with stretch-bend, stretch-torsion, and bend-bend interactions in addition to the five common to all force fields. The MM4 force field has another six in addition to these; a stretch-stretch, torsion-

bend, bend-torsion-bend, torsion-torsion, torsion-improper torsion, and improper torsion-torsion-improper torsion interactions [145]. In addition the Van der Waals is modelled using the Hill potential (4.13).

The second strand of force field development is aimed at modelling large molecules such as proteins or polymers. Typical force fields in this category are the AMBER [143,158], CHARMM [159] and the OPLS force fields [153]. By necessity these have simpler functional forms, usually only containing those terms described in §4.3.1-§4.3.4 and often employing the united atom approximation. The interaction potentials for bond stretching and bending tend to be restricted to the harmonic approximation, while Van der Waals interactions are modelled using the simpler Lennard-Jones potential. Despite their simplicity force fields such as these can often give good results for condensed phase properties, including thermodynamic properties such as heats of vapourisation or densities.

There have been some attempts to bridge the gap between the two types of force fields. An example of this is the Merck Molecular Force Field (MMFF) [150, 160–165]. In terms of complexity it lies between the simple forms used for the AMBER style force fields and the more complicated MM3/MM4 form. It uses one cross term to describe bend-stretch interaction and uses quartic and cubic forms for bond stretching and bending respectively. Unlike most other force fields it is parameterized completely from *ab initio* calculations. It has been shown to perform well (better than MM3) in calculation of structures of small organic molecules [165]. However in condensed phase simulations it performs poorly; this is due to the neglect of condensed phase effects, such as induction, in the parameterization.

4.6 Derivation of a Force Field for Liquid Crystal Molecules

4.6.1 Functional Form of the Force Field

As mentioned above the form of a force field is largely determined by its intended use. Our force field is intended for use in simulations of liquid and liquid crystalline phases so it should be appropriate for the use with large (about 200 molecules) systems. Thus a harmonic form, such as that used in the AMBER force field [143], is appropriate.

The force field has the following form

$$E_{ff} = \sum_{bonds} E_{ij}^{stretch} + \sum_{angles} E_{ijk}^{bend} + \sum_{dihedrals} E_{ijkl}^{tors} + \sum_{pairs} E_{ij}^{coul} + \sum_{pairs} E_{ij}^{vdw}. \quad (4.16)$$

The individual terms are as follows

Bond Stretching

$$E_{ij}^{stretch} = \frac{1}{2} k_{ij}^{stretch} \left(r_{ij} - r_{ij0}\right)^2 \quad (4.17)$$

where k_{ij} is the force constant for the i-j bond, r_{ij} is the i-j bond length, and r_{ij0} is the reference bond length for the i-j bond.

Bond Angle Bending

$$E_{ijk}^{bend} = \frac{1}{2} k_{ijk}^{bend} \left(\theta_{ijk} - \theta_{ijk0}\right)^2 \quad (4.18)$$

where k_{ijk} is the force constant for the i-j-k bond angle , θ_{ijk} is the i-j-k bond angle, and θ_{ijk0} is the reference bond angle.

Torsional Rotation

$$E_{ijkl}^{tors} = \sum_n \frac{1}{2} V_{ijkln}^{tors} \left(1 + \cos\left(n\phi + \delta_n\right)\right) \quad (4.19)$$

where V_{ijkln} is the nth order force constant for the i-j-k-l dihedral, ϕ_{ijkl} is the dihedral angle, and δ_n is the phase angle. The sum in (4.19) runs up to $n = 12$ for some dihedrals. δ_n is set so that terms with positive V_{ijkln} have minima at 180°. Thus

$$\delta_n = \begin{cases} 0^\circ \ , \ n \text{ odd} \\ 180^\circ, \ n \text{ even} \end{cases} . \tag{4.20}$$

Out of plane bending interactions also use the above form with only the $n = 2$ term.

Electrostatic Interaction

$$E_{ij}^{elec} = \frac{1}{4\pi\epsilon_0}\frac{q_i q_j}{r_{ij}} \tag{4.21}$$

where q_i are atomic charges and r_{ij} is the inter-atomic distance. The electrostatic interaction is neglected for atoms sharing a common bond or bond angle. For atoms sharing a common dihedral the electrostatic interaction is scaled by a factor of 0.125.

Van der Waals

$$E_{ij}^{vdw} = 4\epsilon_{ij}\left[\left(\frac{\sigma_{ij}}{r_{ij}}\right)^{12} - \left(\frac{\sigma_{ij}}{r_{ij}}\right)^{6}\right] \tag{4.22}$$

where ϵ_{ij} is the Van der Waals well depth for i and j and σ_{ij} is the distance at which $E_{ij}^{vdw} = 0$. ϵ_{ij} and σ_{ij} are found from the ϵ_i and σ_i using the mixing rules

$$\epsilon_{ij} = \sqrt{\epsilon_i \epsilon_j} \tag{4.23}$$

$$\sigma_{ij} = \sqrt{\sigma_i \sigma_j}. \tag{4.24}$$

For the case when i or j are fluorine atoms the Lennard-Jones form above is replaced by a Hill potential [23]

$$E_{ij}^{vdw} = \epsilon_{ij}\left[\frac{6}{\alpha - 6}e^{\alpha\left(1 - \frac{r_{ij}}{6\sqrt{2}\sigma_{ij}}\right)} - \frac{2\alpha}{\alpha - 6}\left(\frac{\sigma_{ij}}{r_{ij}}\right)^{6}\right] \tag{4.25}$$

where the free parameter $\alpha = 12$ is chosen to reproduce the long range behaviour of the Lennard-Jones potential. As with the electrostatic interaction, the van der

Waals interaction is neglected for 1-2 and 1-3 bonded atoms, and it is scaled by 0.5 for 1-4 bonded atoms.

4.6.2 Calculation of Conformational Energies

Due to the large number of parameters needed for the force field and the desire to use it to make accurate predictions of material properties, the methodology used to derive the parameters should be accurate and computationally inexpensive. Here a methodology based on *ab initio* calculations is used. Structures and conformational energies were computed using density functional theory calculations [26, 27]. A plane wave basis set was used for the valence electrons and the electron-ion interaction was described using ultra-soft pseudo potentials of the Vanderbilt form [41]. The exchange-correlation interaction was described using the PW91 functional [36]. These calculations were performed using the CASTEP program [42, 52].

Two different types of calculations were performed; single point energy calculations to determine the energies of particular molecular conformations and geometry optimizations to find relaxed molecular conformations. Both of these calculations are outlined more fully in §2.6. Single point energy calculations are taken to be converged once the change in energy drops below 10^{-5} eV per atom. For a geometry optimization an initial structure is constructed using the Cerius^2 modelling package [166]. The structure is taken to be converged when the residual forces have fallen below 0.05 eV Å^{-1}, the RMS displacement of the atoms is below 0.001 Å and the change in energy is less than 10^{-5} eV per atom. Potential energy curves for bond stretches and bond angle bends were found from a series of single point energy calculations. To determine the torsional potentials it necessary to hold a particular dihedral fixed while allowing the rest of the structure to relax. For a dihedral consisting of atoms *i*-*j*-*k*-*l*, atom i has to be restricted to move only in the plane containing i, j, and k, so the force becomes

$$\mathbf{F}_i^c = \mathbf{F}_i - (\mathbf{F}_i.\hat{\mathbf{n}}_{ijk})\hat{\mathbf{n}}_{ijk} \tag{4.26}$$

where $\hat{\mathbf{n}}_{ijk}$ is the unit normal to the i-j-k plane. Similarly the force on l becomes

$$\mathbf{F}_l^c = \mathbf{F}_l - (\mathbf{F}_l.\hat{\mathbf{n}}_{jkl})\hat{\mathbf{n}}_{jkl}. \tag{4.27}$$

Atoms j and k are constrained to the intersection of the ijk plane and the jkl plane, i.e. the j-k bond. Thus the forces on j and k become

$$\mathbf{F}_j^c = (\mathbf{F}_j.\hat{\mathbf{n}}_{jk})\hat{\mathbf{n}}_{jk} \tag{4.28}$$

$$\mathbf{F}_k^c = (\mathbf{F}_k.\hat{\mathbf{n}}_{kj})\hat{\mathbf{n}}_{kj}, \tag{4.29}$$

where $\hat{\mathbf{n}}_{jk}$ is the unit vector along the j-k bond.

4.6.3 Fitting Force Field Parameters

Once potentials for bond stretches, bond angles bends, and torsional rotations are known it is then necessary to obtain the force field parameters from them. For stretching and bending parameters this is a simple task of fitting a second order polynomial to the *ab initio* potential energy curve. The parameters in (4.17) and (4.18) are then found from the coefficients of the fitted polynomials. The force field parameters can also be found from the forces on the atoms. Using

$$\mathbf{F}(\mathbf{r}) = -\nabla_{\mathbf{r}} E(\mathbf{r}) \tag{4.30}$$

on (4.17) gives

$$F = -k_{ij}(r_{ij} - r_{ij0}). \tag{4.31}$$

Fitting torsional parameters is more complicated due to the additional influence of non-bonded interactions. The procedure used to fit the torsional parameters is as follows:

1. make initial guess for V_{ijkln}
2. minimize energy of molecule in the force field for a set of values of the dihedral angle ϕ (with ϕ held fixed)

3. calculate the sum of squared differences between the *ab initio* data and the data obtained from the energy minimization

$$\chi^2(\{V_{ijkln}\}) = \sum_a |E^{ab}(\phi_a) - E^{ff}(\phi_a)|^2 \tag{4.32}$$

4. find the set of $\{V_{ijkln}\}$ that minimizes χ^2.

This requires many energy minimizations to obtain converged values of $\{V_{ijkln}\}$; however it does ensure that all the other force field contributions to the torsional potential are properly accounted for during the fit. All the minimizations are performed using Powell's method [47].

4.6.4 Validation of Force Field Parameters

As the force field is intended for use in liquid phase simulations, the validation process should test that it is capable of reproducing liquid phase properties. Thus while molecular structures and vibrational frequencies provide a useful test of a force field, it is more useful for our force field to reproduce thermodynamic properties. Two such properties are the density and heat of vapourisation. The density ρ is trivially found from the volume of the simulation cell V.

The heat of vapourisation is found from

$$\Delta_{vap}H = H(g) - H(l), \tag{4.33}$$

where H is the enthalpy l and g denote the liquid and gas phase. Using $H = E_{inter} + E_{intra} + PV$ where E_{inter} and E_{intra} are the intermolecular and intramolecular energies, P is the pressure and V is the volume. In the gas phase, $PV = Nk_BT$, while $E_{inter} = 0$ and in the liquid PV is negligible. Thus [153]

$$\Delta_{vap}H = E_{intra}(g) - (E_{intra}(l) + E_{inter}(l)) + Nk_BT. \tag{4.34}$$

As well as these thermodynamics properties the simulation data can also be used to calculate diffusion coefficients, radial distribution functions, and dihedral angle distributions.

Condensed phase properties are calculated from molecular dynamics simulations of the pure liquids. These were performed on a system consisting of 216 molecules. The simulations were performed using the DL_POLY package [167]. The equations of motion were solved using the leapfrog algorithm with a time-step of 2 fs. Temperature and pressure were controlled using the Nosé-Hoover thermostat and Hoover barostat [122–124] with relaxation times of 1 ps and 4 ps respectively. The long range electrostatic interactions were handled using an Ewald sum [115] with a convergence parameter of 0.48 $Å^{-1}$ and 6 wave-vectors in the x, y, and z directions. A cut-off of 9 Å was applied to the Van der Waals interaction. Bond lengths were constrained using the SHAKE algorithm [117]. The starting configuration for each simulation was a simple cubic lattice at a gas phase density. These were then compressed under a large pressure until a liquid state density (500-1000 kg m^{-3}) was obtained.

Calculation of $\Delta_{vap}H$ requires the gas phase energy. However molecular dynamics performs poorly in the gas phase [125]. With few collisions between molecules, MD simulations often get trapped in particular conformations leading to poor sampling of conformation space. Consequently, the gas phase energy was calculated using Monte Carlo calculations on single molecules.

4.7 Force Field Parameters

Force field parameters were calculated for a group of molecules that contain functional groups commonly found in mesogenic molecules. These were biphenyl, 4-cyanobiphenyl, 2,3,and 4-fluorobiphenyl, phenylcyclohexane, propylbenzene, and butane.

4.7.1 Atom Types

The basis of a force field is the selection of suitable atom types. These are atoms similar enough in the physical and chemical sense for them to be the same in different molecules, allowing them to be treated as identical in a molecular mechanics calculation. Our selection of atom types are based on the AMBER force field [143] and are shown in Tab. 4.1.

Atom type	Description	Mass /amu
CA	Aromatic carbon	12.01
CP	Aromatic carbon (joining aromatic rings)	12.01
HA	Aromatic hydrogen	1.008
CZ	Carbon in cyano group	12.01
NZ	Nitrogen in cyano group	14.01
Cn*	Aliphatic carbon	12.01
HC	Aliphatic hydrogen	1.008
F	Fluorine	19.00

Table 4.1: Atom types. * n indicates number of attached hydrogen atoms.

4.7.2 Electrostatic and Van der Waals Parameters

Van der Waals parameters are the hardest to calculate from *ab initio* calculations. A high level of theory (at least MP2) is needed to account for electron correlation that gives rise to the dispersion interaction. DFT calculations, such as those employed here, perform particularly poorly in this regard. In any case Van der Waals parameters calculated from *ab initio* calculations in the gas phase tend to perform poorly in condensed phase simulations [168, 169]. This is due to the neglect of many-body effects such as induction or polarization. The van der Waals parameters have thus been taken from the OPLS parameter set [153, 154, 170], which has been derived

to accurately reproduce thermodynamic quantities of small organic molecules. As these have been derived from condensed phase simulations they implicitly include many-body effects that are not included in van der Waals parameters calculated from gas-phase calculations. The atomic charges were also taken from the OPLS parameter set apart from the charges for aromatic carbon and hydrogen atoms. These charges were found by fitting to the quadrupole moment for benzene, obtained from density functional theory calculations. A better representation of the quadrupole moment was found by increasing the OPLS partial charges from ∓ 0.115 to ∓ 0.122. This is shown in Tab. 4.2. The full list of non-bonded parameters is shown in Tab. 4.3.

Method	$q_{CA/HA}$ / e	Q_{xx} / eV Å^2	Q_{yy} / eV Å^2	Q_{zz} / eV Å^2
PW-DFT (GGA)	-	0.79	0.80	-1.59
OPLS	∓ 0.115	0.67	0.68	-1.35
Here	∓ 0.122	0.72	0.72	-1.44

Table 4.2: Calculated quadrupole moment of benzene.

4.7.3 Bond Stretching Parameters

Shown in Fig. 4.6 are the energy and force plotted against change in bond length for CA-HA and CZ-NZ bonds. As can be seen the energy shows a quadratic dependence on δr as expected from (4.17) while the force varies linearly with δr. The bond stretching parameters are shown in Tab. 4.4. Tab. 4.5 provides a comparison of our bond stretching force constants for the aliphatic C-C and C-H bond stretches compared with those from the OPLS [154], MM3 [142], MMFF94 [163],and AMBER [143] force fields. Our values show reasonable agreement, notably with the OPLS, which employs the same harmonic form, and the MMFF94 values. This is indicative of the quality of our *ab initio* calculations; we obtain comparable results from the

Atom Type	ϵ_i / kJ mol^{-1}	σ_i / Å	q_i / e
CA	0.293	3.550	-0.122
CA[1]	0.293	3.550	0.035
CA[2]	0.293	3.550	0.220
CP	0.293	3.550	0.000
Cn	0.276	3.500	-0.060n[3]
CZ	0.628	3.650	0.395
HA	0.126	2.420	0.122
HC	0.126	2.500	0.060
NZ	0.711	3.200	-0.430
F	0.255	2.850	-0.220

Table 4.3: Van der Waals parameters and partial charges. Notes: (1) CA bonded to CZ, (2) CA bonded to F, (3) n = number of attached hydrogens.

density functional calculations as those from high level (MP2) quantum chemical calculations.

4.7.4 Bond Angle Bending Parameters

Shown in Fig. 4.7 are the bond angle bending potentials for the CA-CA-HA and the CA-CA-F bond angles. These clearly show a quadratic dependence on the change in angle, in agreement with (4.18). Force field parameters for bond angle bending are shown in Tab. 4.6

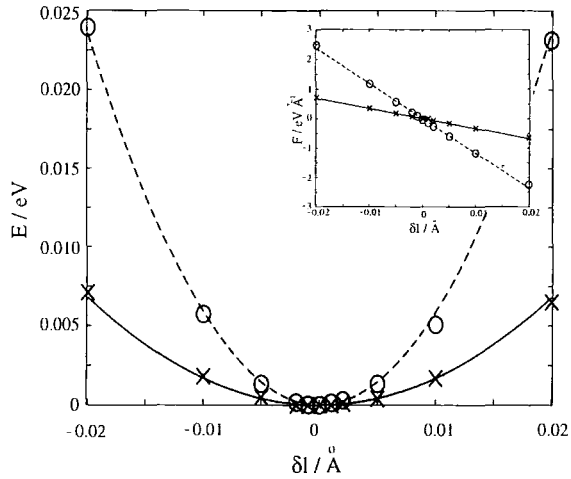

Figure 4.6: Bond stretching potentials for CA-HA bond and the CZ-NZ bond. For the CA-HA bond the *ab initio* potential is marked by crosses and the fitted potential shown by the solid line. For the CZ-NZ bond the *ab initio* potential is marked by circles and the fitted potential marked by the dashed line. The inset shows the variation of force with distance (same symbols).

Bond	k_{ij} / eV Å^{-2}	r_{ij0} / Å
CA-HA	33.96	1.08
CA-CA	44.32	1.38
CA-CP	44.32	1.38
CP-CP	27.28	1.47
CA-CZ	31.52	1.31
CZ-NZ	115.11	1.17
CA-Cn	24.47	1.50
Cn-Cn	22.97	1.51
Cn-HC	31.65	1.09
CA-F	35.08	1.36

Table 4.4: The bond stretching force constants (k_{ij}) and equilibrium bond lengths (r_{ij0}) are given here for a range of bonds found in liquid crystal fragments.

Force field	Cn-Cn bond	Cn-HC bond	Ref.
	k_{ij} (eV Å^{-2})	k_{ij} (eV Å^{-2})	
This work	22.97	31.65	-
OPLS	23.22	29.40	[154]
MM3	28.03	29.59	[142]
MMFF94	23.72	32.15	[163]
AMBER	26.90	28.71	[154]

Table 4.5: Comparison of bond stretching force constants for aliphatic C-C and C-H bonds, from this work and other force fields

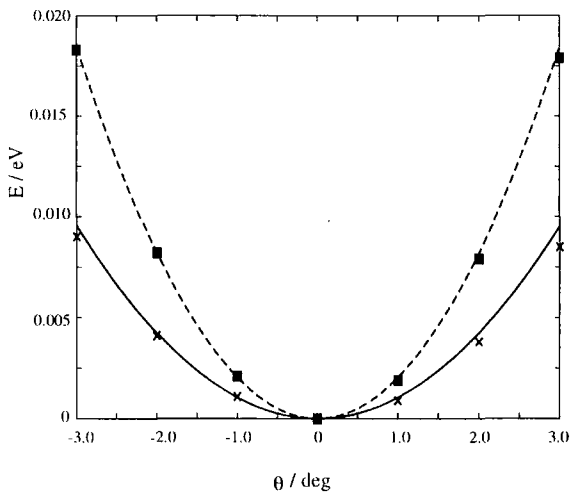

Figure 4.7: Bond angle bending potentials for CA-CA-HA angle (*ab initio* data marked by crosses and fitted potential shown by the solid line) and CA-CA-F (*ab initio* data marked by squares and fitted potential shown by the dashed line).

Angle	k_θ / $\times 10^{-5}$ eV $^{\circ -2}$	θ_{eq} / $^{\circ}$
CA-CA-HA	98.46	120
CA-CA-CA	84.94	120
CA-CP-CP	95.32	120
CA-CA-CZ	134.38	120
CA-CZ-NZ	71.10	180
Cn-Cn-Cn	244.76	113
Cn-Cn-HC	116.98	112
HC-Cn-HC	147.25	107
CA-CA-F	101.90	120

Table 4.6: Bond angle bending force constants (k_θ) and equilibrium bond angles θ_{eq}.

4.7.5 Torsional Rotation Parameters

The torsional potential and hence the torsional force constants are the key intramolecular parameters responsible for determining the overall shape of a molecule. Thus they have a large bearing on the behaviour of the molecules. Unlike bond stretching and bending parameters they are less transferable: they are more sensitive to the molecular environment than the other intra-molecular terms [171].

4.7.5.1 Biphenyl and 4-cyanobiphenyl

Biphenyl and 4-cyanobiphenyl (Fig. 4.8) are important core units for mesogenic molecules. The torsional potentials for biphenyl and 4-cyanobiphenyl are shown in Fig. 4.9. As can be seen there is good agreement between the *ab initio* and fitted potentials.

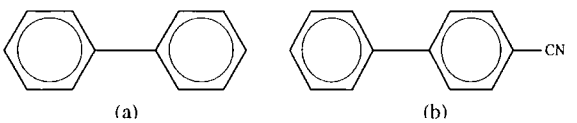

Figure 4.8: Structures of (a) biphenyl and (b) 4-cyanobiphenyl.

The torsional barrier of biphenyl has been the subject of a number of previous studies, both theoretical [146, 172–175] and experimental [176–179]. As can be seen from Fig. 4.9 we have been able to reproduce the *ab initio* torsional potentials accurately through the fitted potentials. The rotational barrier at 0° for biphenyl is found to be 0.089 eV for the fitted potential and 0.087 eV from the *ab initio* data. The rotational barrier at 90° is 0.108 eV from the fitted potential and 0.108 eV from the *ab initio* data. A previous study using DFT with the 6-31G(d) basis set [173] found the energy barriers to be 0.087 and 0.104 eV. However the present results benefit from a more complete basis set than these earlier results. The barrier heights have been calculated using a number of wavefunction based methods [172,174], which give barrier heights of about 0.098 to 0.141 eV for the 0° barrier and 0.063 to 0.092 eV

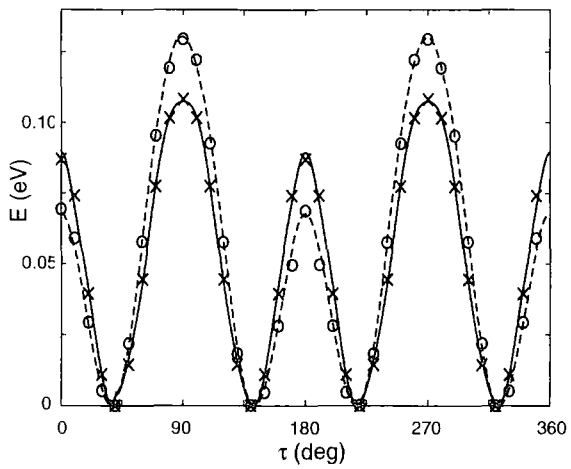

Figure 4.9: Torsional potentials for biphenyl and 4-cyanobiphenyl. For biphenyl, the *ab initio* data is marked with crosses and the fitted potential is shown in bold. For 4-cyanobiphenyl, the *ab initio* data is marked by circles, and the fitted potential is shown by the dashed line.

for the 90° barrier. Again these values have been obtained using a smaller basis set than in this work. Experimentally E_0 has been found to be between 0.061 and 0.079 eV and E_{90} between 0.061 and 0.226 eV. These results are summarized in Tab. 4.7, along with results from the MM4 force field [146]. Our 0° barrier is lower than that given by the wavefunction methods, but is consistent with other DFT calculations and also with experiment. The 90° barrier is somewhat larger than those calculated by wavefunction methods as well as the electron diffraction and Raman scattering results, although it is substantially lower than that given by NMR measurements. The NMR measurements however were performed on biphenyl in a liquid crystalline solvent while the other experimental and computational results are for molecules in the gas phase. In agreement with experimental measurements, we have $E_{90} > E_0$.

For 4-cyanobiphenyl the barrier heights at 0° and 90° are 0.073 eV and 0.130 eV respectively from the fitted potential and 0.069 eV and 0.130 eV from the *ab initio* data. Previous *ab initio* calculations at the HF/6-31G level found the barriers to be 0.212 eV and 0.067 eV [86]. The 0° and 90° barrier heights have been determined

Method	Ref.	ΔE_0	ΔE_{90}
PW-DFT (GGA)	-	0.087	0.108
Fitted potential	-	0.089	0.108
MM4	[146]	0.107	0.080
HF/6-31G*//MP2/6-31G*	[172]	0.141	0.063
MP2/cc-PVQZ//MP2/6-31G*	[172]	0.098	0.092
MP2/6-31G(d)	[173]	0.169	0.091
B3-LYP/6-31G(d)	[173]	0.087	0.104
B3LYP/cc-pVTZ	[174]	0.083	0.092
B3LYP/6-311G*	[175]	0.094	0.078
Electron diffraction	[177, 178]	0.061	0.069
Raman scattering	[176]	0.061	0.061
NMR	[179]	0.079	0.226

Table 4.7: Comparison of rotational barrier heights for biphenyl between this work and previous studies (barrier heights in eV).

by NMR [180] to be 0.079 and 0.241 eV respectively. Again the NMR results are for cyanobiphenyl dissolved in a liquid crystal solvent. In agreement with experiment and in contrast to the Hartree-Fock results we have $E_0 < E_{90}$ which underlines the greater accuracy of our method compared to earlier calculations.

From Fig. 4.9 it can be seen that there is a marked difference in torsional potentials between biphenyl and 4-cyanobiphenyl. This would not be expected from the classical non-bonded energy, shown in Fig. 4.10, which is identical for both molecules. The change in torsional potential is caused by charge transfer toward the terminal cyano group. This changes the charge distribution and hence the trade off between the repulsion between the hydrogen atoms and conjugation that governs the torsional potential. The torsional potential and force constants are not transferable between biphenyl and 4-cyanobiphenyl [171].

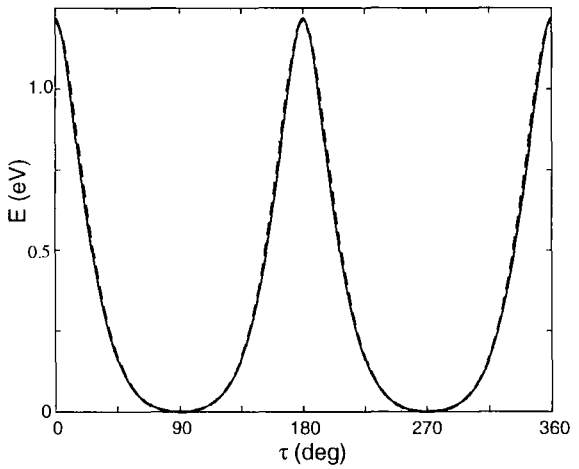

Figure 4.10: Non-bonded energy as a function of torsional angle for biphenyl (solid) and 4-cyanobiphenyl (dashed).

4.7.5.2 Fluorinated Biphenyls

Lateral polar substiutents are often added to mesogenic molecules to produce a negative dielectric anisotropy. However, the decrease in the length to width ratio caused by these substituents causes a decrease in the clearing temperature and

the mesophase stability. They also have a large effect on the torsional potentials of conjugated systems. In addition to changing the conjugation of the system, they also create highly dipolar regions which give rise to strong electrostatic interactions. For liquid crystal molecules, the most common lateral substituent is fluorine, because it has the smallest effect on the phase stability due to its small size. We have calculated the torsional potential for the various fluorinated biphenyls with structures shown in Fig. 4.11.

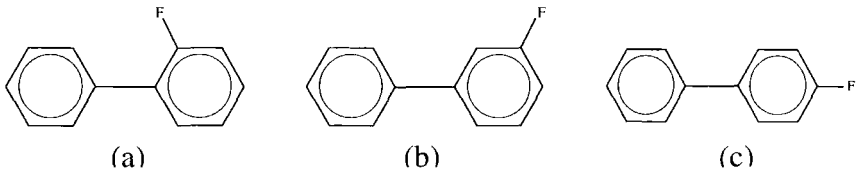

Figure 4.11: Structures of (a) 2-fluorobiphenyl, (b) 3-fluorobiphenyl, and (c) 4-fluorobiphenyl.

The torsional potentials for the fluorobiphenyls are shown in Fig. 4.12. The effect of moving the fluorine atom from the 2 position to the 3 and 4 positions can be clearly seen. Moving the fluorine atom from the 2 position to the 3 position results in a large change to the torsional potential with the barrier at 90° becoming lower than the 180° (planar) barrier. The decrease in the planar barrier height is expected as there is no longer a close approach between the fluorine atom and a hydrogen atom on the other phenyl ring. The difference between the potentials for the fluorine in the 3 and 4 positions is smaller. In all three cases there is good agreement between the *ab initio* potentials and the fitted potentials. There is little previous work on these torsional potentials, either experimental or theoretical. The torsional potential of 2-fluorobiphenyl has been the subject of a few previous computational studies [175, 181, 182]. The most recent work was an DFT investigation using the B3LYP functional [175]. Barrier heights of 0.132 eV (0°) and 0.052 (90°) were found; in reasonable in agreement with our values of 0.080 eV and 0.081 eV from the *ab initio* and fitted potentials respectively for the 0° barrier and 0.119 eV and 0.121

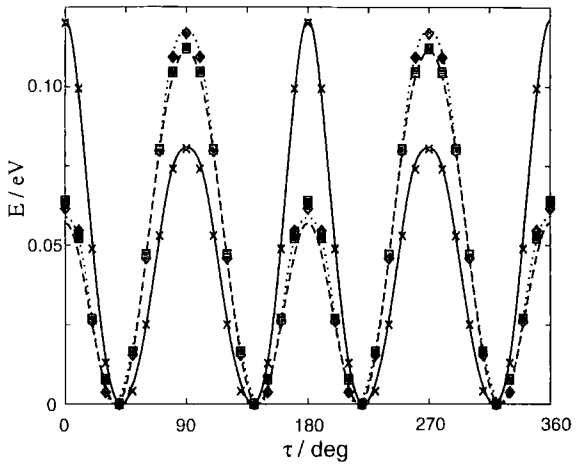

Figure 4.12: Torsional potentials for 2-fluorobiphenyl, 3-fluorobiphenyl, and 4-fluorobiphenyl. For 2-fluorobiphenyl the *ab initio* potential is marked by crosses and the fitted potential is shown by the bold line, for 3-fluorobiphenyl the *ab initio* potential is marked by squares and the fitted potential is shown by the dashed line, and for 4-fluorobiphenyl the *ab initio* potential is marked by diamonds and the fitted potential is shown by the dotted line.

eV for the 90° barrier. The torsional potential of 4-fluorobiphenyl was previously investigated by electron scattering [183]. The barrier heights were found to be 0.112 eV at 0° and 0.116° at 90°. The 90° is in good agreement with both the *ab initio* barrier of 0.117 eV and the fitted barrier of 0.118 eV. The values for the 0° barrier are very different however.

4.7.5.3 Phenylcyclohexane

Another common liquid crystal core component is the partially conjugated phenylcyclohexane (Fig. 4.13). Here the saturated cyclohexane ring prevents electron delocalization over all of the molecule. Thus the torsional potential is governed by repulsion between the hydrogens. A previous study has shown that the addition of a polar end group has little effect on the torsional potential [171]. Both the *ab initio* and fitted potentials for phenylcyclohexane are shown in Fig. 4.14. The fitted

potential closely matches the *ab initio*, with a barrier height of 0.120 eV in the *ab initio* potential and 0.116 eV in the fitted potential. These are in good agreement with the experimental value of 0.124 eV [184] found by NMR spectroscopy in the liquid phase.

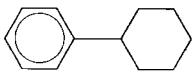

Figure 4.13: Structure of phenylcyclohexane.

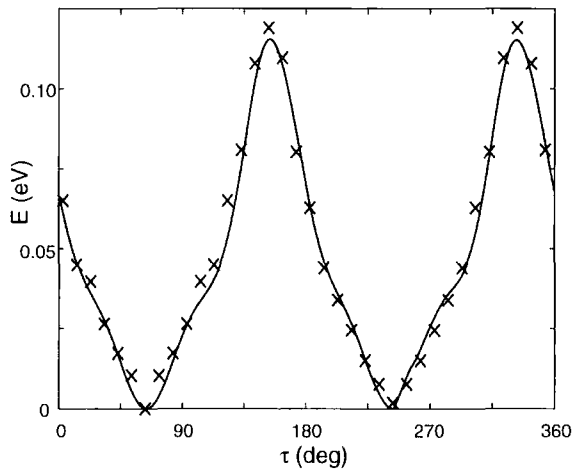

Figure 4.14: Torsional potential for phenylcyclohexane. *Ab initio* potential is marked by crosses and the fitted potential is shown by the solid line.

4.7.5.4 Propylbenzene

The coupling between rotations of the tail and the core in a liquid crystal molecule can play an important role in determining the shape and behaviour of the molecule. Torsional parameters for these structural features have been found from studying the propylbenzene molecule Fig. 4.15. There are two different torsional potentials; the CA-CA-C2-C2 torsion and the CA-C2-C2-C3 torsion. Both of these are shown in Fig. 4.16.

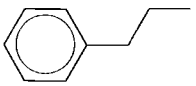

Figure 4.15: Structure of propylbenzene.

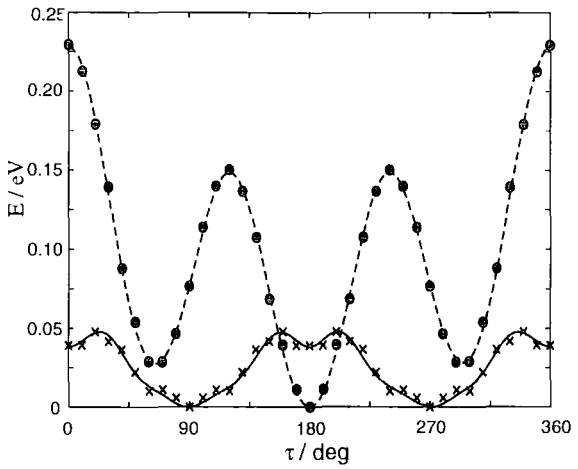

Figure 4.16: Torsional potentials for propylbenzene. The *ab initio* potentials are marked by crosses, for the CA-CA-C2-C2 dihedral, and circles, for the CA-C2-C2-C3 dihedral. The fitted potentials are shown by the bold line, for the CA-CA-C2-C2 dihedral, and dashed line for the CA-C2-C2-C3 dihedral.

As can be seen the CA-C2-C2-C3 has a global minima (*trans*) at 180° and two local minima (*gauche*) as expected for an alkyl chain. The CA-CA-C2-C2 torsion is periodic over 180°, as expected from the 2-fold symmetry of the molecule, with minima at 90° and 270°. There are also local minima at 0° and 180°. This configuration minimizes the repulsion between the hydrogen atoms on the phenyl ring and the first hydrogen atom on the tail [171].

4.7.5.5 Butane

As the simplest alkane with a C-C-C-C torsion butane (Fig. 4.17) has been well studied both experimentally and theoretically. Shown in Fig. 4.18 are the *ab initio* and fitted torsional potentials. Again good agreement can be seen between the *ab*

initio data and the fitted potential. The eclipse(0°) barrier height is 0.251 eV and the *trans-gauche* barrier is 0.140 eV. This system has been well studied, both experimentally [185–188] and theoretically [189,190]. A study by Suzuki *et al* [189] compared the rotational barriers of butane calculated by various computational methods, finding *trans-gauche* barriers between 0.142 and 0.159 eV and eclipse barriers between 0.245 and 0.268 eV, to which our results compare favourably. Our values for the *trans-gauche* energy difference (*ab initio* potential 0.034 eV, fitted potential 0.035 eV) are in better agreement with experimental values than those calculated up to the MP2 level and with DFT using a localized basis set. These results are displayed fully in Table 4.8.

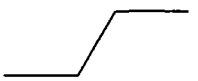

Figure 4.17: Structure of butane.

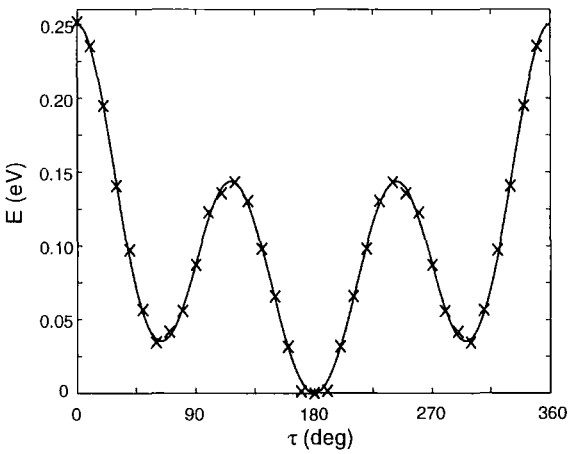

Figure 4.18: Torsional potential for butane.

Method	Ref	ΔE_{t-g}	$E_{120°}$	$E_{0°}$
PW-DFT(GGA)	this work	0.035	0.142	0.251
Fitted potential	this work	0.034	0.140	0.251
CCSD(T)/TZ($2d, 2p$)	[190]	0.026	0.142	0.241
RMP2/QD($2d1f, 2p1d$)	[190]	0.027	0.142	0.247
HF/6-31G*//HF/6-31G*	[189]	0.041	0.159	0.268
MP2/6-31G*//MP2/6-31G*	[189]	0.029	0.157	0.263
MP4(SDTQ)/6-31G*//MP2/6-31G*	[189]	0.031	0.154	0.257
QCISD(T)/6-31G*//MP2/6-31G*	[189]	0.031	0.152	0.255
BLYP/6-31G*//BLYP/6-31G*	[189]	0.037	0.150	0.245
MM4	[146]	0.029	0.147	0.214
Raman scattering	[186]	0.039	0.157	0.196
Thermodynamic	[185]	0.035	0.156	-
IR in solid Ne	[187]	0.032	-	-
Electron diffraction	[188]	0.033	-	-

Table 4.8: Comparison of rotational barrier energies for butane (in eV).

4.7.5.6 Torsional Force Constants

A complete set of torsional force constants have been obtained from the fitted curves. These are shown in Tab. 4.9.

Torsion	$k_{\tau 1}$	$k_{\tau 2}$	$k_{\tau 3}$	$k_{\tau 4}$	$k_{\tau 5}$	$k_{\tau 6}$	$k_{\tau 8}$	$k_{\tau 10}$	$k_{\tau 12}$
CA-CP-CP-CA[1]	0.00	7.90	0.00	1.76	0.00	0.54	0.16	0.03	0.01
CA-CP-CP-CA[2]	0.00	9.57	0.00	0.11	0.00	0.19	0.25	0.07	-0.04
CA(F)-CP-CP-CA	0.00	4.87	0.00	-1.48	0.00	-0.07	0.00	-0.03	0.05
CA-CP-CP-CA[3]	0.00	3.97	0.00	0.95	0.00	0.31	0.08	0.01	0.01
CA-CP-CP-CA[4]	0.00	4.62	0.00	0.11	0.00	0.18	0.10	0.03	0.05
CA-CA-CA-CA	0.00	41.24	0.00	0.00	0.00	0.00	0.00	0.00	0.00
Cn-Cn-Cn-Cn	8.47	0.32	0.12	-1.63	0.17	0.06	0.00	0.00	0.00
HC-Cn-Cn-Cn	0.00	0.00	0.16	0.00	0.00	0.00	0.00	0.00	0.00
HC-Cn-Cn-HC	0.00	0.00	0.14	0.00	0.00	0.00	0.00	0.00	0.00
CA-CA-HA-CA	0.00	4.34	0.00	0.00	0.00	0.00	0.00	0.00	0.00
CA-Cn-Cn-Cn	3.04	0.03	-0.14	0.55	0.00	0.25	0.00	0.00	0.00
CA-CA-Cn-Cn[5]	0.00	3.59	0.00	-0.29	0.00	-0.21	0.08	0.00	0.00
CA-CA-Cn-Cn[6]	0.00	2.28	0.00	-1.00	0.00	-0.20	0.00	0.00	0.00

Table 4.9: Torsional force constants in $\times 10^{-4}$ eV. Notes: (1)- biphenyl, (2) 4-cyanobiphenyl, (3) 3-fluorobiphenyl, (4) 4-fluorobiphenyl, (5) propylbenzene, and (6) phenylcyclohexane.

4.8 Validation of Force Field Parameters

The force field has been tested by computing thermodynamic quantities of the pure liquids as outlined in §4.6.4. Simulations to calculate these quantities were performed on molecules used in the parameterization of force field parameters. Densities and

heats of vapourisation were also calculated for the molecules hexane and terphenyl (Fig. 4.19) to test the transferability of the calculated parameters. The simulations were performed at atmospheric pressure.

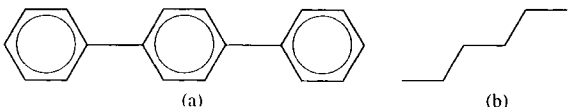

Figure 4.19: Structures of (a) terphenyl and (b) hexane.

4.8.1 Density

The calculated system densities for each of the sample liquids are shown in Tab. 4.10, along with the experimental values (where known). As can be seen from the table the calculated densities are in good agreement with the experimental values [153, 191, 192], with an average error of 1.2%. The density is largely determined by the non-bonded parameters and the OPLS values we have taken for these have been shown to reproduce experimental densities with an average error of about 2% [168]. For molecules containing flexible chains the torsional parameters also have an effect on the density. The average error for molecules with flexible chains (butane, hexane, and propylbenzene) is about 0.7 %.

4.8.2 Heats of Vapourisation

The calculated values of $\Delta_{vap}H$, obtained using (4.34) are shown in Tab. 4.11 along with the known experimental values [192]. Again there is good agreement between the calculated values and experiment, with an average error of 3.3 %. The largest error is for terphenyl (5.1 %). This however is at a temperature of 493 K, over 100 K above the other simulations. At this temperature it may be expected that anharmonic effects become significant in both stretches and bond angle bends and that fixing bond lengths may no longer be appropriate.

Liquid	T / K	$\langle V \rangle$ (Å^{-3})	$\langle \rho \rangle$ /kg.m^{-3}	$\langle \rho \rangle$(expt) / kg.m^{-3}	error
biphenyl	343	56373	981.3±7.1	990[1]	1.0%
4-cyanobiphenyl	360	62485	1028.7±6.8		
butane	272.5	34685	605.3±10.6	602[2]	0.5%
n-propylbenzene	298	50388	861.8±7.8	860[3]	0.2%
phenylcyclohexane	298	60620	954.9	939[3]	1.7%
2-fluorobiphenyl	343	57303	1085.6		
hexane	298	46860	664.3±8.0	656[3]	1.3%
terphenyl	493	89217	932.4±8.8	957.7[3]	2.6%

Table 4.10: Computed and experimental densities of sample liquids. Notes: (1) Ref. [191], (2) Ref. [153], (3) Ref. [192].

4.8.3 Diffusion Coefficients

The centre of mass diffusion coefficients were calculated from the simulation data using the Einstein relation, (3.54). These are shown in Tab. 4.12. The diffusion coefficient of butane was calculated by Daivis and Evans [193] using non-equilibrium molecular dynamics to be 7.4×10^{-9} m^{2}s^{-1}. This was at a lower density than our results (583 kg m^{-3}) a factor that strongly influences diffusion.

4.8.4 Dihedral Angle Distribution Functions

The dihedral angle distributions for butane is shown in Fig. 4.20. The C3-C2-CC2-C3 dihedral shows a large central peak, corresponding to the *trans* minima in the potential (as shown in Fig. 4.18 and two smaller peaks corresponding to the *gauche* minima). Integrating these gives a *trans* population of 67.5 % and *gauche* populations of 16.6 % and 15.9 %. This is in good agreement with a previous simulation study which reported a *trans* population of 67.8 % [194] and Raman scattering data that gave a *trans* population of 70.7 % [186]. The agreement between

Liquid	T / K	E_{total}(l)	E_{intra}(g)	Δ_{vap}H	Δ_{vap}H(expt)	Error
biphenyl	343	-9.669	50.472	62.99	61.23	2.9%
4-cyanobiphenyl	360	-34.024	43.095	77.119		
butane	272.5	17.03	36.43	21.67	22.44	3.4%
n-propylbenzene	298	28.46	71.86	45.88	46.48	1.3%
phenylcyclohexane	298	19.84	83.77	66.41	64.14	3.5%
2-fluorobiphenyl	343	62.74	112.82	31.66		
hexane	298	7.56	38.22	33.13	31.98	3.6%
terphenyl	493	190.98	123.06	72.02	75.89	5.1%

Table 4.11: Computed and experimental heats of vapourisation for sample liquids. All energies in kJ mol^{-1}. $E_{total}(l) = E_{inter}(l) + E_{intra}(l)$. Experimental results taken from [192].

the two *gauche* populations is good, showing only a small asymmetry. The C2-C2-C3-HC dihederal shows the expected three-fold symmetric distribution. Integrating this distribution gives the proportion under each peak to be 32.5 %, 33.8 %, and 33.7 %.

Figure 4.21 shows the dihedral angle distributions for liquid hexane and butane. As can be seen from part (a) the distributions for hexane are the same for as for butane with a large central peak and two smaller peaks. The central dihedral (τ_2) has a larger *trans* population than the outer two dihedrals, consistent with previous simulations [195]. Part (b) shows that the *trans* populations are higher in liquid hexane than in liquid butane.

Shown in Fig. 4.22 are the liquid phase dihedral angle distributions for biphenyl and 4-cyanobiphenyl. As can be seen, maxima in these occur at the minima in both the *ab initio* and fitted potentials (as shown in Fig. 4.9).

Liquid	T / K	D / $\times 10^{-9}$ $m^2 s^{-1}$
biphenyl	343	0.718
4-cyanobiphenyl	360	0.555
butane	272.5	4.741
n-propylbenzene	298	1.006
phenylcyclohexane	298	0.205
2-fluorobiphenyl	343	0.634
hexane	298	3.152
terphenyl	493	1.939

Table 4.12: Diffusion coefficients calculated from molecular dynamics simulation data.

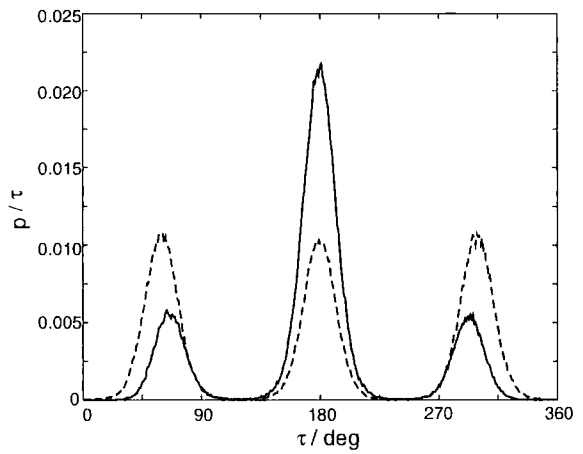

Figure 4.20: Dihedral angle distributions for butane. Solid line shows the C3-C2-C2-C3 dihedral angle distribution and the dashed line shows the C2-C2-C3-HC dihedral angle distribution.

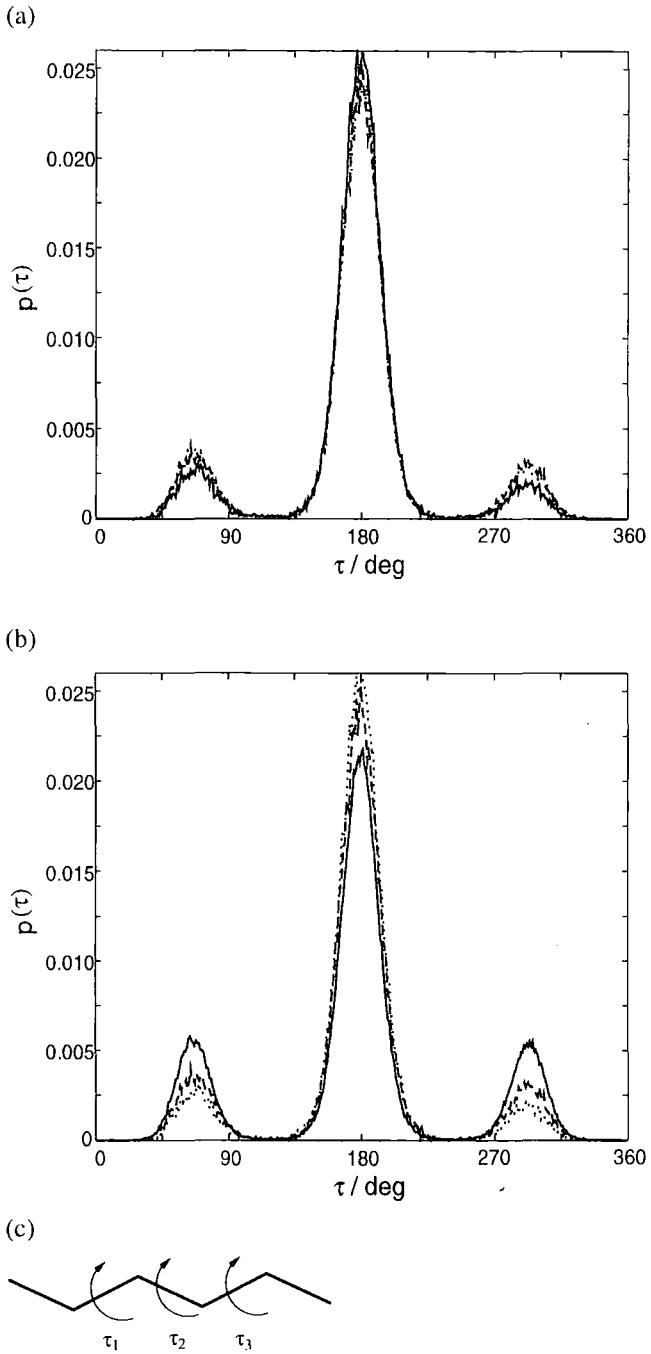

Figure 4.21: (a) Liquid phase dihedral angle distributions for hexane at 298 K, τ_1 (dotted line), τ_2 (solid line), and τ_3 (dashed line). (b) Dihedral angle distributions for liquid butane (solid line) at 272.5 K and liquid hexane at 298 K (dotted line for τ_1 and dashed line for τ_2). (c) definitions of τ_1, τ_2, and τ_3.

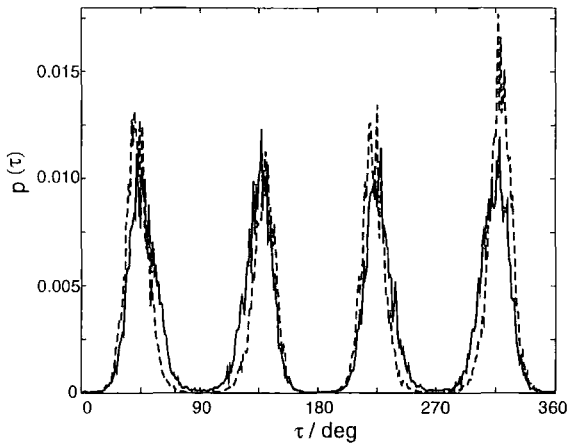

Figure 4.22: Liquid phase dihedral angle distribution functions for liquid biphenyl at 343 K (solid line) and liquid 4-cyanobiphenyl (dashed line) at 360 K.

4.8.5 Radial Distribution Functions

Shown in Fig. 4.23 are the centre of mass radial distribution functions for butane at 272.5 K and hexane at 298 K. For butane, $g(r)$ is typical of a fluid with the first solvation peak at approximately 5.4 Å. For hexane $g(r)$ shows a broad first peak starting at about 5.3 Å and peaking at about 6.9 Å.

The centre of mass radial distribution functions for biphenyl, 4-cyanobiphenyl, and 2-fluorobiphenyl are shown in Fig. 4.24. Both biphenyl and 2-fluorobiphenyl show first solvation peaks starting at about 4 Å, peaking at about 7.5 Å. For 4-cyanobiphenyl the onset of the first peak is about 3.5 Å with a maximum at about 5 Å. The similarity in the RDF for biphenyl and 2-fluorobiphenyl is to be expected due to the similarity in their molecular structures. The first peak in the RDF for 4-cyanobiphenyl is closer than in the other biphenyls due to the closer molecular packing caused by the strong dipole-dipole interactions between the molecules. Schematically this is shown in Fig. 4.25. The results of other simulations [93, 103] and experiments [196, 197] suggest the presence of parallel and antiparallel dimers in cyanobiphenyl systems.

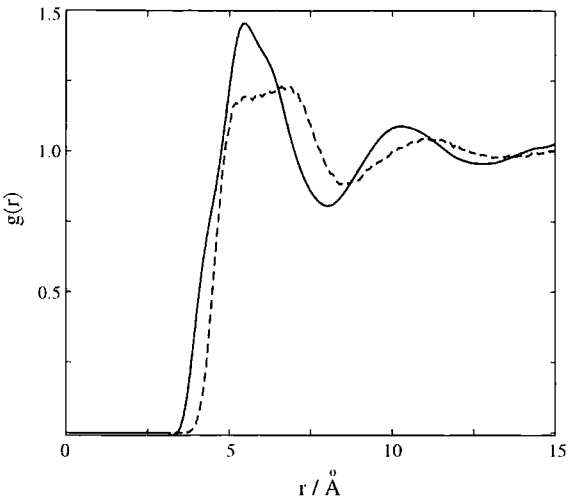

Figure 4.23: Radial distribution functions for butane at 272.5 K (solid line) and hexane at 298 K (dashed line).

4.9 Conclusions

Accurate representation of intra and intermolecular interactions is vital for good quality atomistic simulations. This is especially true for torsional energy profiles. However, previous studies [148] have shown that commercial force fields are not always reliable in this regard.

The work presented here describes the preliminary steps in the construction and validation of a force field for liquid crystal molecules. It also presents a methodology for the generation of force field parameters. Due to the large number of different functional groups that are found in mesogenic molecules any parameterization is liable to be incomplete, thus it is important to be able to generate force field parameters in a simple manner. This has been accomplished through the use of a simple functional form and the use of accurate, but relatively computationally inexpensive, *ab initio* density functional theory calculations.

The initial parameterization covers some of the common structural motifs in calamitic liquid crystals that are often used in display applications. In particular potential functions were found for alkyl chains, biphenyl and phenylcyclohexane

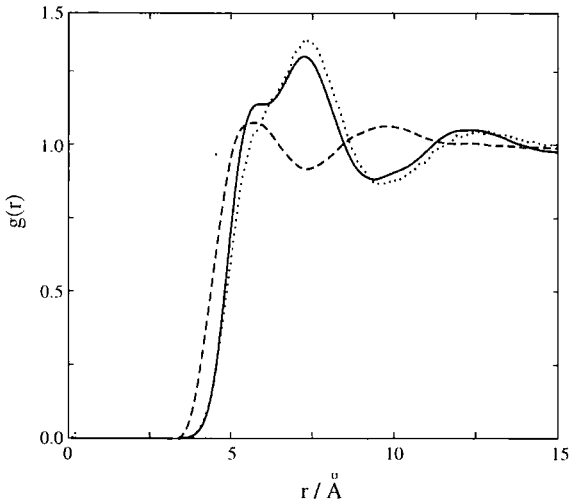

Figure 4.24: Radial distribution functions for biphenyl at 343 K (solid line), 4-cyanobiphenyl at 360 K (dashed line), and 2-fluorobiphenyl at 343 K (dotted line).

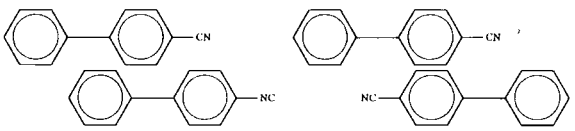

Figure 4.25: Examples of dimers in cyanobiphenyl systems.

cores, lateral and terminal fluorine substituents and cyano groups. The force field parameters were tested using condensed phase molecular dynamics simulations on some compounds containing these functional groups. Good agreement was found between calculated values of thermodynamic properties and experimental data.

Chapter 5

Calculation of the Rotational Viscosity Coefficient of a Nematic Liquid Crystal

5.1 Introduction

As liquid crystals are anisotropic fluids it is obvious that many of their properties are much more complicated than those of simple fluids. For instance the values of transport coefficients often depend on the direction (relative to the director). In a nematic the diffusion and heat transport are more rapid parallel to the director than perpendicular to it.

The hydrodynamics of liquid crystals are largely explained by Ericksen-Leslie (EL) theory [198–201], more recently renamed Ericksen-Leslie-Parodi (ELP) theory. Using this the viscosity coefficients can be calculated from correlation functions of the stress tensor σ_{ij} and the director $\mathbf{n}$. The viscous part of the stress tensor can be written as [202]

$$\sigma_{ij} = \alpha_1 n_i n_j V_{kp} n_k n_p + \alpha_2 n_j N_i + \alpha_3 n_i N_j + \alpha_4 V_{ij} + \alpha_5 n_j V_{ik} n_k + \alpha_6 n_i V_{jk} n_k \quad (5.1)$$

where n_i are the components of the director $\mathbf{n}$ and α_i are the Leslie coefficients. In (5.1) $\mathbf{V}$ is the symmetric part of the velocity gradient tensor

$$V_{ij} = \frac{1}{2}(\partial_j v_i + \partial_i v_j), \tag{5.2}$$

where $\partial_i v_j = \frac{\partial v_j}{\partial r_i}$, and $\mathbf{N}$ is the rotation of $\mathbf{n}$ relative to the fluid

$$N_i = \dot{n}_i - \frac{1}{2}(\partial_j v_i - \partial_i v_j) n_j, \tag{5.3}$$

where $\dot{\mathbf{n}} = \frac{\partial \mathbf{n}}{\partial t}$. In the EL theory, the Leslie coefficients are considered to be properties of the material and independent of the velocity gradient and time, but are functions of temperature and pressure. Knowledge of the Leslie coefficients is needed to calculate flow phenomena of liquid crystals. Four of these coefficients are linked by the Parodi equation [203]

$$\alpha_2 + \alpha_3 = \alpha_6 - \alpha_5. \tag{5.4}$$

In practice the Leslie coefficients give rise to rather complicated expressions for the viscosities. Thus it is common to use different but equivalent notation for the viscosity coefficients, such as those by Helfrich [204] or Miesowicz [205].

5.2 Viscosity in Liquid Crystals

5.2.1 Shear Viscosity

For a simple isotropic liquid the shear viscosity is defined in terms of the pressure tensor and the shear rate. For the simplest case, where the flow is along the x-axis and the velocity is a function of the y coordinate, i.e. $\mathbf{v} = v_x(y)\hat{\mathbf{x}}$, the shear viscosity coefficient η is determined by the ratio of the only non-vanishing component of the pressure tensor p_{yx} and the shear rate $\Gamma = \frac{\partial v_x}{\partial y}$

$$p_{yx} = -\eta \frac{\partial v_x}{\partial y} \tag{5.5}$$

As there are 3 different shear viscosity coefficients for a nematic liquid crystal the situation is more complicated. If we consider a nematic liquid crystal in the same geometry as above the director is a function of two angles θ and ϕ,

$$\mathbf{n} = (\sin\theta\cos\phi, \sin\theta\sin\phi, \cos\theta), \tag{5.6}$$

where θ and ϕ are shown in Fig. 5.1.

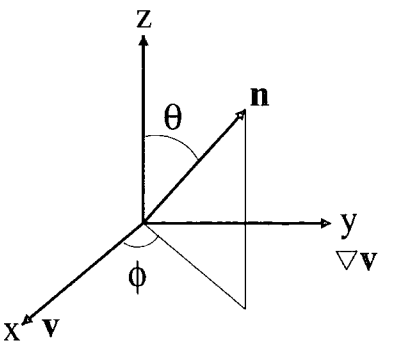

Figure 5.1: Definition of the angles θ and ϕ used to define the director relative to the flow velocity $\mathbf{v}$ and the velocity gradient $\nabla\mathbf{v}$.

The only non-vanishing elements of $\mathbf{V}$ (5.2) are

$$V_{xy} = V_{yx} = \frac{1}{2}v_{x,y} \tag{5.7}$$

and if the director is held fixed by an external field the rotation of the director given by (5.3) becomes

$$\mathbf{N} = \frac{1}{2}\left(-\sin\theta\sin\phi, \sin\theta\cos, \phi, 0\right)v_{x,y}. \tag{5.8}$$

If the liquid crystal is sheared in the xy-plane a constant velocity gradient parallel to the y axis ensues. From (5.1), (5.3), (5.6), and (5.7) we can calculate the xy component of the stress tensor. This then defines a viscosity

$$\begin{aligned}\eta(\theta,\phi) &= \frac{1}{2}(\alpha_4+\alpha_5-\alpha_2)\sin^2\theta\sin^2\phi + \frac{1}{2}(\alpha_4+\alpha_6+\alpha_3)\sin^2\theta\cos^2\phi + \\ &\quad \frac{1}{2}\alpha_4\cos^2\theta + \alpha_1\sin^4\theta\cos^2\phi\sin^2\phi,\end{aligned} \tag{5.9}$$

From (5.9) we can introduce a new set of viscosity coefficients η_1, η_2, η_3, and η_{12}. In terms of the Leslie coefficients these are

$$\begin{aligned} \eta_1 &= \frac{1}{2}(\alpha_4 + \alpha_5 - \alpha_2) \\ \eta_2 &= \frac{1}{2}(\alpha_4 + \alpha_6 + \alpha_3) \\ \eta_3 &= \frac{1}{2}\alpha_4 \\ \eta_{12} &= \alpha_1 \end{aligned} \tag{5.10}$$

Typically $\eta_1 > \eta_3 > \eta_2 > \eta_{12}$ [206]. η_1, η_2, and η_3 can be determined experimentally from shear flow experiments with specific director orientations

$$\begin{aligned} \eta_1 &: \mathbf{n}||\nabla\mathbf{v} \\ \eta_2 &: \mathbf{n}||\mathbf{v} \\ \eta_3 &: \mathbf{n} \perp \mathbf{v} \,\&\, \mathbf{n} \perp \nabla\mathbf{v}. \end{aligned}$$

These are shown schematically in Fig. 5.2. η_{12} needs to be taken into account when the director lies in the shear plane and is not parallel to either $\mathbf{v}$ or $\nabla\mathbf{v}$. Determination of η_{12} requires three experiments: two to find η_1 and η_2 and one where the influence of η_{12} on the shear viscosity is largest, with $\theta = 90°$ and $\phi = 45°$.

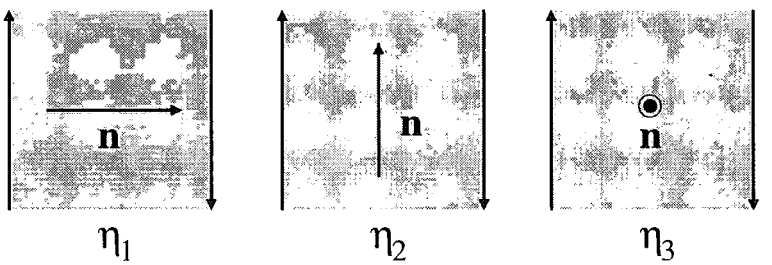

Figure 5.2: Definition of the shear viscosity coefficients η_1, η_2, and η_3. The arrows on the sides of the boxes show the shear flow.

5.2.2 Rotational Viscosity

In addition to the shear viscosities there is another viscosity coefficient, the rotational viscosity coefficient γ_1. This arises due to viscous torques being exerted on the director during rotation or during shear flow when the director orientation is held fixed. These torques can be found from the anti-symmetric part of the stress tensor, σ^a_{ij} [207]

$$\sigma^a_{ij} = \frac{\alpha_2 - \alpha_3}{2}(n_j N_i - n_i N_j) + \frac{\alpha_5 - \alpha_6}{2}(n_j V_{jk} n_k - n_i V_{jk} n_k). \tag{5.11}$$

The viscous torque density, Γ_i is given by

$$\Gamma_i = \epsilon_{ijk}\sigma^a_{jk} \tag{5.12}$$

$$\Gamma_i = \epsilon_{ijk}[(\alpha_2 - \alpha_3)n_k N_j + (\alpha_5 - \alpha_6)n_k V_{jl} n_l] \tag{5.13}$$

where ϵ_{ijk} is the Levi-Civita tensor. If the liquid crystal is at rest, the second term on the right hand side of (5.13) disappears and the viscous torque density is given by

$$\mathbf{\Gamma} = -\gamma_1 \dot{\phi}, \tag{5.14}$$

where $\gamma_1 = \alpha_2 - \alpha_3$ is the rotational viscosity coefficient and $\dot{\phi} = \mathbf{n} \times \dot{\mathbf{n}}$ is the angular velocity in the absence of shear flow. If the director is rotating with an angular velocity $\dot{\phi}$ then the viscous torque $\mathbf{M}$ is given by

$$\begin{aligned} \mathbf{M} &= \mathbf{\Gamma} V \\ &= -\gamma_1 \dot{\phi} V, \end{aligned} \tag{5.15}$$

where V is the volume. This is illustrated schematically in Fig. 5.3.

The rotational viscosity is a key liquid crystal property for display devices. For example, the switching times for a twisted nematic display are given by [208]

$$\tau_{on} = \frac{\gamma_1 d^2}{\epsilon_0 \Delta\epsilon} \frac{1}{U^2 - U_0^2} \tag{5.16}$$

$$\tau_{off} = \frac{\gamma_1 d^2}{k\pi^2} \tag{5.17}$$

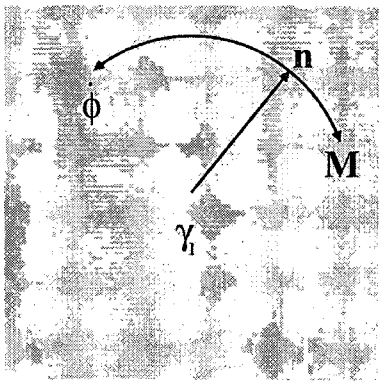

Figure 5.3: Schematic diagram of the viscous torque **M** acting on the director moving with an angular velocity $\dot{\phi}$.

where d is the cell thickness. In (5.16) ϵ_0 is the permitivity of free space, $\Delta\epsilon$ is the dielectric anisotropy, U is the operating voltage, and U_0 is the threshold voltage. In (5.17) k is a constant that depends on the elastic constants

$$k = k_{11} + \frac{1}{4}\left(k_{33} - 2k_{22}\right). \tag{5.18}$$

Other similar expressions hold for other display types all of which depend strongly on γ_1 [209].

5.3 Determination of γ_1 from Experiment

There are a number of techniques for determining γ_1 [207]. One method is the rotating field method. This involves applying a rotating electric or magnetic field [210, 211] to a suspended LC sample. The torque, M, exerted by a magnetic field, H, is given by

$$M = \frac{1}{2}\mu_0\chi_a H^2 V \sin 2(\psi - \phi) \tag{5.19}$$

where χ_a is the magnetic anisotropy, μ_0 is the permeability of free space, and V is the sample volume. When the field is rotated with a low angular velocity the director will follow the field with a constant phase lag of $\psi - \phi$. This is shown in

Fig. 5.4. Eventually the viscous and magnetic torque become equal

$$\gamma_1 \dot{\phi} = \frac{1}{2}\mu_0 \chi_a H^2 V \sin 2(\psi - \phi) \tag{5.20}$$

Increasing $\dot{\phi}$ increases the phase lag, until the maximum torque is exerted at $\psi - \phi = \frac{\pi}{4}$. The corresponding angular velocity is called the *critical angular velocity* $\dot{\phi}_c$, and is given by

$$\dot{\phi}_c = \frac{\mu_0 \chi_a H^2}{2\gamma_1}. \tag{5.21}$$

γ_1 can be determined in a particularly simple way by measuring the torque (through the twisting of the suspension wire) on the sample in field rotating with $\dot{\phi} < \dot{\phi}_c$ [212].

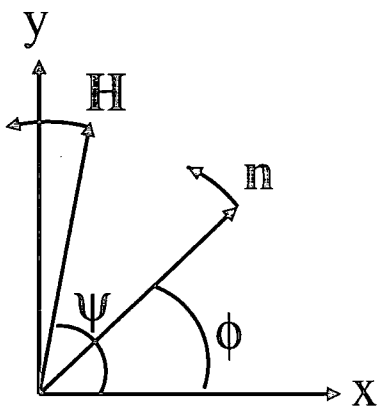

Figure 5.4: Schematic diagram showing director orientation in a rotating magnetic field.

The rotational viscosity coefficient can also be measured using director relaxation methods. A non-equilibrium orientation is produced and the time constant for relaxation back to equilibrium is determined. This deformation can be produced using either a magnetic [213] or electric field [214] and the relaxation process can be followed using optical or dielectric methods. Measuring the time τ to relax back to equilibrium gives the rotational viscosity [215–217]

$$\tau = \frac{2\gamma_1}{\mu_0 \chi_a H^2} \tag{5.22}$$

5.4 Calculation of γ_1 from Computer Simulation

One method based on experimental techniques for determining γ_1 was used recently by Manabe and Kuwajima [218]. They coupled an external field to the liquid crystal and allowed the system to equilibrate. The direction of the external field was then changed and the orientation of the director was monitored as a function of time. γ_1 was then determined from the time taken for the director reorientation. While this method gave good results for γ_1 the application of an external field is likely to change the orientational distribution of the molecules and hence the value of γ_1. Also for a system of flexible molecules it is not entirely clear how to couple the molecular long axis to an external field.

A second non-equilibrium method involves pinning the director in a shear flow, either by a using a *real* applied field such a magnetic field [219] or by using a director constraint [220]. If the director is held fixed at an angle θ and the shear rate is γ then [220, 221]

$$\langle p_2^a \rangle = -\frac{\gamma}{4}\gamma_1 - \frac{\gamma}{4}\gamma_2 \cos 2\theta \tag{5.23}$$

where $\mathbf{p}^a$ is the anti-symmetric part of the pressure tensor and $\gamma_2 = \alpha_5 - \alpha_6$. By performing shear flow simulations with the director pinned at different angles θ to the flow and calculating p_2^a as a function of θ, γ_1 and γ_2 may be found. As in the Manabe and Kuwijima method constraining the director is difficult for flexible, realistic models of mesogens. Additionally it is difficult to apply the Lees-Edwards (sliding brick) boundary conditions [222] needed for the shear flow for flexible molecules.

γ_1 can also be calculated from an equilibrium MD simulation by evaluating the appropriate Green-Kubo (GK) formulae. GK formulae were first derived by Forster [223] using the projector operator formalism. They were then rederived by Sarman and Evans [224] using linear response theory. The antisymmetric part of the pressure tensor is given by [206]

$$\langle p_\mu^a \rangle = \frac{\gamma_1}{2}\left[\Omega_\mu - \frac{1}{2}(\nabla \times \mathbf{v})_\mu\right] + \frac{\gamma_2}{4}\left[\epsilon_{\mu\nu\lambda} n_\nu n_\kappa + \epsilon_{\mu\nu\kappa} n_\nu n_\lambda\right] \nabla_\lambda u_\kappa \tag{5.24}$$

where $\boldsymbol{\Omega}$ is the director angular velocity, and $\mathbf{v}$ is the flow velocity. For purely rotational flow this reduces to

$$\langle p_\mu^a \rangle = \frac{1}{2}\Omega_\mu \gamma_1 \tag{5.25}$$

Using the linear response relation [222]

$$\langle B(t) \rangle = \langle B(0) \rangle - \beta \int_0^t dt' \langle B(t') \dot{H}_1(0) \rangle \tag{5.26}$$

and [224]

$$\dot{H}_1 = \lambda_2 \Omega_2 \tag{5.27}$$

we have

$$\gamma_1 = 2 \lim_{t\to\infty} \frac{\langle p_2^a(t) \rangle}{\langle \Omega_2(t) \rangle} \tag{5.28}$$

$$\gamma_1 = 2 \frac{\beta V \int dt \langle p_2^a(t) \Omega_2(0) \rangle}{\beta V \int dt \langle \Omega_2(t) \Omega_2(0) \rangle} \tag{5.29}$$

$$\gamma_1 = \frac{1}{\beta V \int dt \langle \Omega_2(t) \Omega_2(0) \rangle}. \tag{5.30}$$

The final expression (5.30) holds as $\beta V \int dt \langle \Omega_2(t) \Omega_2(0) \rangle = \frac{1}{2}$ (see Appendix A in Ref. [224])

An equivalent expression involving the mean squared displacement of the director can also be found. We have

$$\lim_{t\to\infty} \lim_{V\to\infty} V \frac{\langle |\mathbf{n}(t) - \mathbf{n}|^2 \rangle}{2t} = V \int dt \langle \Omega_2(t) \Omega_2(0) \rangle \tag{5.31}$$

which leads to

$$\gamma_1 = \lim_{t\to\infty} \lim_{V\to\infty} \frac{2t}{\beta V \langle |\mathbf{n}(t) - \mathbf{n}(0)|^2 \rangle_{eq}}. \tag{5.32}$$

Theoretical methods can be derived from the rotational diffusion model. Here it is assumed that each molecule moves in a mean field. The molecular orientational motion is assumed to be Brownian within this mean field. The rotational viscosity is then proportional to the energy barrier to molecular reorientation. Specifically in this method the state of the system is determined by the time dependent single particle orientational distribution function. The evolution of this is governed by

a Fokker-Planck type equation [225]. Several formulations of this technique exist, due to Osipov and Terentjev (OT) [225, 226], Nemtsov and Zakharov [227], and Fialkowski [228] which give the following formulae for γ_1

$$\gamma_1^{OT} = \frac{Nk_BT}{VD_\perp}\left[\frac{1}{6}\left(\frac{J_0\bar{P}_2}{k_BT}\right)^{\frac{1}{2}}\exp\left(\frac{J_0\bar{P}_2}{k_BT}\right)\right], \tag{5.33}$$

$$\gamma_1^{NZ} = \frac{Nk_BT}{VD_\perp}\left[\frac{3\bar{P}_2^2(3.181+0.757\bar{P}_2)}{2.881+\bar{P}_2+12.56\bar{P}_2^2+4.69\bar{P}_2^3-0.743\bar{P}_2^4}\right], \tag{5.34}$$

$$\gamma_1^{F} = \frac{NK_BT}{VD_\perp}\left[\frac{70\bar{P}_2^2}{16\bar{P}_4+5\bar{P}_2+14}\right], \tag{5.35}$$

where N is the number of molecules, T is the temperature, and $D_\perp$ is the rotational diffusion coefficient. $\bar{P}_2$ and $\bar{P}_4$ are the average second and fourth rank order parameters. In (5.33) J_0 is a constant, with a value given by mean field theory as $J_0 = 4.5k_BT_c$, where T_c is the clearing temperature. These formulae have been used to calculate γ_1 from simulation [229–231]. This in achieved by first calculating orientational time correlation functions (OTCF). The general OTCF is given by

$$\Phi^l_{mn}(t) = \frac{\langle D^{l*}_{mn}(\Omega(0))\, D^l_{mn}(\Omega(t))\rangle}{\langle D^{l*}_{mn}(\Omega(0))\, D^l_{mn}(\Omega(0))\rangle} \tag{5.36}$$

where D^l_{mn} is a Wigner rotation matrix element [232] and $\Omega(t) = (\theta, \phi, \psi)$ are the Euler angles that define the orientation of the molecular axis relative to the director frame. An exponential decay is then fitted to this and the decay time is used to calculate the rotational diffusion coefficient $D_\perp$. This is then inserted into (5.33), (5.34), and (5.35) to find γ_1.

5.5 Simulation Details

5.5.1 Computational Method

PCH5 molecules were represented using a harmonic all atom force field of the AMBER form [143] (4.16). The force field parameters were taken from the OPLS-AA

force field of Jorgensen *et al.* [153, 154, 170] and are shown in Tables 5.1, 5.2, and 5.3. The structure of PCH5 is shown in Fig. 5.5.

Angle	k_θ / kJ mol^{-1} rad^{-2}	θ_0 / deg
CA-CA-CZ	292.88	120.0
CA-CZ-NZ	711.28	180.0
CA-CA-CA	263.59	120.0
CA-CA-HA	146.66	120.0
CA-CA-CT	292.88	120.0
CA-CT-CT	263.59	114.0
CA-CT-HC	146.44	109.5
CT-CT-CT	244.35	112.7
CT-CT-HC	156.90	110.7
HC-CT-HC	138.07	107.8

Table 5.1: Bond angle bending parameters.

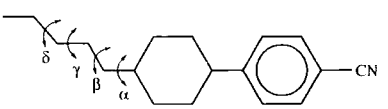

Figure 5.5: Structure of PCH5 showing dihedral angles α, β, γ, and δ.

The molecular dynamics simulations were performed using the DL_POLY package, version 2.12 [167]. To allow the use of a longer time step, bond lengths were constrained using the SHAKE algorithm [117]. The equations of motion were solved using the leap-frog algorithm with a time step of 2 fs. The calculations were performed in the NpT ensemble using a Nosé-Hoover thermostat and barostat [122–124] with relaxation times of 1 ps and 4 ps respectively. Electrostatic interactions were evaluated using an Ewald sum [115] with a convergence parameter of 0.34 Å^{-1} and 7 wave-vectors in the x, y, and z directions. A cut-off of 9 Å was applied to the

Dihedral	V_1	V_2	V_3
HC-CT-CT-HC	0.000	0.000	1.331
CT-CT-CT-HC	0.000	0.000	1.531
CT-CT-CT-CT	7.280	-0.657	1.167
HC-CT-CA-CA	0.000	0.000	0.000
CT-CT-CA-CA	0.000	0.000	0.000
HC-CT-CT-CA	0.000	0.000	1.933
CA-CA-CA-CA	0.000	39.748	0.000
CA-CA-CA-HA	0.000	39.748	0.000
HA-CA-CA-HA	0.000	39.748	0.000
CA-CA-CA-CZ	0.000	39.748	0.000
CA-CA-CZ-NZ	0.000	0.000	0.000

Table 5.2: Torsional parameters in kJ mol^{-1}.

short-ranged van der Waals interactions with corrections applied to the energy and virial. The pressure was set to 1 atmosphere.

The simulations were started from a simple cubic lattice of 125 molecules at a gas phase density. The initial state was a highly ordered nematic ($\bar{P}_2 \approx 0.9$). This was then rapidly compressed to a liquid state density (about 500-1000 kg m^{-3}). An equilibration run of about 1 ns was then performed after which statistics were then gathered over 4 ns at each temperature (300K, 310 K, 320K, and 330K).

5.5.2 Calculation of γ_1

5.5.2.1 Director Angular Velocity Correlation Function

The procedure to calculate γ_1 from the director angular velocity correlation function (DAVCF) (5.30) is as follows:

- calculate the director **n** from the long molecular axis found by diagonalizing

Atom Type	ϵ / kJ mol^{-1}	σ / Å	q / e
CA	0.293	3.550	-0.115
CA[1]	0.293	3.550	0.000
CA[2]	0.293	3.550	0.035
CT[3]	0.276	3.500	-0.180
CT[4]	0.276	3.500	-0.120
CT[5]	0.276	3.500	-0.060
CZ	0.628	3.650	0.395
HA	0.126	2.420	0.155
HC	0.126	2.500	0.060
NZ	0.711	3.200	-0.430

Table 5.3: Non-bonded parameters. Notes: (1) Bridging aromatic carbon (CA-CT), (2) aromatic carbon bonded to cyano carbon (CA-CZ), (3) aliphatic carbon (CH_3), (4) aliphatic carbon (CH_2), and (5) aliphatic carbon (CH).

the inertia tensor.

- check the director does not flip during the simulation (ensure that $\mathbf{n}(t).\mathbf{n}(t+\delta t) > 0$)
- calculate $\dot{\mathbf{n}} = \frac{d\mathbf{n}}{dt}$.
- calculate director angular velocity

$$\boldsymbol{\Omega} = \mathbf{n} \times \dot{\mathbf{n}} \tag{5.37}$$

- transform into director based frame of reference, with $\mathbf{n} = (0, 0, 1)$ and $\boldsymbol{\Omega} = (\Omega_1, \Omega_2, 0)$.

The transformation into the director fixed frame is important as (5.30) was derived under the assumption of constant director orientation and the motion of the director

can have a large effect on the values of transport coefficients for small system sizes [233]. This transformation is achieved using the rotation matrix constructed from the eigenvectors of the ordering tensor

$$\begin{aligned} \mathbf{u}_1 &= (u_{1x}, u_{1y}, u_{1z}) \\ \mathbf{u}_2 &= (u_{2x}, u_{2y}, u_{2z}) \\ \mathbf{u}_3 &= (u_{3x}, u_{3y}, u_{3z}) \end{aligned} \tag{5.38}$$

The angular momentum in the director fixed frame is then given by

$$\begin{pmatrix} \Omega'_1 \\ \Omega'_2 \\ \Omega'_3 \end{pmatrix} = \begin{pmatrix} u_{1x} & u_{1y} & u_{1z} \\ u_{2x} & u_{2y} & u_{2z} \\ u_{3x} & u_{3y} & u_{3z} \end{pmatrix} \begin{pmatrix} \Omega_x \\ \Omega_y \\ \Omega_z \end{pmatrix} \tag{5.39}$$

where $\Omega'_3 = 0$.

To obtain good statistics, it is necessary to average the DAVCF over many different time origins. γ_1 is then calculated by integrating the DAVCF.

5.5.2.2 Director Mean Squared Displacement

The procedure to calculate γ_1 from the director mean-squared displacement (DMSD) is as follows:

- calculate director $\mathbf{n}$
- check the director does not flip during the simulation (as in §5.5.2.1)
- calculate the mean squared director displacement ($\langle|\mathbf{n}(t) - \mathbf{n}(0)|^2\rangle$)

Again this is averaged over many different time origins to obtain good statistics. γ_1 is then calculated from the gradient of the director mean squared displacement. At long times the mean squared displacement takes on a linear form

$$\langle|\mathbf{n}(t) - \mathbf{n}(0)|^2\rangle = mt + c \tag{5.40}$$

where m is the gradient. γ_1 is then given by

$$\gamma_1 = \frac{2}{m\beta V}. \tag{5.41}$$

Again, averaging over many time origins is required for good statistics.

5.5.2.3 Rotational Diffusion

Calculation of γ_1 using the rotational diffusion model requires knowledge of the order parameters and the rotational diffusion coefficient $D_\perp$. The order parameters are calculated from the simulation trajectories in the usual way. To calculate $D_\perp$ we need to calculate the decay time of the OTCF (5.36). OTCFs with $m = 0$, $n = 0$, and $l = 2$ are calculated (these being determined solely by tumbling motion).These require the Wigner rotation matrix elements $D^2_{00}(\Omega)$ which in terms of the Euler angles that define the orientation of the molecular axis relative to the director frame. These are [232]

$$D^2_{00}(\Omega(t)) = \frac{3}{2}\cos^2\theta(t) - \frac{1}{2}. \tag{5.42}$$

$\Phi^2_{00}(t)$ is then

$$\begin{aligned} \Phi^2_{00}(t) &= \frac{\langle D^2_{00}(\Omega(t)) D^2_{00}(\Omega(0))\rangle}{\langle D^2_{00}(\Omega(0)) D^2_{00}(\Omega(t))\rangle} \\ &= \frac{\left\langle \left(\frac{3}{2}\cos^2(\theta(0)) - \frac{1}{2}\right)\left(\frac{3}{2}\cos^2(\theta(t)) - \frac{1}{2}\right)\right\rangle}{\left\langle \left(\frac{3}{2}\cos^2(\theta(0)) - \frac{1}{2}\right)\left(\frac{3}{2}\cos^2(\theta(0)) - \frac{1}{2}\right)\right\rangle} \end{aligned} \tag{5.43}$$

At long times $\Phi^2_{00}(t) = \langle P_2\rangle^2$. The decay time τ^l_{nm} can then be found by fitting an exponential decay to $\Phi^2_{00}(t) - \langle P_2\rangle^2$. $D_\perp$ can then be found from [234]

$$D^2_\perp = \frac{7 + 10\bar{P}_2 + 18\bar{P}_4 - 35\bar{P}_2}{(7 + 5\bar{P}_2 - 12\bar{P}_4)\tau^2_{00}}. \tag{5.44}$$

γ_1 can then be found from (5.33),(5.34), and (5.35). The molecular axis, and hence the director, have been calculated using two methods. In the first the molecular axis is the long axis found from diagonalising the inertia tensor (3.52), and in the second the molecular axis is taken to be the molecular dipole axis.

5.6 Results

5.6.1 Densities

The system density ρ was monitored throughout the simulations. The final values for ρ are shown in Tab. 5.4. These are in excellent agreement with the experimental values [235]. The density is sensitive to the values of the intermolecular parameters: small changes to these can lead to large changes in the calculated values of ρ.

T / K	V / Å^3	ρ / kg m^{-3}	ρ_{expt} / kg m^{-3}
300	54548±302	978.8±5.4	963
310	54853±315	973.3±5.6	956.5
320	55262±384	966.1±6.7	949.6
330	55558±345	961.0±6.0	-

Table 5.4: Box volume and densities from simulations of PCH5.

5.6.2 Order Parameters

The order parameters have also been calculated from the simulation trajectories. They are shown in Tab. 5.5 along with experimental values calculated from Raman scattering experiments [236]. Both $\bar{P}_2$ and $\bar{P}_4$ have been calculated using two different definitions of the molecular axis. In the first, the molecular axis is the long axis found by diagonalizing the inertia tensor (3.52). In the second, the long axis is taken to be the molecular dipole axis. As can be seen both definitions give order parameters that are higher than the experimental values and relatively constant across the temperature range considered.

This lack of perfect agreement is not altogether surprising. Studies of single site models have shown strong system size effects and so for a small system of 125 molecules we would not expect to be able to predict the phase transition temperature

accurately or avoid super-heating the nematic past the actual transition temperature. The lack of strong temperature dependence of the order parameters is also consistent with previous studies of relatively small numbers of molecules [98].

T / K	$\bar{P}_2^{inertia}$	$\bar{P}_4^{inertia}$	$\bar{P}_2^{dipole}$	$\bar{P}_4^{dipole}$	$\bar{P}_2^{expt}$	$\bar{P}_4^{expt}$
300	0.79±0.01	0.46±0.01	0.63±0.02	0.20±0.03	0.63	0.25
310	0.81±0.02	0.49±0.02	0.65±0.02	0.23±0.03	0.58	0.21
320	0.84±0.04	0.57±0.05	0.64±0.04	0.21±0.05	0.50	0.15
330	0.83±0.01	0.54±0.02	0.63±0.03	0.21±0.04	0.00	0.00

Table 5.5: Calculated and experimental order parameters for PCH5.

The translational order can be examined by calculating the centre of mass radial distribution function (RDF). The RDF, $g(r)$ and its component parallel to the director $g_{\parallel}(r)$ for each temperature are shown in Fig. 5.6. At 300 K, $g(r)$ shows two peaks at about 6 Å and 10 Å. At higher temperatures the second peak disappears and the peak at about 6 Å grows stronger. $g_{\parallel}(r)$ shows no periodic variation indicating a nematic phase.

5.6.3 Molecular Structure

The molecular structure in the nematic phase has been examined by calculating the dihedral angle distributions of several key dihedral angles in the molecules. These are shown in Fig. 5.7. These are peaked around the potential minima for each dihedral angle, which in the case of the β, γ, and δ dihedrals corresponds to the *trans* configuration. For the α dihedral there is a double degeneracy at about 65° and 180°. The γ dihedral has the largest *gauche* populations. These results are consistent with previous atomistic simulations of the mesogen CCH5 [82, 83].

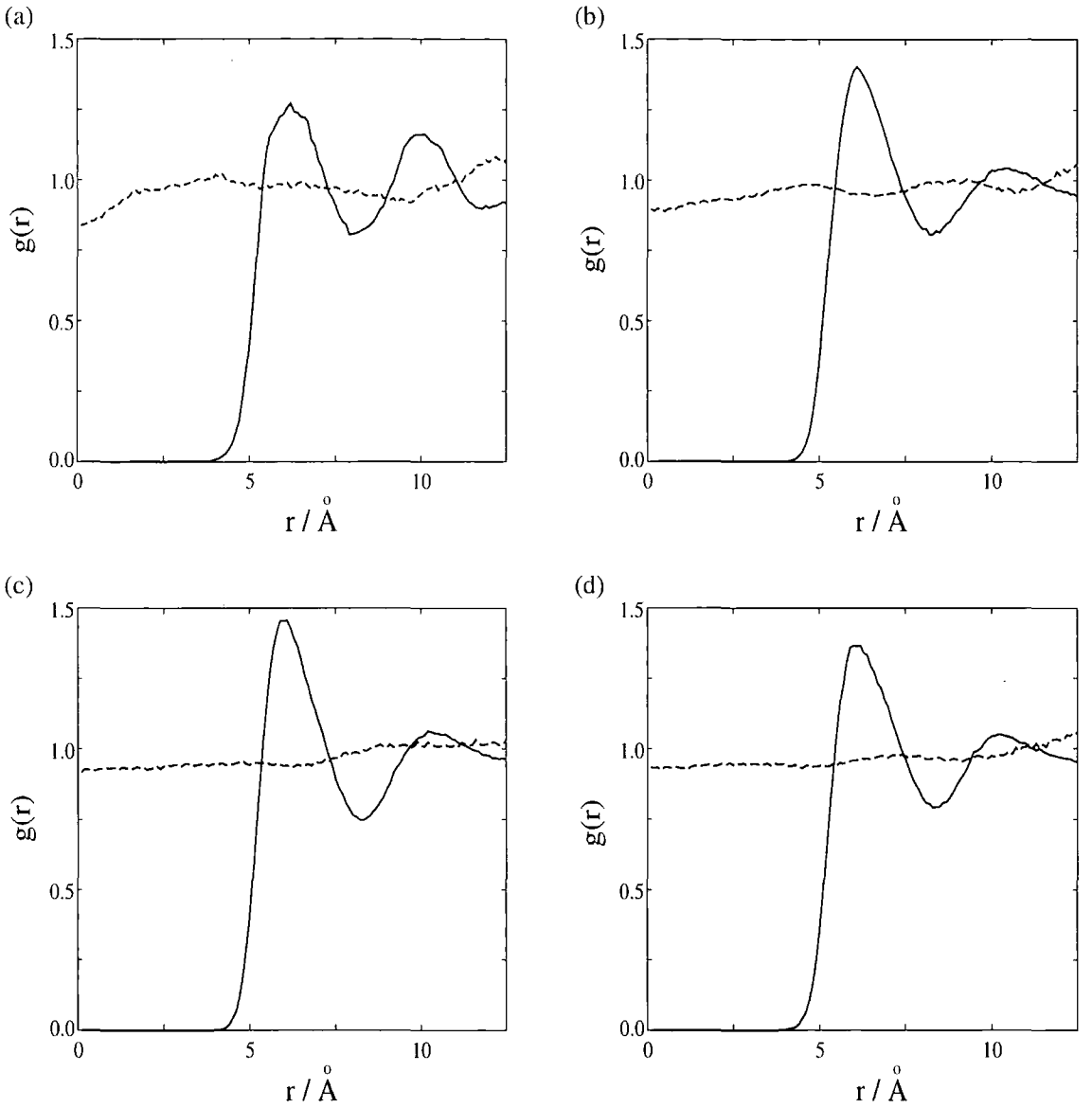

Figure 5.6: Radial distribution functions $g(r)$ and $g_{\parallel}(r)$ for simulated PCH5 at (a) 300 K, (b) 310 K, (c) 320 K, and (d) 330 K. The solid lines show $g(r)$ and the dashed lines show $g_{\parallel}(r)$.

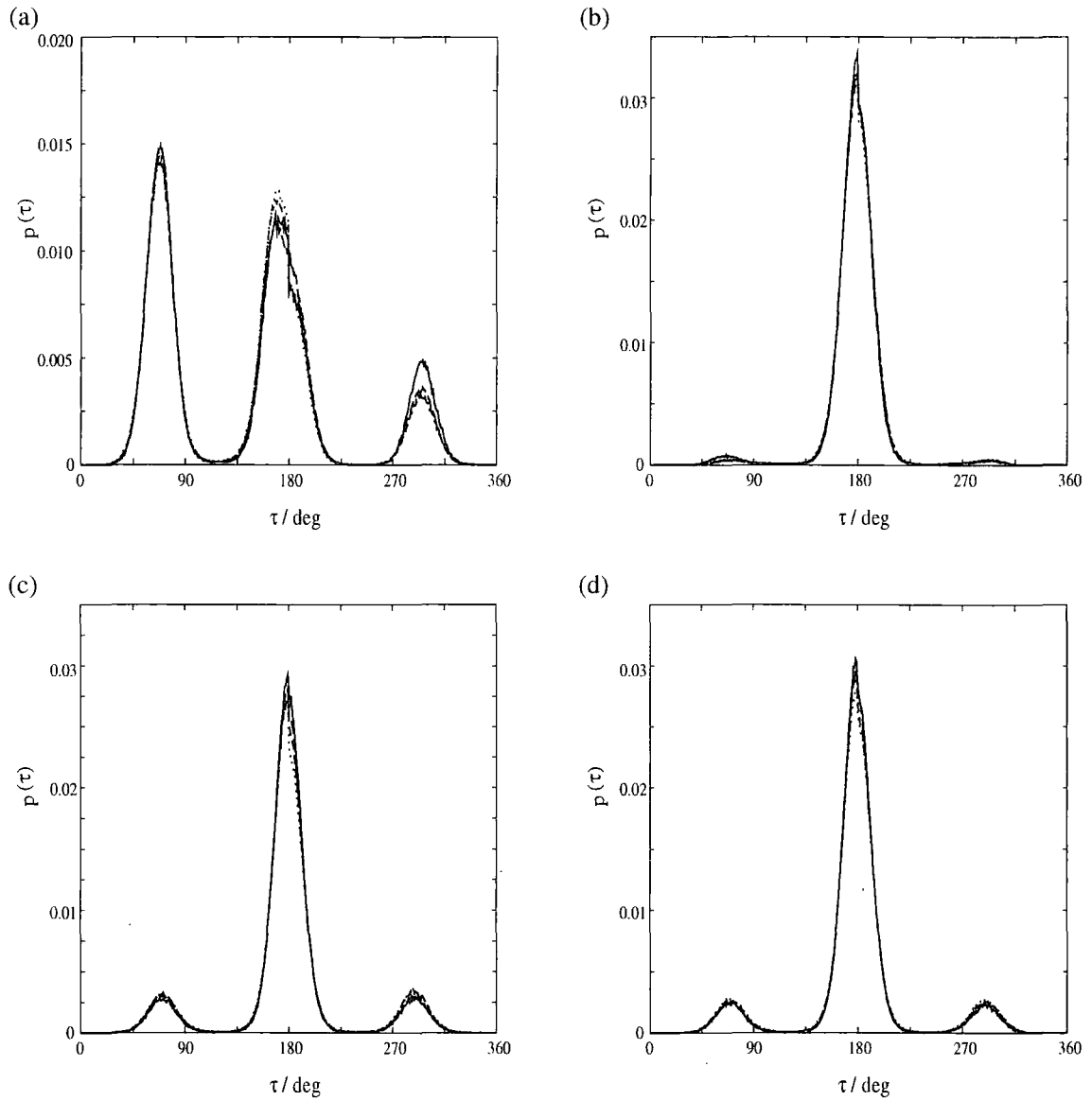

Figure 5.7: Dihedral angle distributions for (a) dihedral α, (b) dihedral β, (c) dihedral γ, and (d) for dihedral δ. The dihedral angles α, β, γ, and δ are defined in Fig. 5.5. In all cases the solid line is the distribution at 300 K, the long dashed line is the distribution at 310 K, the short dashed line is the distribution at 320 K, and the dotted line is the distribution at 330 K.

5.6.4 Rotational Viscosity coefficient γ_1

Presented here are the values of the rotational viscosity coefficient γ_1 calculated using the different methods outlined in §5.5.2.

The director angular velocity correlation function was calculated using (5.30) for each simulation temperature. The calculated correlation functions are shown in Fig. 5.8. The function has the same form at each temperature; from an initial value the function rapidly goes through zero before reaching a minima and decaying to zero.

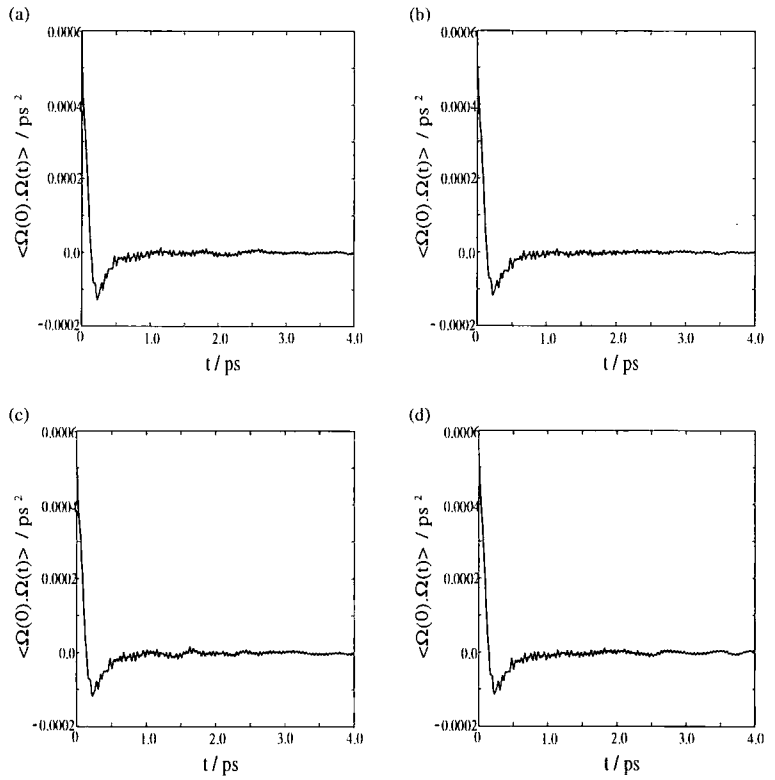

Figure 5.8: Calculated director angular velocity correlation functions

The DAVCF was then integrated to give γ_1 from (5.30). Calculated values of γ_1 for each temperature are shown in Tab. 5.6. There are relatively large errors on these values. This is due to the large amount of noise on the DAVCF.

The director mean-squared displacement was calculated (5.32) as a function of time, as shown in Fig. 5.9. As can be seen at long times the director mean-squared

T / K	$\int_0^\infty \langle \Omega_2(t).\Omega_2(0) \rangle \, dt$ / ps^{-1}	γ_1 / mPa s
300	0.879×10^{-6}	86.3±11.0
310	1.179×10^{-6}	66.2±8.4
320	2.966×10^{-6}	27.0±3.4
330	2.692×10^{-6}	30.5±4.0

Table 5.6: Integrals of the director angular velocity function and calculated values of γ_1.

displacement shows a linear form, with the gradient increasing with temperature.

The gradient of the director mean-squared displacement has been found and used to calculate γ_1. These values are shown in Tab. 5.7. They are in good agreement with those calculated using the director angular velocity correlation function method shown in Tab. 5.6. The values of γ_1 calculated using the DMSD have smaller uncertainties than those calculated using the DAVCF. The reason for this is clearly seen by comparing the clear linear form of the DMSD shown in Fig. 5.9 and the relatively noisy DAVCF in Fig. 5.8.

T / K	$\lim_{t\to\infty} \frac{\langle \lvert \mathbf{n}(t)-\mathbf{n}(0) \rvert^2 \rangle}{t}$ / ps^{-1}	γ_1 / mPa s
300	1.577×10^{-6}	96.3±0.5
310	3.094×10^{-6}	50.7±0.3
320	4.128×10^{-6}	38.7±0.3
330	8.827×10^{-6}	18.6±0.1

Table 5.7: Gradients of the director mean-squared displacement and calculated values of γ_1.

The OTCF $\Phi^2_{00}(t)$ was calculated using the method outlined in §5.5.2.3. For comparison both the inertia tensor and dipole moment definition of the molecular long axis were used. These are shown in Fig. 5.10. The decay times were then

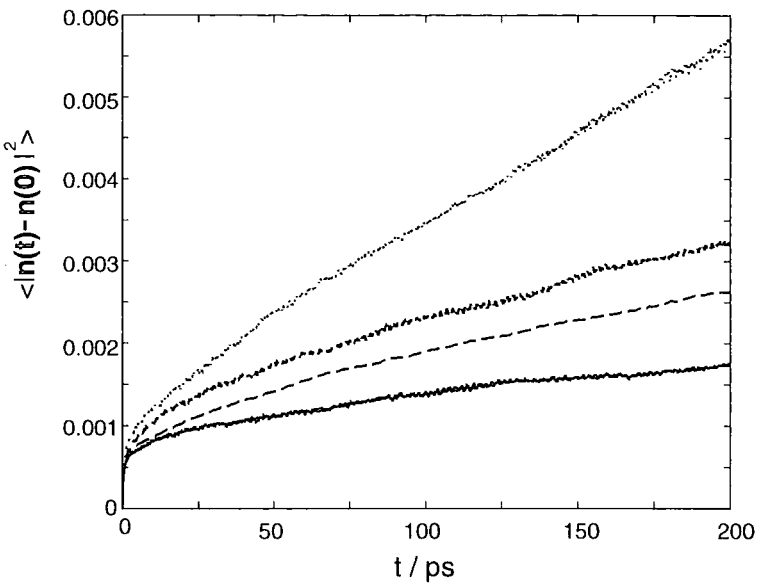

Figure 5.9: Director mean-squared displacement against time for simulated PCH5. Data for 300 K is shown by the solid line, 310 K shown by the long dashed line, 320 K shown by the dashed line, and 330 K shown by the dotted line.

found and used along with the order parameters (from Tab. 5.5) to calculate the rotational diffusion coefficients $D_\perp$ using (5.42). These are shown in Tab. 5.8.

The values of $D_\perp$ were used to calculate γ_1 for each of the different formulations of the rotational diffusion model. These are presented in Tables 5.9, 5.10, and 5.11. As can be seen the values calculated using the Osipov-Terentjev formula (5.33) give results about an order of magnitude higher than those calculated using the Nemtsov-Zakharov (5.34) and Fialkowski (5.35) formulae. This was also observed in a previous simulation study [229] and arises due to the exponential dependence of (5.33) on $\bar{P}_2$. Previously a modified form of the OT formula was proposed by Wu and Wu [237]

$$\gamma_1 = g_0 \left(\frac{T}{T_c}\right)^4 \left(\frac{E_1}{k_B T_c}\right)^{-3} \left(\frac{J_0 \bar{P}_2}{k_B T_c}\right)^{\frac{1}{2}} \exp\left(\frac{E_1 + J_0 \bar{P}_2}{k_B T}\right) \tag{5.45}$$

where g_0 is a proportionality constant and E_1 is the activation energy. For PCH5 these have been estimated to be $g_0 = 0.0645$ mPa s and $E_1 = 5.548 \times 10^{-20}$ J ,

T / K	$\tau^2_{00\,inertia}$	$\tau^2_{00\,dipole}$	$D^2_{\perp\,inertia}$	$D^2_{\perp\,dipole}$
300	459.7	538.4	0.89	1.52
310	888.1	552.6	0.34	1.15
320	739.1	331.6	0.50	1.86
330	618.7	247.0	0.52	2.80

Table 5.8: Decay times τ^2_{00} and rotational diffusion coefficients $D^2_\perp$ for simulated PCH5. τ^2_{00} in ps, $D^2_\perp$ in $\times 10^{-4}$ ps^{-1}.

T / K	$\gamma_{1\,OT}^{inertia}$ / mPa s	$\gamma_{1\,OT}^{dipole}$ / mPa s	$\gamma_{1\,Wu}^{inertia}$ / mPa s	$\gamma_{1\,Wu}^{dipole}$ / mPa s
300	825.7±47.2	283.4±28.1	257.5±9.9	150.6±11.2
310	2723.6±122.9	373.5±30.0	166.5±6.3	99.0±7.2
320	2563.4±401.8	249.1±30.3	114.2±18.4	60.7±8.3
330	2708.2±78.5	177.3±13.8	71.1±2.6	38.3±3.9

Table 5.9: γ_1 calculated using the Osipov-Nemtsov formula (5.33) The values in the last two columns were calculated using the modified formula due to Wu and Wu (5.45).

while $J_0 = 2.42 k_B T_c$ [237]. γ_1 has been calculated using (5.45) and the calculated values are shown in Tab. 5.9. As can be seen these values are much lower than those found from the original formula. However g_0, E_1 and J_0 in (5.45) are parameters fitted to experimental data for PCH5; consequently different values of these parameters are needed for each different liquid crystal compound, reducing the predictive power of this method. The values of γ_1 calculated using the Nemtsov-Zakharov and Fialkowski formulae are closer to the values calculated using the first two methods. These values have large statistical errors, in some cases greater than the measured value.

T / K	$\gamma_1^{inertia}$ / mPa s	γ_1^{dipole} / mPa s
300	55.6±3.7	36.0±10.4
310	148.7±4.1	39.6±9.9
320	108.0±15.9	24.7±20.0
330	104.8±3.7	16.6±15.3

Table 5.10: γ_1 calculated using the Nemtsov-Zakharov formula (5.34).

T / K	$\gamma_1^{inertia}$ / mPa s	γ_1^{dipole} / mPa s
300	183.6±41.6	107.8±81.7
310	498.3±43.7	120.0±82.0
320	362.4±202.3	74.8±163.2
330	352.1±42.6	49.2±120.9

Table 5.11: γ_1 calculated using the Fialkowski formula (5.35).

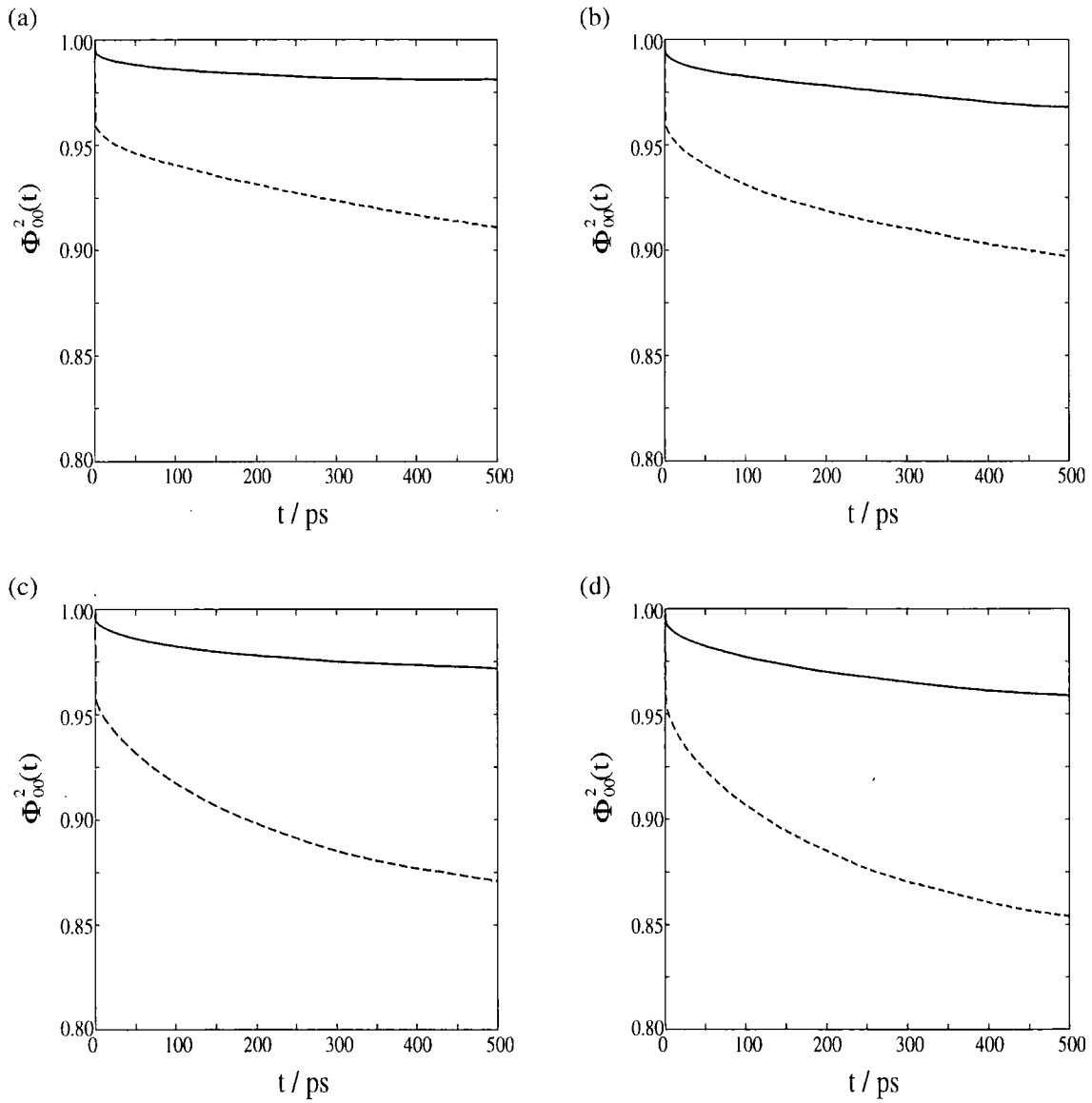

Figure 5.10: Orientational time correlation function $\Phi^2_{00}(t)$ for simulated PCH5 at (a) 300 K, (b) 310 K, (c) 320 K, and (d) 330 K. In all graphs the solid line denotes the correlation functions obtained using the molecular long axis and the dashed line denotes the correlation function obtained using the molecular dipole axis.

Shown in Tab. 5.12 are experimental values of γ_1 [219,235] along with the values calculated from the methods above. These are also plotted in Fig. 5.11. The experimental values were determined using the rotating magnetic field method as outlined in §5.3.

The values of γ_1 calculated using the director angular velocity correlation function and director mean-squared displacement are in good agreement with each other and the experiment. The agreement between each other is expected as both methods are formally equivalent; the mean-squared displacement method is the Einstein relation corresponding to the director angular velocity correlation function method. However, the errors in the DAVCF method are significantly larger than those for the DMSD method. This is due to the large amount of statistical noise on the director angular velocity correlation function that leads to large errors in the calculated integrals. In contrast the director mean-squared displacement curves show a clear linear form.

T / K	γ_1^{expt}	γ_1^{davc}	γ_1^{dmsd}	γ_1^{OT}	γ_1^{NZ}	γ_1^{F}
300	83.2±1.2[1]	86.3±11.0	96.3±0.5	190.7±10.8	36.0±10.8	107.8±81.0
310	61.0±0.9[2]	66.2±8.4	50.7±0.3	584.7±10.8	39.6± 9.7	120.0±81.3
320	32.6±0.5	27.0±3.4	38.7±0.3	502.0±10.8	24.7±19.8	74.8±162.6
330	-	30.5±4.0	18.6±0.1	516.6±10.8	16.9±12.7	50.5±100.9

Table 5.12: Comparison between calculated and experimental values of γ_1. The experimental values at 303.5 K and 320.0 K were taken from [235] while the value at 308 K was taken from [219]. All γ_1 values in mPa s. Notes: (1) T=303.5 K, (2) T=308 K.

Comparison between the experimental values of γ_1 and those calculated using the rotational diffusion method is less favourable. As mentioned previously, the Osipov-Terentjev results are an order of magnitude higher than those obtained using the other methods. The Nemtsov-Zakharov and Fialkowski results are in qual-

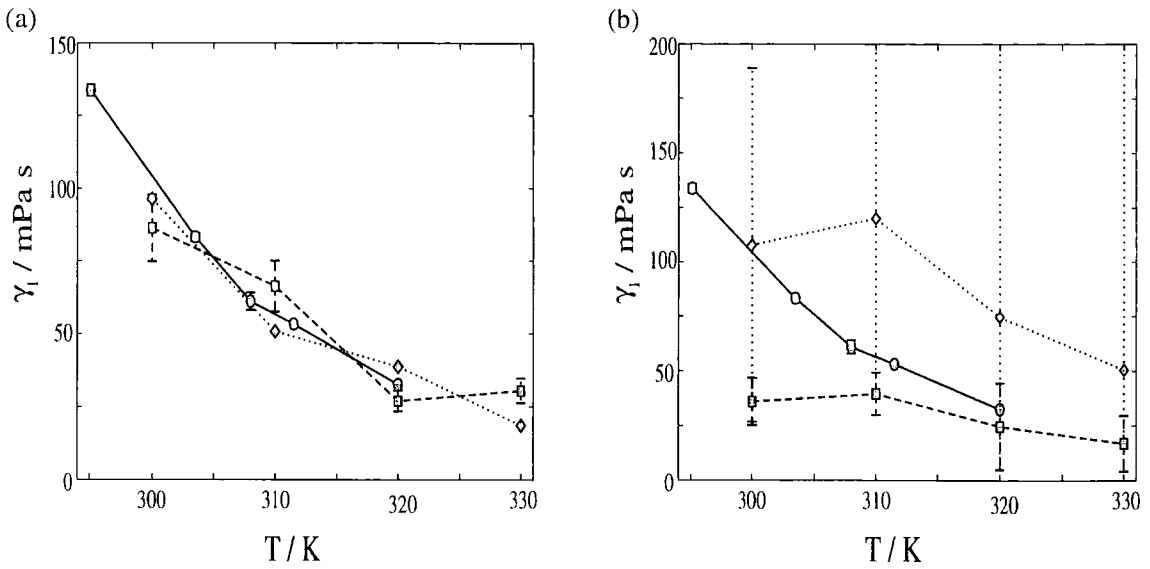

Figure 5.11: Comparison of experimental and calculated values of γ_1. In (a) The experimental values of γ_1 are marked by the circles joined by the solid line, γ_1 calculated from the director angular velocity correlation function (5.30) are marked by the squares joined by the dashed line, and γ_1 calculated from the director mean squared displacement are shown by the diamonds joined by the dotted line. In (b) the experimental values of γ_1 are denoted by the circles joined by the solid line, γ_1 calculated using the Nemtsov-Zakharov formula (5.34) are shown by the squares joined by the dashed line, and γ_1 calculated using the Fialkowski formula are shown by the diamonds joined by the dotted line.

itative agreement with experiment, with the NZ formula underestimating and the Fialkowski formula overestimating γ_1. This has been observed before in a previous simulation study [229]. The poor agreement with experiment can be due to the explicit dependence on the order parameters. To test this γ_1 has been calculated from (5.33), (5.34), and (5.35) using the experimental values for the order parameters (Tab. 5.5). These values are shown in Tab. 5.13. The use of experimental order parameters has a large effect on γ_1 calculated using (5.35), lowering the magnitude of the calculated values bringing them closer to experiment. This is due to the explicit

dependence on $\bar{P}_4$ in (5.35) that is absent in (5.33) and (5.34).

T / K	γ_1^{expt} / mPa s	γ_1^{OT} / mPa s	γ_1^{NZ} / mPa s	γ_1^{F} / mPa s
300	83.2	201.3	25.6	73.7
310	61.0	153.2	34.2	92.8
320	36.2	57.1	9.7	23.8

Table 5.13: γ_1 values calculated using experimental order parameters (Tab. 5.5) and orientational decay times calculated from simulation.

5.7 System Size Dependence

To test the dependence of the calculated values of γ_1 on the size of the simulated system, simulations of a larger (216 molecule) system have been performed. This has been simulated using the force field developed in Chapter 4. Force field parameters for this system are shown in Tables 4.3, 4.4, 4.6, and 4.9. The full details of this system will be discussed in Chapter 6. The quantities relevant for the calculation of γ_1 are shown in Tab. 5.14.

T / K	V / Å^3	$\bar{P}_2^{inertia}$	$\bar{P}_4^{inertia}$	$\bar{P}_2^{dipole}$	$\bar{P}_4^{dipole}$
300	92468±688	0.68±0.02	0.31±0.01	0.45±0.01	0.06±0.01
310	92912±745	0.65±0.01	0.27±0.00	0.47±0.00	0.08±0.00
320	94033±777	0.55±0.03	0.23±0.01	0.39±0.01	0.07±0.00
330	94829±761	0.50±0.04	0.20±0.02	0.36±0.02	0.08±0.01

Table 5.14: System volumes and order parameter for simulated PCH5 (216 molecules).

As can be seen $\bar{P}_2$ and $\bar{P}_4$ in the 216 molecule system are lower than those in the 125 molecule system. This is especially true for the order parameters calculated

from the dipole axis, which are now lower than the Raman scattering results shown in Tab. 5.5. They also show a wider variation across the temperature range than in the 125 molecule system, in better agreement with the experimental values. This can be attributed to an improvement in the representation in the long range order of the system. This improvement with system size has been seen in studies of dipole correlations in isotropic PCH5 [106].

The director angular velocity correlation functions were calculated as outlined in §5.5.2.1. The calculated correlation functions are shown in Fig. 5.12. The DAVCF

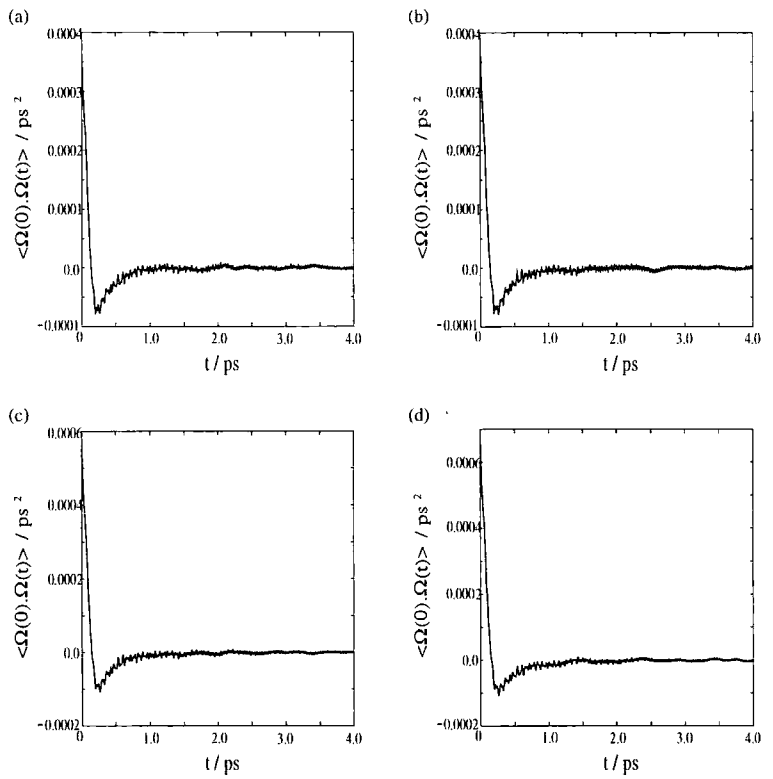

Figure 5.12: Director angular velocity correlation functions for simulated PCH5 at (a) 300 K, (b) 310 K, (c) 320 K, and (d) 330 K.

has been integrated to given γ_1 and these values are shown in Tab. 5.15, along with results for the 125 molecule system and the experimental results. As can be seen, there is no improvement in the calculated values of γ_1 for the 216 molecule system

compared to the 125 molecule system. This is probably caused by the higher density of the 216 molecule system compared to the 125 molecule system. The temperature dependence of γ_1 in the 216 molecule system is in better agreement with experiment in that it doesn't show an increase between 320 and 330 K. The statistical errors are also smaller in the 216 molecule system than in the 125 molecule system.

T / K	$\int_0^\infty \langle \Omega_2(t).\Omega_2(0) \rangle \, dt$ / ps^{-1}	γ_1^{216} / mPa s	γ_1^{125} / mPa s	γ_1^{expt} / mPa s
300	0.507×10^{-6}	88.3±8.8	86.3±11.0	83.2±1.2[1]
310	0.820×10^{-6}	56.2±3.1	66.2±8.4	61.0±0.9[2]
320	2.030×10^{-6}	23.1±2.3	27.0±3.4	32.6±0.5
330	8.727×10^{-6}	5.5±1.0	30.5±4.0	-

Table 5.15: Integrals of the director angular velocity function and calculated values of γ_1 for the 216 molecule system. γ_1^{216} are the calculated values of the rotational viscosity coefficient for the 216 molecule system, γ_1^{125} are the calculated values of the rotational viscosity coefficient for the 125 molecule system and γ_1^{expt} are the experimental values of the rotational viscosity coefficient. Notes: (1) T=303.5 K, (2) T=308 K.

The director mean-squared displacement has been calculated as outlined in §5.5.2.2. The calculated mean-squared displacements are shown in Fig. 5.13. By comparing Fig. 5.9 and Fig. 5.13 it can be seen that director motion in the larger system is slower. Shown in Tab. 5.16 are the gradients of the director mean squared displacement and the values of γ_1 calculated from these. Also listed in Tab. 5.16 are the equivalent values from the 125 molecule system and the experimental values. The values of γ_1 calculated from the 216 molecule system are generally in better agreement with experimental values than those calculated from the 125 molecule system. This is expected as (5.32) was derived in the thermodynamic limit, so an increase in system size should bring about an improvement in the calculated values.

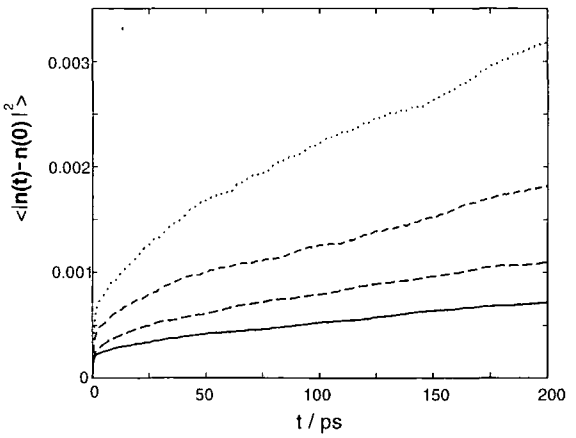

Figure 5.13: Director mean-squared displacement for simulated PCH5 (216 molecule system). Solid line shows data at 300 K, long dashed line shows data at 310 K, short dashed line shows data at 320 K, and dotted line shows data for 330 K.

Also noticeable is the decrease in the errors in the calculated values of γ_1.

The values of γ_1 calculated using the DAVCF and DMSD methods and the experimental values of γ_1 are plotted as a function of temperature in Fig. 5.14, along with the values of γ_1 calculated for the 125 molecule system. As can be seen, both the DAVCF and DMSD methods are in good agreement with experiment below the nematic-isotropic transition temperature.

T / K	$\lim_{t\to\infty} \frac{\langle\|\mathbf{n}(t)-\mathbf{n}(0)\|^2\rangle}{t}$ / ps^{-1}	γ_1^{216} / mPa s	γ_1^{125} / mPa s	γ_1^{expt} / mPa s
300	1.05×10^{-6}	85.3±0.0	96.3±0.5	83.2±1.2[1]
310	1.62×10^{-6}	56.7±0.0	50.7±0.3	61.0±1.2[2]
320	2.83×10^{-6}	33.4±0.0	38.7±0.3	32.6±1.2
330	4.90×10^{-6}	19.6±0.0	18.6±0.1	-

Table 5.16: Director mean-squared displacements and calculated rotational viscosity coefficients for simulated PCH5 (216 molecule system). γ_1^{216} is the calculated rotational viscosity coefficient for the 216 molecule system, γ_1^{125} is the calculated rotational viscosity coefficient for the 125 molecule system, and γ_1^{expt} is the experimental rotational viscosity coefficient. Notes: (1) T=303.5 K, (2) T=308 K.

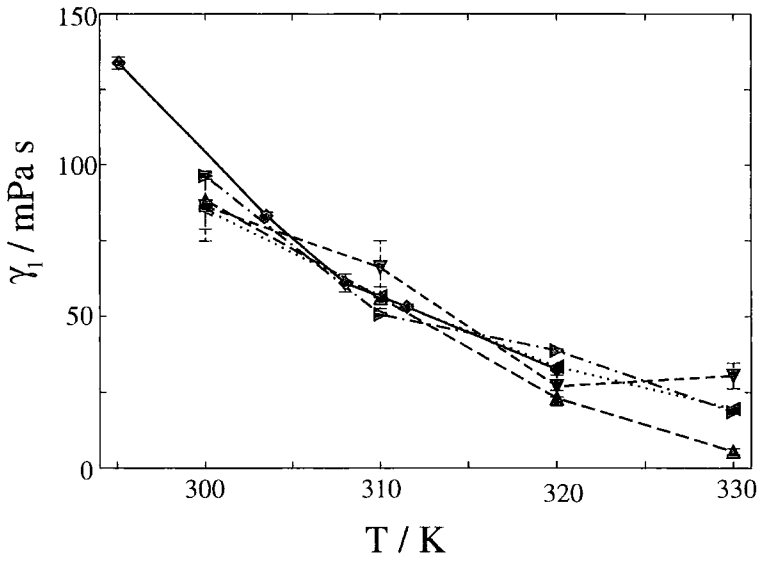

Figure 5.14: Comparison between experimental and values of γ_1 calculated using the DAVCF and DMSD approaches. The experimental values are marked by diamonds, the values calculated from DAVCF for the 216 molecule system are marked by the upright triangles, the DAVCF results for the 125 molecule system are marked by downward pointing triangles, the DMSD results for the 216 molecule system are marked by the left pointing triangles, and the DMSD results for the 125 molecule system are marked by the right pointing triangles.

The OTCF $\Phi^2_{00}(t)$ has been calculated as described in §5.5.2.3 and have been plotted in Fig. 5.15. In all cases $\Phi^2_{00}(t)$ calculated using the dipole moment definition of the molecular axis decays quicker than that calculated from the inertia tensor. This is expected from the lower values of the order parameter found using the dipole axis. As before, the decay times τ^2_{00} have been calculated by fitting an exponential decay to $\Phi^2_{00}(t)$ and have been used to calculate the rotational diffusion coefficients. These are shown in Tab. 5.17. For the 216 molecule system the rotational diffusion coefficients increase with temperature, in contrast to the 125 molecule system, which shows no clear trend. This improvement arises due to the improved temperature dependence of the order parameters and decay times τ^2_{00}.

T / K	$\tau^2_{00inertia}$	$\tau^2_{00dipole}$	$D^2_{\perp\, inertia}$	$D^2_{\perp\, dipole}$
300	1053.8	468.1	0.76	2.29
310	870.8	416.3	0.98	2.58
320	1166.4	403.1	1.24	3.49
330	774.2	318.1	2.08	5.01

Table 5.17: Decay times and rotational diffusion coefficients with $l = 2$ for simulated PCH5. τ^2_{00} in ps, $D^2_\perp$ in $\times 10^{-4}$ ps^{-1}.

The calculated rotational diffusion coefficients and order parameters have been used to calculate γ_1 as above and results for the 216 molecule system are shown in Tab. 5.18, 5.19, and 5.20. The strong dependence of these methods on the values of the order parameters can clearly be seen. For the 216 molecule system γ_1 calculated using (5.33) is significantly smaller than those calculated for the 125 molecule system. In some cases the results differ by an order of magnitude. The exponential form of (5.33) and (5.45) imply that small changes to the order parameters have a large effect on γ_1. Thus the decrease in $\bar{P}_2$ leads to a large decrease in γ_1. γ_1 calculated using (5.34) and (5.35) generally show a marked decrease between the 125 and 216 molecule systems, due to the lower values of the order parameters in the 216 molecule system.

The values of γ_1 calculated from (5.34) and (5.35) are compared to experimental values of γ_1 in Fig. 5.16. As can be seen in both cases $\gamma_1^{216\, inertia}$ falls toward zero with increasing temperature. After an initial rise, caused by the anomalous increase in $\bar{P}_2^{dipole}$ between 300 K and 310 K, $\gamma_1^{216\, dipole}$ also falls off toward zero. This arises due to the improvement in the temperature dependence of the order parameters $\bar{P}_2$ and $\bar{P}_4$ for the 216 molecule system compared to the 125 molecule system.

T / K	γ_1^{expt}	N	$\gamma_{1\,OT}^{inertia}$	$\gamma_{1\,OT}^{dipole}$	$\gamma_{1\,Wu}^{inertia}$	$\gamma_{1\,Wu}^{dipole}$
300	83.2±1.2[1]	125	825.7±47.2	283.4±28.1	257.5±9.9	150.6±11.2
		216	585.6±60.8	35.3±1.8	178.5±13.4	79.0±3.0
310	61.0±0.9[2]	125	2723.6±122.9	373.5±30.0	166.5±6.3	99.0±7.2
		216	448.6±20.3	67.1±0.5	99.0±4.1	53.1±0.4
320	32.6±0.5	125	2563.4±401.8	249.1±30.3	114.2±18.4	60.7±8.3
		216	237.6±23.2	35.2±1.4	45.0±5.0	25.5±1.2
330	-	125	2708.2±78.5	177.3±13.8	71.1±2.6	38.3±3.9
		216	120.4±13.0	22.5±1.4	25.0±3.6	15.1±1.3

Table 5.18: γ_1 calculated using the Osipov-Terentjev (5.33) and Wu-Wu (5.45) formulae for the 125 and 216 molecule systems and experimental values of γ_1. N indicates the number of molecules. All values of γ_1 are in mPa s. Notes: (1) T=303.5 K, (2) T=308 K.

T / K	γ_1^{expt}	$\gamma_1^{216\,inertia}$	$\gamma_1^{216\,dipole}$	$\gamma_1^{125\,inertia}$	$\gamma_1^{125\,dipole}$
300	83.2±1.2[1]	61.9±9.4	8.3±7.9	55.6±3.7	36.0±10.4
310	61.0±0.9[2]	47.5±5.2	13.4±0.1	148.7±4.1	39.6±9.9
320	32.6±0.5	33.7±18.9	8.5±8.8	108.0±15.9	24.7±20.0
330	-	18.9±28.1	5.3±18.4	104.8±3.7	16.6±15.3

Table 5.19: γ_1 calculated using the Nemtsov-Zakharov formula (5.34). γ_1^{expt} are the experimental values of γ_1, $\gamma_1^{216\,inertia}$ and $\gamma_1^{216\,dipole}$ are the values calculated from the 216 molecule system using the inertia tensor and dipole axis respectively, and $\gamma_1^{125\,inertia}$ and $\gamma_1^{125\,inertia}$ are calculated from the 125 molecule system. All γ_1 values in mPa s. Notes: (1) T=303.5 K, (2) T=308 K

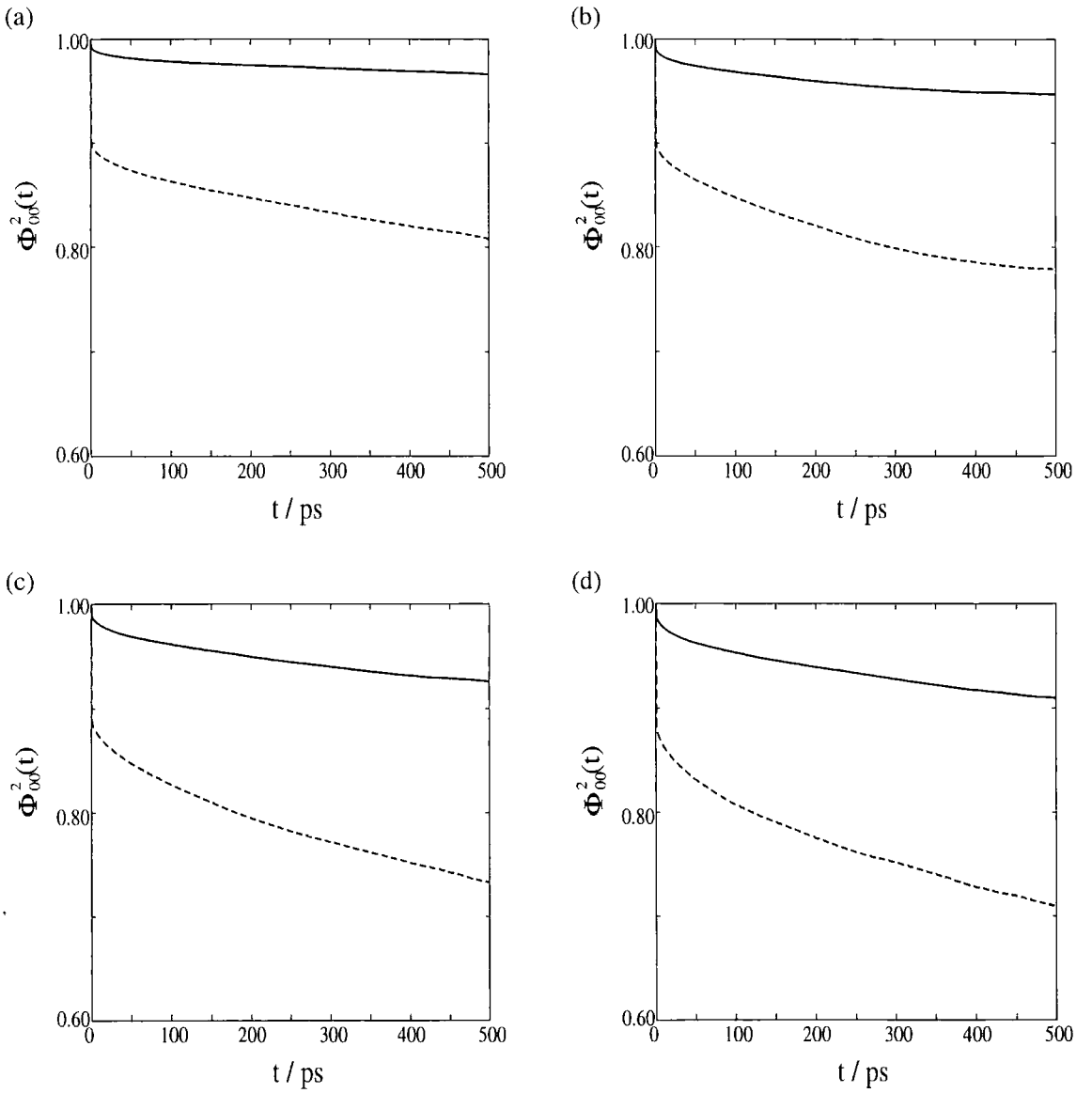

Figure 5.15: Orientational time correlation functions $\Phi^2_{00}(t)$ for PCH5 at (a) 300 K, (b) 310 K, (c) 320 K, and (d) 330 K. In all graphs the solid line denotes correlation functions found from the molecular long axis and the dashed line shows the correlation function obtained using the dipole axis.

T / K	γ_1^{expt}	$\gamma_1^{216\ inertia}$	$\gamma_1^{216\ dipole}$	$\gamma_1^{125\ inertia}$	$\gamma_1^{125\ dipole}$
300	83.2±1.2[1]	185.1±80.4	20.1±34.9	183.6±41.6	107.8±81.7
310	61.0±0.9[2]	139.8±40.1	33.8±0.3	498.3±43.7	120.0±82.0
320	32.6±0.5	85.0±106.5	18.2±30.3	362.4±202.3	74.8±163.2
330	-	44.4±134.3	10.6±56.5	352.1±42.6	49.2±120.9

Table 5.20: γ_1 calculated using the Fialkowski formula (5.35). γ_1^{expt} are the experimental values of γ_1, $\gamma_1^{216\ inertia}$ and $\gamma_1^{216\ dipole}$ are the values calculated from the 216 molecule system using the inertia tensor and dipole axis respectively, and $\gamma_1^{125\ inertia}$ and $\gamma_1^{125\ inertia}$ are calculated from the 125 molecule system. All γ_1 values in mPa s. Notes: (1) T=303.5 K, (2) T=308 K.

For most methods an increase in system size improves agreement between the simulated and experimental values of γ_1. For all the methods, including the DAVCF method where no improvement in the calculated values of γ_1 is seen, the larger system has smaller statistical errors. The largest changes in the values of γ_1 between the 125 and 216 molecule systems are in the values of γ_1 calculated using the rotational diffusion model. This arises due to their explicit dependence on the order parameters.

5.8 Conclusions

In this chapter the rotational viscosity coefficient γ_1 has been calculated for a typical nematic liquid crystal from atomistic computer simulation. A number of different methods have been used to calculate γ_1. The values of γ_1 calculated from these methods have been compared to each other and to experimental values. From the results presented in §5.6 and §5.7 the following conclusions may be made.

- The system densities calculated from simulation are in good agreement with

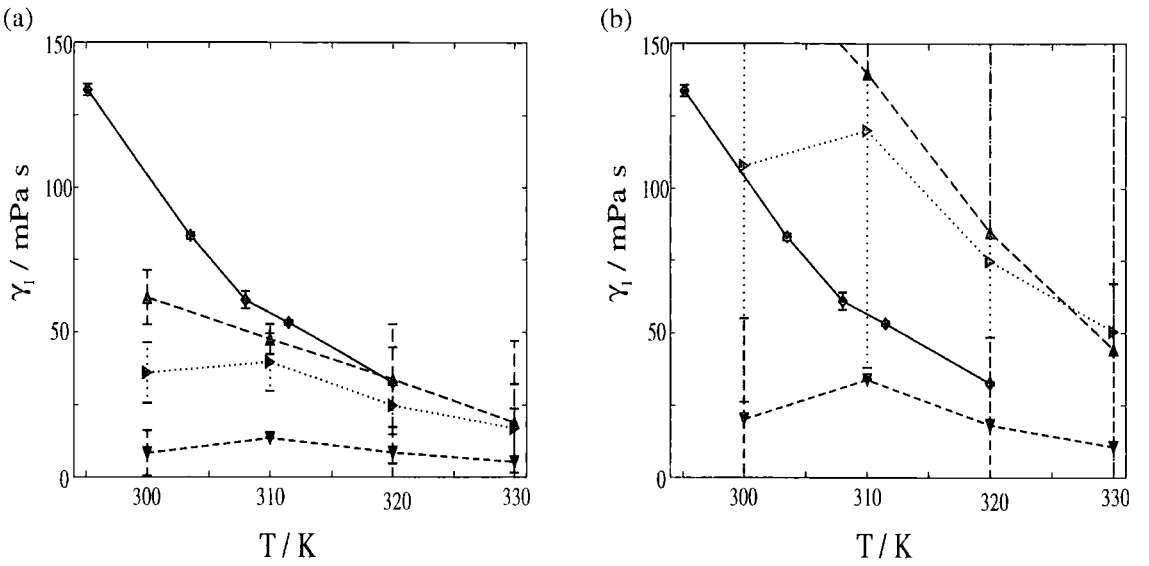

Figure 5.16: Comparison between γ_1 calculated using (a) the Nemtsov-Zakharov and (b) the Fialkowski formula and experimental values. In both graphs, the experimental data is marked by diamonds joined by solid line, the values calculated using the inertia tensor definition of the long axis for the 216 molecule system are marked by upright triangles joined by the dashed line, the values calculated using the dipole moment definition of the long axis for the 216 molecule system are marked by the downward facing arrows joined by the short dashed line and the vales calculated using the dipole moment definition of the molecular long axis for the 125 molecule system are marked by the left facing triangles joined by the dotted line.

experimental values.

- For the 125 molecule system the order parameter was poorly represented. This is not entirely surprising and has been observed in previous studies of small systems. The values of the order parameter and their temperature dependence improves when the system size is increased to 216 molecules.

- The large magnitude of the order parameter is not caused by the formation of smectic layers as shown in Fig. 5.6 (although it is highly improbable that a

system of 125 molecules would form smectic layers in a simulation).

- The value of the order parameters and hence some of the calculated values of γ_1 depend on the definition of the molecular axis.
- Both methods derived from linear response theory give calculated values of γ_1 broadly in line with experimental values.
- The director mean squared displacement method gives lower statistical errors than the director angular velocity correlation function method. This can be attributed to the larger amount of statistical noise on the angular velocity correlation function compared to the director mean-squared displacement.
- The Osipov-Terentjev formula performs poorly compared to the other methods. Values of γ_1 calculated using (5.33) are roughly an order of magnitude higher than other values. This arises due to the exponential dependence on $\bar{P}_2$ of (5.33). The empirical correction due to Wu and Wu gives much better values of γ_1, although the use of parameters fitted to experimental data for PCH5 reduces the predictive power of this method.
- The Nemtsov-Zakharov and Fialkowski formulae give values of γ_1 in better agreement with experimental values of γ_1 and those calculated using the two methods by Sarman and Evans, than those calculated using the Osipov-Terentjev formula.
- Values of γ_1 calculated for a larger system are generally in better agreement with experiment and have smaller uncertainties than those calculated in the smaller system. The improvement in the calculated values of γ_1 is most noticeable for the rotational diffusion methods. This is due to the lowering of the order parameters in the 216 molecule system.

There are a number of possible extensions to this work. The improvement in the values of the order parameters and calculated values of γ_1 suggest that the

system size dependence of γ_1 should be investigated. Atomistic studies of systems of the order of a thousand molecules have been performed recently and these have seen an improvement in the representation of long range order [106]. This should give a better representation of the temperature dependence of the order parameters (already seen for the 216 molecule system) which should improve the accuracy of the Nemtsov-Zakharov and Fialkowski approaches. An increase in system size should also improve the accuracy of the two linear-response approaches. These would also be improved by longer run lengths to improve the statistics. While run lengths for atomistic simulations are typically in the range of nanoseconds, increasing computing power, the increased use of parallel computers [238], and improvements to algorithms such as multiple time step methods [239] allow run lengths of the order of tens of nanoseconds.

Also desirable would be the investigation of alternative routes to γ_1 such as the non-equilibrium routes mentioned in §5.4. These have not been tested on many systems (the Manabe-Kuwajima method has only been used on the mesogen CCH4 and the shear flow method has only been used on Gay-Berne mesogens). However, as mentioned in §5.4, NEMD methods can be difficult to implement for atomistic models. Specifically in this case it can be difficult to constrain the director for flexible molecules.

Chapter 6

Calculation of the Flexoelectric Coefficients of a Nematic Liquid Crystal

6.1 Introduction

The *flexoelectric effect* was first discussed in 1969 [240] as a liquid crystal analogue to the piezoelectric effect[1]. Flexoelectricity is the generation of a spontaneous polarization in a liquid crystal due to a deformation of the director, or conversely, the deformation of the director due to an applied electric field.

Classically the flexoelectric effect arises from molecules with a shape asymmetry. The first cases to be considered were wedge and banana shaped molecules. Wedge shaped molecules with longitudinal dipoles show spontaneous polarization when splayed. Likewise banana shaped molecules with transverse dipoles exhibit spontaneous polarization under bend deformation. These cases are shown in Fig. 6.1.

[1] As pressure does not affect the nematic director and nematic liquid crystals are unable to maintain shear, piezoelectricity is not observed in nematic liquid crystals.

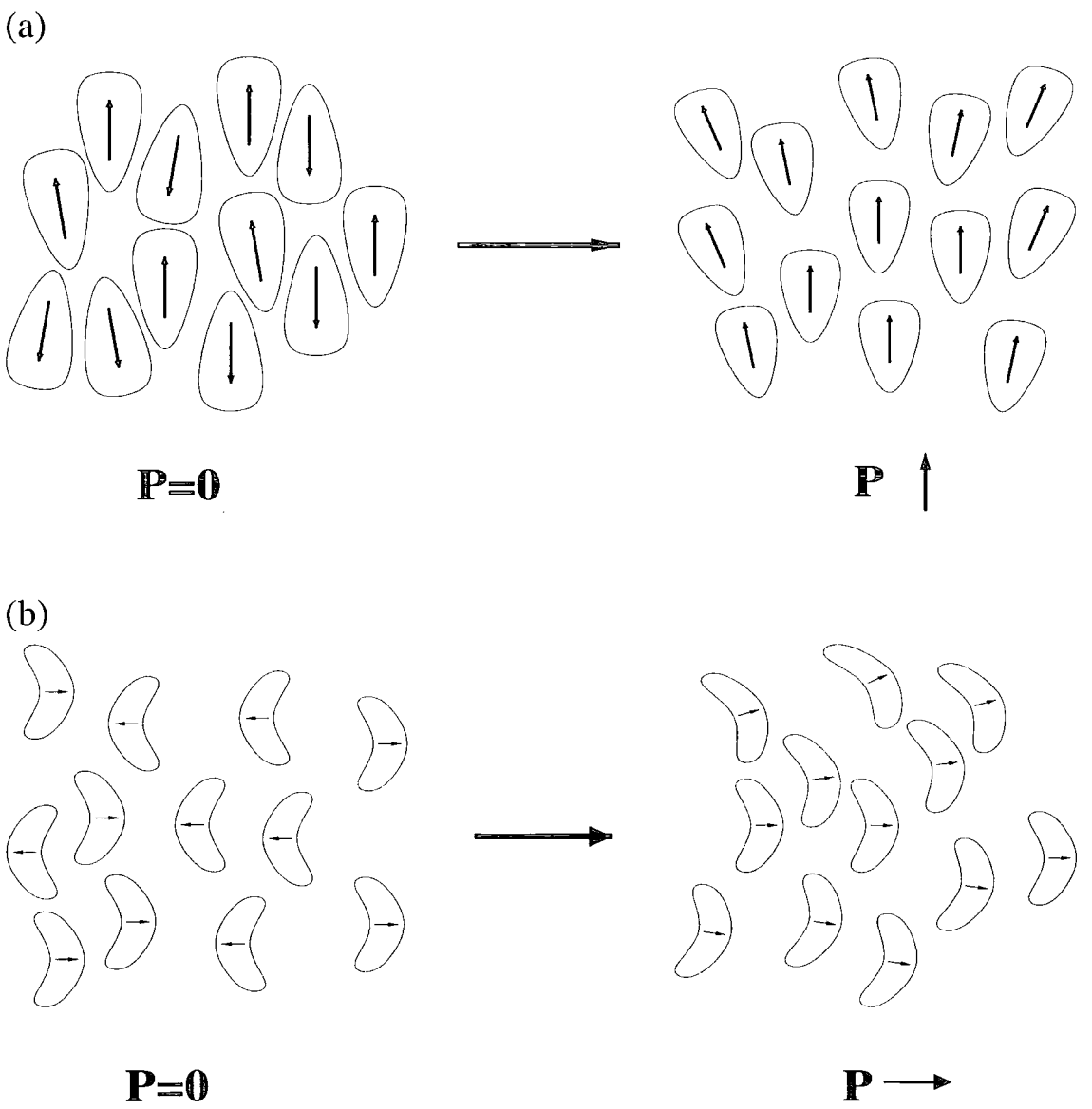

Figure 6.1: (a) Wedge shaped molecules with longitudinal dipole. (b) Banana shaped molecules with transverse dipole.

Prost and Marceau extended this analysis to more symmetric molecules with permanent quadrupole moments [241]. For quadrupolar molecules a polarization can occur from the gradient of the quadrupolar density. A simple physical picture of this can be seen in Fig. 6.2. In an undistorted state there is no bulk polarization. If the system is splayed, positive charges can enter a layer from above, while they are expelled below. This gives rise to a dipole, hence a spontaneous polarization.

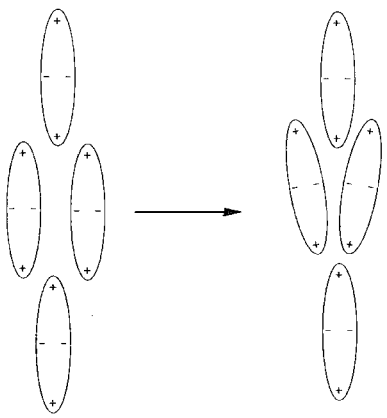

Figure 6.2: Splay deformation of a system of quadrupolar mesogens.

Flexoelectricity is also possible in symmetric polar liquid crystals such as 5CB and PCH5. In this case flexoelectricity arises from the effect that splay and bend deformations have on the local association between molecules. Polar liquid crystals tend to form dimers with anti-parallel alignment between the molecular dipoles [93,102,242]. When these are subjected to splay or bend deformations the alignment is no longer completely anti-parallel leading to a net polarization. This is shown in Fig. 6.3. This dimerization would also lead to the quadrupolar effect, at distance the anti-parallel dipoles would have a similar effect to a quadrupole.

In the above cases the polarization couples to a splay and/or bend deformation. It can be seen from symmetry arguments that the twist deformation cannot give rise to a polarization [243]. Thus a phenomenological formula for the flexoelectric

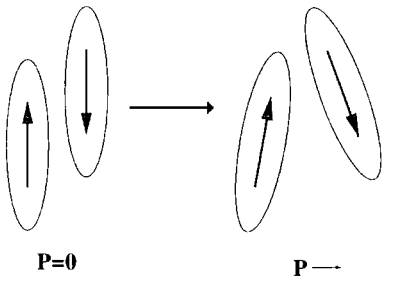

Figure 6.3: Microscopic mechanism for flexoelectricity in symmetric polar liquid crystals.

polarization can be written as

$$\mathbf{p}_f = e_s\mathbf{n}(\nabla.\mathbf{n}) + e_b\mathbf{n} \times \nabla \times \mathbf{n} \tag{6.1}$$

where e_s and e_b are the splay and bend flexoelectric coefficients, and $\mathbf{n}(\nabla.\mathbf{n})$ and $\mathbf{n} \times \nabla \times \mathbf{n}$ are the splay and bend vectors respectively. In addition to this direct flexoelectric effect, there is also a converse effect where an applied field can deform the director [240].

The flexoelectric effect has a large influence on many phenomena in liquid crystals [244]. Technologically it plays a key role in some novel device applications. Flexoelectric surface switching is important in newly developed bistable displays [245, 246]. Flexoelectric coupling in chiral and twisted nematic crystals [247] leads to a linear rotation of the optic axis and also leads to device applications . Flexoelectric coupling in smectic liquid crystals has been shown to stabilize helical structures [248].The flexoelectric effect is also present in lipid membranes [249]. The direct link between molecular structure and the flexoelectric effect also makes it of fundamental interest.

There have been many experimental studies of the flexoelectric effect [250, 251] and some experimental techniques for determining the flexoelectric coefficients are outlined in §6.2. However, e_s and e_b are difficult to determine from experiment for a number of reasons. Firstly the response of liquid crystals to applied fields is dominated by the dielectric response for all but the smallest fields. Secondly

the flexoelectric coefficients are not measured directly; generally $(e_s + e_b)/k_{22}$ and $|e_s - e_b|/k_{33}$ are measured. Alongside experimental studies, several theoretical studies have also been performed [252–259]. A number of different approaches were used. An Onsager-like theory [252], a mean-field theory (including attractive and repulsive interactions) [253], and density functional theories [256,257] have all been developed. By necessity numerical results from these theories have only been determined for simple models of liquid crystals. Recently more sophisticated theoretical studies have attempted to calculate the flexoelectric coefficients using more realistic models of liquid crystals [258] or to take the effect of intermolecular interactions into account [259],

Despite the difficulties in experimental or theoretical approaches only two previous simulation studies of the flexoelectric effect have been performed [76–78]. These both used simple models and are outlined in §6.3.

6.2 Experimental Determination of e_s and e_b

A number of techniques for determining e_s and e_b have been proposed [251], both by determining e_s and e_b directly from a spontaneous polarization arising from a deformed director field, or indirectly by measuring distortions to the director in an applied field.

Direct measurements are less common than converse measurements. One direct method is to apply periodic pressure [260] or heat pulses [261, 262] to a nematic cell. Pressure pulses are usually produced using a loudspeaker, while heat pulses are produced by short pulses from a laser.

There are a number of methods for determining e_s and e_b from the converse flexoelectric effect, i.e. director deformation in an applied field. Some of these involve surface torques. These however are complicated due to the unknown nature of the anchoring [251]. Measurements of the flexoelectric coefficients from bulk

torques are more accurate. The application of a field to an unbound nematic leads to the formation of a periodic domain structure [240]. The period of these domains can be used to calculate $e_s + e_b$ [263]. Another, more common method is to apply a field across a hybrid aligned cell [264–266]. Measurement of the twist angle allows the determination of $e_s + e_b$. $e_s - e_b$ can be determined using two experiments. The value can be determined using an inhomogenous field produced by electrodes on a glass substrate [267] (cf. Fig. 3 in [250]). The sign can be found by applying a field across a wedge shape cell [250].

6.3 Simulation Studies of the Flexoelectric Effect

Previous simulation studies of the flexoelectric effect have focused on a simple molecular model, a wedge shaped molecule formed by fusing a Gay-Berne molecule with a Lennard-Jones sphere, shown in Fig. 6.4. The aim of these have been to study the relationship between the flexoelectric properties and molecular shape, and so, have consequently, neglected issues such as molecular flexibility or long range dipole-dipole interactions.

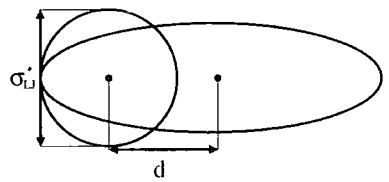

Figure 6.4: Wedge formed by fusing Gay-Berne and Lennard-Jones particles. d is the distance between the centres of the Lennard-Jones and Gay-Berne units and σ^*_{LJ} is the diameter of the Lennard-Jones unit.

The first study [76,77] calculated e_s and e_b, as well as the elastic constants, for a range of temperatures (and order parameters) across the nematic range of the model for two different values of the steric dipole p^*

$$p^* = \left(\frac{4\pi}{3}\right) \epsilon^*_{LJ} \sigma^*_{LJ} d^*, \tag{6.2}$$

where σ^*_{LJ} and ϵ^*_{LJ} are the Lennard-Jones width and well depth respectively, and d^* is the distance from the centre of the Gay-Berne unit to the centre of the Lennard-Jones sphere. e_s and e_b were calculated from the direct correlation function $c(\mathbf{r}_{ij}, \mathbf{u}_i, \mathbf{u}_j)$ [132]

$$e_s = \rho^2 p \int d\mathbf{r}_{ij} d\mathbf{u}_i d\mathbf{u}_j f(\mathbf{u}_i) f'(\mathbf{u}_j) c(\mathbf{r}_{ij}, \mathbf{u}_i, \mathbf{u}_j) u_{iz} u_{jx} r_{ijx} \tag{6.3}$$

$$e_b = \rho^2 p \int d\mathbf{r}_{ij} d\mathbf{u}_i d\mathbf{u}_j f(\mathbf{u}_i) f'(\mathbf{u}_j) c(\mathbf{r}_{ij}, \mathbf{u}_i, \mathbf{u}_j) u_{ix} u_{jx} r_{ijz} \tag{6.4}$$

where p is the molecular dipole, $f(\mathbf{u})$ is the single particle orientational distribution function and $f'(\mathbf{u})$ is its derivative with respect to $\mathbf{u}$, $\mathbf{u}_i$ is the molecular orientation, and $\mathbf{r}_{ij}$ is the intermolecular vector. The direct correlation function $c(\mathbf{r}_{ij}, \mathbf{u}_i, \mathbf{u}_j)$ was determined iteratively from the pair distribution function [268]. The bend coefficient was found to be negligible, in line with Meyer's predictions based on molecular shape [240], while the splay coefficient was found to be significant in the nematic phase and negligible in the isotropic liquid.

The iterative method used to find $c(\mathbf{r}_{ij}, \mathbf{u}_i, \mathbf{u}_j)$ neglects the director dependence in $c(\mathbf{r}_{ij}, \mathbf{u}_i, \mathbf{u}_j)$. Studies of the elastic constants using this method [269–271] have given poor results relative to other methods [272]. Recently a method for calculating the direct correlation function from simulation has been presented and used for the calculation of the nematic elastic constants [273].

The second study [78] calculated e_s and e_b using a linear response formalism [255] that relates the flexoelectric coefficients to correlation functions of the polarization and the orientational stress together with the fluctuation-dissipation theorem [274]. The simulations were performed on two systems of wedge shaped molecules, with different degrees of asymmetry, this time on the smectic phase and in the isotropic phase. Comparison was also made with a system of symmetric Gay-Berne particles. The molecules considered were less symmetric than in [76, 77] which explains the lack of a nematic phase. Again the bend coefficient was found to be small compared to the splay coefficient, with both coefficients negligible in the isotropic phase. The splay coefficient was also seen to change sign with decreasing shape asymmetry. This

was due to different packing arrangements, the larger edges tilted away from each other for the less symmetric molecules.

Comparison between these studies is difficult due to differences in the models and state points considered. While both studies found e_b to be negligible, there is a difference of about an order of magnitude between e_s. The most direct comparison possible is between the more symmetric molecules in each study ($p^* = 0.524$ in [76, 77] and $p^* = 0.565$ in [78]). The computed e_s are shown in Tab. 6.1. As well as the order of magnitude difference between the two results, there is also a sign difference. This difference is likely to be due to differences between the two methods employed in these studies; the temperatures and steric dipoles are similar and flexoelectric coefficients are similar in the nematic and smectic phases [275].

p^*	T^*	e_s^*	Ref.
0.524	2.95	0.13±0.01	[76]
0.565	2.90	-2.08±0.21	[78]

Table 6.1: Comparison between simulated values of e_s for simple wedge shaped molecules. All values are in reduced units, where $T^* = (k_B/\epsilon)T$, and $e_s^* = (\sigma^2/\epsilon)e_s$ and ϵ and σ are the energy and length units of the Gay-Berne units.

6.4 Theory

Here we outline the method used for the calculation of the flexoelectric coefficients. From the discussion in §6.3 previous methods give markedly different values for the flexoelectric coefficients. While the two methods used are formally equivalent [255], significant approximations for the direct correlation function were made in the density functional method. In comparison the linear response is relatively straightforward to implement.

Linear-response relations for the flexoelectric coefficients e_s and e_b were initially derived by Osipov and Nemtsov [255]. They have since been re-derived by Allen and Masters [276] using thermodynamic perturbation theory [132].

The change in a variable B caused by a perturbation H_1 is [222]

$$\langle B(t)\rangle_\lambda = \langle B(0)\rangle - \int_0^\infty dt'\, \lambda \langle B(t')H_1(0)\rangle F_e(t'). \tag{6.5}$$

In the case of the flexoelectric effect, $F_e(t')$ is the orientational stress, given by

$$\gamma_{\alpha\beta} = \epsilon_{\alpha\mu\nu} n_\mu \partial_\beta n_\nu \tag{6.6}$$

where $\partial_\beta n_\nu = \frac{\partial n_\nu}{\partial r_\beta}$. The perturbation is given by the static orientational stress tensor [78] $\Pi_{\alpha\beta}$. An explicit form for this can be found as follows [276]. A small change in the angular coordinates θ_i can be written as

$$\theta_{i\beta} = \theta_{i0\beta} + r_{i\alpha}\gamma_{\alpha\beta} \tag{6.7}$$

where $\mathbf{r}_i$ is the position vector of molecule i. The corresponding stress for this deformation is

$$\Pi_{\alpha\beta} = \sum_i r_{i\alpha} \frac{\partial V}{\partial \theta_{i\beta}} \tag{6.8}$$

$$= -\sum_i r_{i\alpha}\tau_{i\beta}, \tag{6.9}$$

where V is the potential and τ_i is the torque on molecule i ($\tau_i = -\frac{\partial V}{\partial \theta_i}$). Rewriting this gives

$$\Pi_{\alpha\beta} = -\sum_i \sum_{j\neq i} r_{i\alpha}\tau_{ij\beta} \tag{6.10}$$

$$= -\frac{1}{2}\sum_i \sum_{j\neq i} r_{i\alpha}\tau_{ij\beta} + r_{j\alpha}\tau_{ji\beta} \tag{6.11}$$

$$= -\frac{1}{2}\sum_i \sum_{j\neq i} r_{ij\alpha}\tau_{ij\beta} + r_{j\alpha}(\tau_{ij\beta} + \tau_{ji\beta}) \tag{6.12}$$

(6.12) follows as $\mathbf{r}_i = \mathbf{r}_j + \mathbf{r}_{ij}$. On ensemble averaging the second term in (6.12) disappears so finally

$$\Pi_{\alpha\beta} = -\frac{1}{2}\sum_i \sum_{j\neq i} r_{ij\alpha}\tau_{ij\beta}. \tag{6.13}$$

Inserting these into (6.5) and taking the flexoelectric polarization $\mathbf{p}^f$ to be $\mathbf{p}-\mathbf{p}_{eq}$ gives

$$\langle p_\alpha^f \rangle = -\int_0^\infty dt' \ \langle p_\alpha(t')\Pi_{\beta\gamma}(0)\rangle \, \gamma_{\beta\gamma}(t'). \tag{6.14}$$

If the distortion is taken to be periodic with frequency ω

$$\langle p_\alpha^f \rangle = -\int_0^\infty dt' \ \langle p_\alpha(t')\Pi_{\beta\gamma}(0)\rangle \, \gamma_{\beta\gamma} \exp(i\omega t'). \tag{6.15}$$

Integrating by parts and taking the limit $\omega \to 0$ gives

$$\langle p_\alpha^f \rangle = E_{\alpha\eta\gamma}\gamma_{\beta\gamma}, \tag{6.16}$$

where $E_{\alpha\beta\gamma}$ is the response function given by

$$E_{\alpha\beta\gamma} = -\frac{\beta}{V}\langle p_\alpha(0)\Pi_{\beta\gamma}(0)\rangle . \tag{6.17}$$

To find e_s and e_b in terms of the components of $E_{\alpha\beta\gamma}$ it is necessary to write $E_{\alpha\beta\gamma}$ as

$$E_{\alpha\beta\gamma} = E_1\epsilon_{\alpha\beta\gamma} + E_2\epsilon_{\lambda\alpha\beta}n_\lambda n_\gamma + E_3\epsilon_{\lambda\gamma\beta}n_\lambda n_\alpha + E_4\epsilon_{\lambda\alpha\gamma}n_\lambda n_\beta. \tag{6.18}$$

This is the most general form for a third rank pseudotensor consisting of the director components and the Levi-Civita tensor. When multiplied by the distortion tensor, the first term on the right hand side of (6.18) gives

$$\begin{aligned} E_1\epsilon_{\alpha\beta\gamma}\epsilon_{\beta\mu\nu}n_\mu\partial_\gamma n_\nu &= E_1\left(\delta_{\gamma\mu}\delta_{\alpha\nu} - \delta_{\gamma\nu}\delta_{\alpha\mu}\right)n_\mu\partial_\gamma n_\nu \\ &= -E_1 n_\alpha\partial_\gamma n_\gamma + E_1 n_\gamma\partial_\gamma n_\alpha. \end{aligned} \tag{6.19}$$

Similarly

$$\begin{aligned} E_2\epsilon_{\lambda\alpha\beta}n_\lambda n_\gamma\epsilon_{\beta\mu\nu}n_\mu\partial_\gamma n_\nu &= E_2\left(\delta_{\lambda\mu}\delta_{\alpha\nu} - \delta_{\lambda\nu}\delta_{\alpha\mu}\right)n_\gamma n_\lambda n_\mu\partial_\gamma n_\nu \\ &= E_2 n_\gamma\partial_\gamma n_\alpha - E_2 n_\lambda n_\gamma n_\alpha\partial_\gamma n_\lambda \\ &= E_2 n_\gamma\partial_\gamma n_\alpha, \end{aligned} \tag{6.20}$$

$$\begin{aligned} E_3\epsilon_{\lambda\gamma\beta}n_\lambda n_\alpha\epsilon_{\beta\mu\nu}n_\mu\partial_\gamma n_\nu &= E_3\left(\delta_{\lambda\mu}\delta_{\gamma\nu} - \delta_{\lambda\nu}\delta_{\gamma\mu}\right)n_\alpha n_\lambda n_\mu\partial_\gamma n_\nu \\ &= E_3 n_\alpha\partial_\gamma n_\gamma - E_3 n_\alpha n_\gamma n_\nu\partial_\gamma n_\nu \\ &= E_3 n_\alpha\partial_\gamma n_\gamma, \end{aligned} \tag{6.21}$$

and

$$\begin{aligned} E_4\epsilon_{\lambda\alpha\gamma}n_\lambda n_\beta\epsilon_{\beta\mu\nu}n_\mu\partial_\gamma n_\nu &= E_4\left(\delta_{\lambda\beta}\delta_{\alpha\mu}\delta_{\gamma\nu}+\delta_{\lambda\mu}\delta_{\alpha\nu}\delta_{\gamma\beta}+\delta_{\lambda\nu}\delta_{\alpha\beta}\delta_{\gamma\mu}-\delta_{\lambda\mu}\delta_{\alpha\beta}\delta_{\gamma\nu}\right. \\ &\quad \left.-\delta_{\lambda\nu}\delta_{\alpha\mu}\delta_{\gamma\beta}-\delta_{\lambda\beta}\delta_{\alpha\nu}\delta_{\gamma\mu}\right)n_\beta n_\lambda n_\mu\partial_\gamma n_\nu \\ &= E_4 n_\alpha\partial_\gamma n_\gamma + E_4 n_\gamma\partial_\gamma n_\alpha + E_4 n_\alpha n_\gamma n_{nu}\partial_\gamma n_\nu - E_4 n_\alpha\partial_\gamma n_\gamma \\ &\quad -E_4 n_\gamma\partial_\gamma n_\alpha - E_4 n_\alpha n_\gamma n_\nu\partial_\gamma n_\nu \\ &= 0. \end{aligned} \tag{6.22}$$

Thus

$$E_{\alpha\beta\gamma}\gamma_{\beta\gamma} = (E_3 - E_1)n_\alpha\partial_\gamma n_\gamma + (E_1 + E_2)n_\gamma\partial_\gamma n_\alpha. \tag{6.23}$$

Noting that

$$\left[\mathbf{n}(\nabla\mathbf{n})\right]_\alpha = n_\alpha\partial_\gamma n_\gamma \tag{6.24}$$

$$\left[\mathbf{n}\times\nabla\times\mathbf{n}\right]_\alpha = -n_\gamma\partial_\gamma n_\alpha \tag{6.25}$$

then (6.23) is identical to (6.1) if $e_s = E_3 - E_1$ and $e_b = -(E_1 + E_2)$. Expressions for e_s and e_b in terms of $E_{\alpha\beta\gamma}$ can be found from (6.18). An expression for e_s can be found by multiplying (6.18) by $\epsilon_{\mu\beta\gamma}n_\mu n_\alpha$ giving

$$\begin{aligned} E_{\alpha\beta\gamma}\epsilon_{\mu\beta\gamma}n_\mu n_\alpha &= E_1\epsilon_{\alpha\beta\gamma}\epsilon_{\mu\beta\gamma}n_\mu n_\alpha + E_2\epsilon_{\lambda\alpha\beta}\epsilon_{\mu\beta\gamma}n_\alpha n_\gamma n_\lambda n_\mu + E_3\epsilon_{\lambda\gamma\beta}\epsilon_{\mu\beta\gamma}n_\alpha n_\lambda n_\mu n_\alpha \\ &\quad +E_4\epsilon_{\lambda\alpha\gamma}\epsilon_{\mu\beta\gamma}n_\alpha n_\beta n_\lambda n_\mu \\ &= 2E_1\delta_{\alpha\mu}n_\alpha n_\mu + E_2\left[\delta_{\lambda\gamma}\delta_{\alpha\mu}-\delta_{\lambda\mu}\delta_{\alpha\gamma}\right]n_\alpha n_\gamma n_\mu n_\lambda - 2E_3\delta_{\lambda\mu}n_\mu n_\lambda \\ &\quad E_4\left[\delta_{\lambda\mu}\delta_{\alpha\beta}-\delta_{\lambda\beta}\delta_{\alpha\mu}\right]n_\alpha n_\gamma n_\mu n_\lambda \\ &= 2E_1 - 2E_3. \end{aligned} \tag{6.26}$$

Thus

$$e_s = -\frac{1}{2}E_{\alpha\beta\gamma}\epsilon_{\mu\beta\gamma}n_\mu n_\alpha. \tag{6.27}$$

Similarly an expression for e_b can be found by multiplying (6.18) by $\epsilon_{\mu\alpha\beta}n_\mu n_\gamma$

$$E_{\alpha\beta\gamma}\epsilon_{\mu\alpha\beta}n_\mu n_\gamma = E_1\epsilon_{\alpha\beta\gamma}\epsilon_{\mu\alpha\beta} + E_2\epsilon_{\lambda\alpha\beta}\epsilon_{\mu\alpha\beta}n_\gamma n_\lambda n_\gamma n_\mu + E_3\epsilon_{\lambda\gamma\beta}\epsilon_{\mu\alpha\beta}n_\gamma n_\mu n_\lambda n_\alpha$$

$$
\begin{aligned}
& +E_4\epsilon_{\lambda\alpha\gamma}\epsilon_{\mu\alpha\beta}n_\beta n_\gamma n_\lambda n_\mu \\
= \; & 2E_1\delta_{\mu\gamma}n_\mu n_\gamma + 2E_2\epsilon_{\lambda\alpha\beta}\epsilon_{\mu\alpha\beta}n_\lambda n_\mu + E_3\left[\delta_{\lambda\mu}\delta_{\gamma\alpha} - \delta_{\lambda\alpha}\delta_{\gamma\mu}\right]n_\alpha n_\gamma n_\lambda n_\mu \\
& +E_4\left[\delta_{\lambda\mu}\delta_{\gamma\beta} - \delta_{\lambda\beta}\delta_{\gamma\mu}\right]n_\beta n_\gamma n_\lambda n_\mu \\
= \; & 2E_1 + 2E_2. \qquad (6.28)
\end{aligned}
$$

So

$$e_b = -\frac{1}{2}E_{\alpha\beta\gamma}\epsilon_{\mu\alpha\beta}n_\mu n_\gamma. \qquad (6.29)$$

For simulations it is convenient to consider these in a director fixed frame. If the $\mathbf{n} = \hat{\mathbf{z}}$ then (6.27) and (6.29) reduce to [276]

$$e_s = -\frac{1}{2}\left[E_{zxy} - E_{zyx}\right] \qquad (6.30)$$

$$e_b = -\frac{1}{2}\left[E_{xyz} - E_{yxz}\right]. \qquad (6.31)$$

6.5 Computational Method

6.5.1 Simulation Model and Methodology

PCH5 molecules (Fig. 5.5) were represented using a harmonic all-atom force field (4.16) of the AMBER form [143]. The force field parameters were taken from the work presented in chapter 4 and are shown in Tables 4.3, 4.4, 4.6, and 4.9.

The molecular dynamics simulations were performed using the DL_POLY program version 2.12 [167]. The equations of motion were integrated using the leapfrog algorithm with a time step of 2 fs. Bond lengths were constrained using the SHAKE algorithm [117]. Simulations were performed in the NpT ensemble using the Nosé-Hoover thermostat and barostat [122–124] with relaxation times of 1 ps and 4 ps respectively. Long range electrostatic interactions were evaluated using an Ewald sum with a convergence parameter of 0.24 Å^{-1} and 11 wave-vectors in the x, y, and z directions. The pressure was set to 1 atmosphere.

The simulations were started from a cubic system of 216 molecules at a gas phase density. The initial state was a highly ordered nematic ($\bar{P}_2 \approx 0.9$) with antiferroelectric ordering. This was then rapidly compressed to a liquid state density (about 500-1000 kg m^{-3}). An equilibration run of about 1 ns was then performed after which statistics were then gathered over 4 ns at each temperature (300K, 310 K, 320K, and 330K). Coordinate data for the calculation of the flexoelectric coefficients was saved every 500 time steps (1 ps).

6.5.2 Calculation of e_s and e_b

This section describes in detail the procedure for calculating the flexoelectric coefficients from the simulation data.

The response function $E_{\alpha\beta\gamma}$ was calculated for each set of saved coordinate data. The polarization $\mathbf{p}$ was calculated from the atomic charges and positions

$$\mathbf{p} = \sum_i q_i \mathbf{r}_i, \tag{6.32}$$

where q_i are the atomic charges and $\mathbf{r}_i$ are the atomic position vectors. The sum in (6.32) runs over all the atoms in the simulation.

The orientational stress tensor is calculated from the torques and centre of mass positions of the molecules. The torque on molecule i from molecule j, τ_{ij}, is found from

$$\tau_{ij} = \sum_k \mathbf{r}_k^c \times \mathbf{F}_{kj}, \tag{6.33}$$

where $\mathbf{r}_k^c$ is the position vector of atom k in i relative to the centre of mass of molecule i, $\mathbf{F}_{kj}$ is the force on k from molecule j and the sum runs over all atoms in i. $\mathbf{F}_{kj}$ is given by

$$\mathbf{F}_{kj} = \sum_l \mathbf{F}_{lk}, \tag{6.34}$$

where $\mathbf{F}_{lk}$ is the force on atom k from atom l in molecule j and the sum runs over all the atoms in molecule j. The force between two atoms is the sum of the

van der Waals force and the electrostatic force. The Van der Waals force is of the Lennard-Jones form

$$\mathbf{F}_{kl}^{vdw} = -24\epsilon_{kl}\left[\frac{2\sigma_{kl}^{12}}{r_{kl}^{13}} - \frac{\sigma_{kl}^{6}}{r_{kl}^{7}}\right]\hat{\mathbf{r}}_{kl}, \tag{6.35}$$

where ϵ_{kl} and σ_{kl} are the usual Van der Waals parameters and $\hat{\mathbf{r}}_{\mathbf{kl}}$ is the unit vector along the direction between k and l. As the Van der Waals interaction is short ranged this is only evaluated for pairs of atoms less than 12 Å apart, in common with the forces calculated in the simulation.

The electrostatic force was evaluated using Coulomb's law

$$\mathbf{F}_{kl}^{elec} = -\frac{1}{4\pi\epsilon_0}\frac{q_k q_l}{r_{kl}^2}\hat{\mathbf{r}}_{kl}. \tag{6.36}$$

Due to the long-range of the electrostatic interaction this is calculated for all pairs of atoms in the system (or their minimum image separations). For our system containing 9504 atoms there are approximately 45 million atom pairs so this is a large computational task.

6.6 Results

6.6.1 Density

Simulation volumes and calculated densities are shown in Tab. 6.2. As can be seen there is good agreement between calculated densities and the experimental values [235].

6.6.2 Order Parameter

Shown in Tab. 6.3 are the values of the order parameter $\bar{P}_2$ calculated from simulation. As before these were calculated using two different methods. The first used the molecule long axis found by diagonalizing the inertia tensor, (3.52), and the second using the molecular dipole axis. Also shown are the order parameters

T / K	V / Å^3	$\langle\rho\rangle$ / kg m^{-3}	ρ_{expt} / kg m^{-3}
300	92468±688	997.5±7.4	963.0
310	92912±745	992.9±8.0	956.5
320	94033±777	981.1±8.1	949.6
330	94824±761	972.9±10.0	-

Table 6.2: Computed densities for simulation PCH5

found from Raman scattering [236]. As can be seen the simulated order parameters found from the inertia tensor are higher than the experimental values at all temperatures, although they are significantly lower than those calculated for the 125 molecule system studied previously (Tab. 5.5). The order parameters found from the dipole moment are significantly lower than those found from the inertia tensor (as for the 125 molecule case) as well as being lower than the Raman scattering results for temperatures below T_{NI}^{expt}.

T / K	$\bar{P}_2^{inertia}$	$\bar{P}_2^{dipole}$	$\bar{P}_2^{expt}$
300	0.68±0.02	0.45±0.01	0.63
310	0.65±0.01	0.47±0.00	0.58
320	0.55±0.03	0.39±0.01	0.50
330	0.51±0.04	0.36±0.02	0.00

Table 6.3: Orientational order parameter $\bar{P}_2$ of PCH5 calculated from simulation.

The translational order of the system can be studied through the centre of mass radial distribution function $g(r)$ and the RDF resolved parallel to the director $g_{\parallel}(r)$. These are shown in Fig. 6.5. As can be seen the RDF shows a first solvation peak at approximately 6 Å. $g_{\parallel}(r)$ remains flat showing no periodic ordering of molecules, indicating a nematic phase.

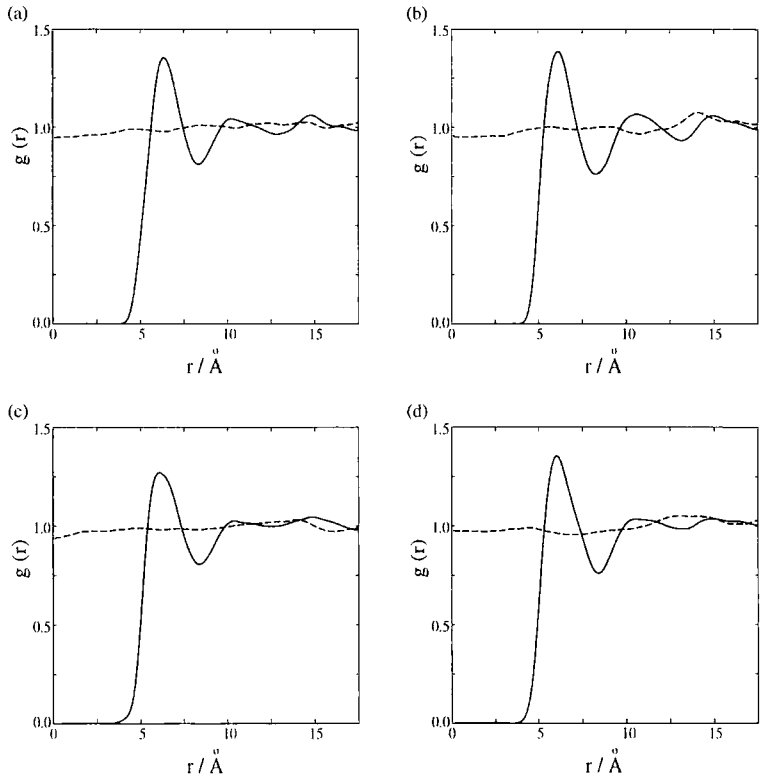

Figure 6.5: Radial distribution functions for simulated PCH5 at (a) 300 K, (b) 310 K, (c) 320 K, and (d) 330 K. The solid line shows the radial distribution function and the dashed line shows the radial distribution function resolved parallel to the director.

6.6.3 Molecular Structure

Shown in Fig. 6.6 are the dihedral distribution functions for some of the dihedrals in the alkyl tail, as shown in Fig. 5.5. These have an important effect on the overall shape of the molecule. The percentage of dihedrals in the *trans* and *gauche* states can be calculated by integrating over these distributions and these are shown in Tab. 6.4. The *gauche* populations increase with temperature as would be expected. The largest *gauche* populations occur for the γ dihedral. This is consistent with previous studies [83,99] and predictions of mean field theory [277]. States where the tail is linear, such as the all *trans* state and states with γ in a *gauche* state and β

and δ *trans*, are of lower energy (and hence of higher probability) than states where the tail is non-linear. The *trans* populations in the alkyl tail are larger than those for organic liquids such as butane or hexane studied in chapter 4. As butane and hexane are isotropic liquids the dihedral populations are not subject to an ordering mean-field.

(a) β

T / K	*trans*	*gauche-*	*gauche+*
300	97.5 %	1.2 %	1.3 %
310	97.7 %	1.2 %	1.1 %
320	95.5 %	2.3 %	2.2 %
330	95.4 %	2.0 %	2.6 %

(b) γ

T / K	*trans*	*gauche-*	*gauche+*
300	85.3 %	7.4 %	7.3 %
310	85.5 %	7.2 %	7.3 %
320	81.8 %	8.9 %	9.3 %
330	79.9 %	10.1 %	10.0 %

(c) δ

T / K	*trans*	*gauche-*	*gauche+*
300	86.7 %	6.7 %	6.6 %
310	86.4 %	6.9 %	6.7 %
320	85.3 %	7.2 %	7.5 %
330	84.5 %	7.6 %	7.9 %

Table 6.4: Dihedral angle populations for simulated PCH5. (a) dihedral angle β, (b) dihedral angle γ, and (c) dihedral angle δ.

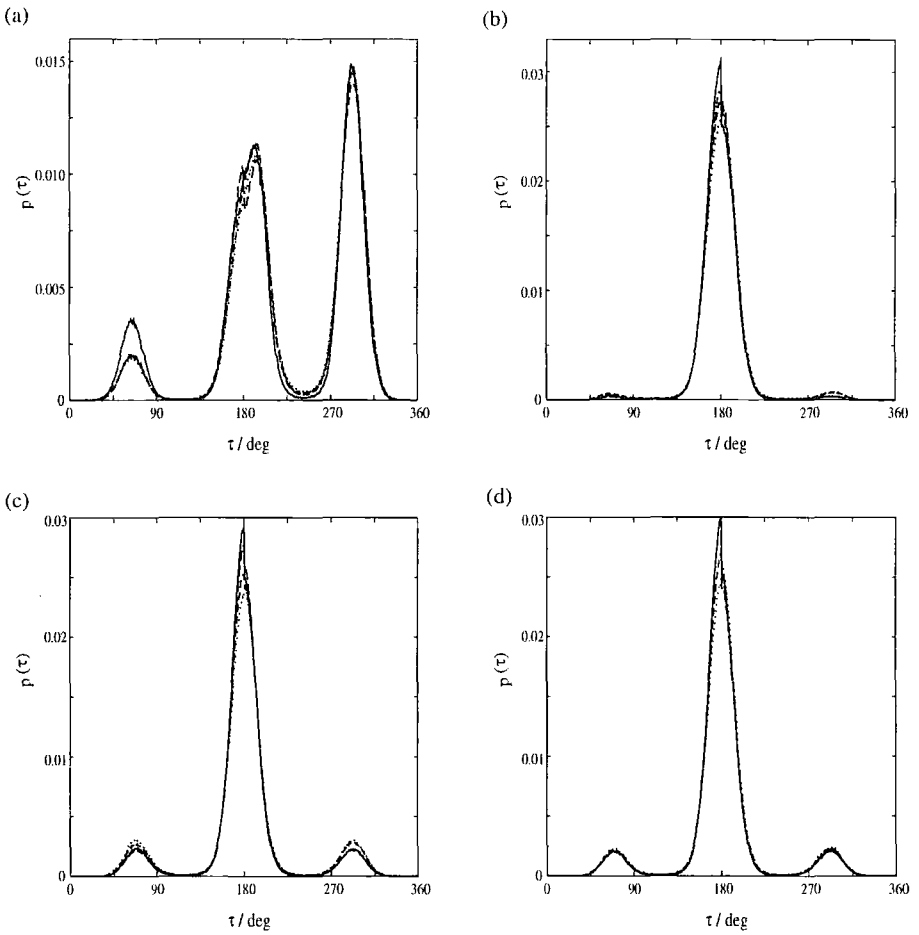

Figure 6.6: Dihedral angle distribution functions for the alkyl tail of PCH5. In each graph the solid line indicates the data for 300 K, the long dashed line indicates the data at 310 K, the short dashed line indicates the data at 320 K, and the dotted line shows the data at 330 K.

The molecular shape can also be approximately characterized by the equivalent inertia spheroid [83]. This is a spheroid with an uniform mass density and the same total mass, M, as the molecule. The dimensions of this give an approximate measure of molecular length, breadth, and width. These are found from the principal moments of inertia I_{aa}, I_{bb}, and I_{cc}, i.e. the eigenvalues of the inertia tensor (3.52). The lengths of each of the axes $2a$, $2b$, and $2c$ are given by

$$\begin{aligned} a &= \sqrt{\frac{2.5(I_{bb}+I_{cc}-I_{aa})}{M}} \\ b &= \sqrt{\frac{2.5(I_{cc}+I_{aa}-I_{bb})}{M}} \\ c &= \sqrt{\frac{2.5(I_{aa}+I_{bb}-I_{cc})}{M}}. \end{aligned} \tag{6.37}$$

Shown in Tab. 6.5 are the principal moments of inertia and the equivalent axes lengths for simulated PCH5. The molecular length ($2a$) shows a slight decrease with temperature, while the molecular breadth and width show a slight increase. This is expected from the dihedral angle distributions and shows that the molecule becomes longer and thinner as the system goes further into the nematic phase. This is in accordance with mean-field theory as discussed above. The ratio between c and b is roughly 0.71 across the temperature range studied. These results are similar to those obtained in a previous atomistic simulation of CCH5 [82, 83] where there was a slight change in the axis lengths with temperature within the nematic phase and a larger change on going into the isotropic phase.

6.6.4 Polarization

The polarization was calculated from the atomic charges and positions using (6.32) for each set of coordinate data and the average polarizations are shown in Tab. 6.6. The time evolution of the polarization at each temperature is shown in Fig. 6.7. As can be seen at each temperature there is a small net polarization, particularly directed along the director. This is a consequence of the finite system size and short

T / K	I_{aa}	I_{aa}	I_{aa}	$2a$	$2b$	$2c$
300	5.197±0.034	84.394±0.139	86.083±0.132	19.74	4.03	2.88
310	5.172±0.004	84.312±0.022	85.985±0.021	19.74	4.02	2.87
320	5.290±0.028	83.900±0.186	85.896±0.166	19.68	4.07	2.89
330	5.315±0.024	83.786±0.024	85.557±0.078	19.67	4.09	2.89

Table 6.5: Principal moments of inertia and axes lengths of the equivalent inertia spheroid. Moments of inertia are in 10^{-45} kg m^2 and axes lengths are in Å.

simulation lengths (about 1 ns compared to a timescale of 10-100 ns for molecular reorientation) rather than any polar ordering.

T / K	p_x	p_y	p_z	$\|\mathbf{p}\|$
300	3.12±4.63	-17.32±2.65	15.46±1.33	23.92±2.58
310	3.24±2.51	-10.06±2.71	19.54±1.38	22.48±1.94
320	2.22±4.03	1.14±4.53	14.07±1.62	15.51±1.72
330	1.10±3.83	-0.52±3.55	4.74±2.00	7.12±2.14

Table 6.6: Computed system polarizations. Here the director lies along the z-axis and $|\mathbf{p}|$ is the magnitude of the polarization vector $\mathbf{p}$. All polarizations are in 10^{-30} C m.

The reorientational motion of the molecules can be investigated using the reorientational time correlation functions [132, 278]

$$C_l(t) = \langle P_l(\hat{\mathbf{u}}_i(t_0).\hat{\mathbf{u}}_i(t_0+t))\rangle, \tag{6.38}$$

where $\hat{\mathbf{u}}_i$ is a unit vector defining the orientation of the molecule and $P_l(x)$ is the lth Legendre polynomial. The orientation of the molecule can be defined in a number of ways. Here two definitions have been used. The first is the *para* axis of the phenylcyclohexane core. $C_l(t)$ for this is shown in Fig. 6.8. The second uses the

CZ-NZ bond and this is shown in Fig. 6.9. These approximate the molecular long axis and dipole vector respectively.

In both cases it can be seen that decay of $C_1(t)$ is slow at all temperatures. This reflects the long times needed for a molecule in the nematic phase to rotate its long axis. This is the reason for the freezing in of a net polarization in this system. All the $C_l(t)$ are similar to those found for other liquid crystal systems [99] and qualitatively similar to those obtained for simple liquids [115,132] but with a longer decay time.

To ensure that there is no long range polar order in the system, the simulation data has been used to calculated the orientational correlation functions $g_1(r)$ and $g_2(r)$. These are shown in Fig. 6.10. As can be seen after an initial minima, $g_1(r)$ oscillates about 0. In contrast $g_2(r)$ has a maxima at about 5 Å, which is then followed by a decay to a value of about $\bar{P}_2^2$. The average values of the polarization are shown in Tab. 6.6.

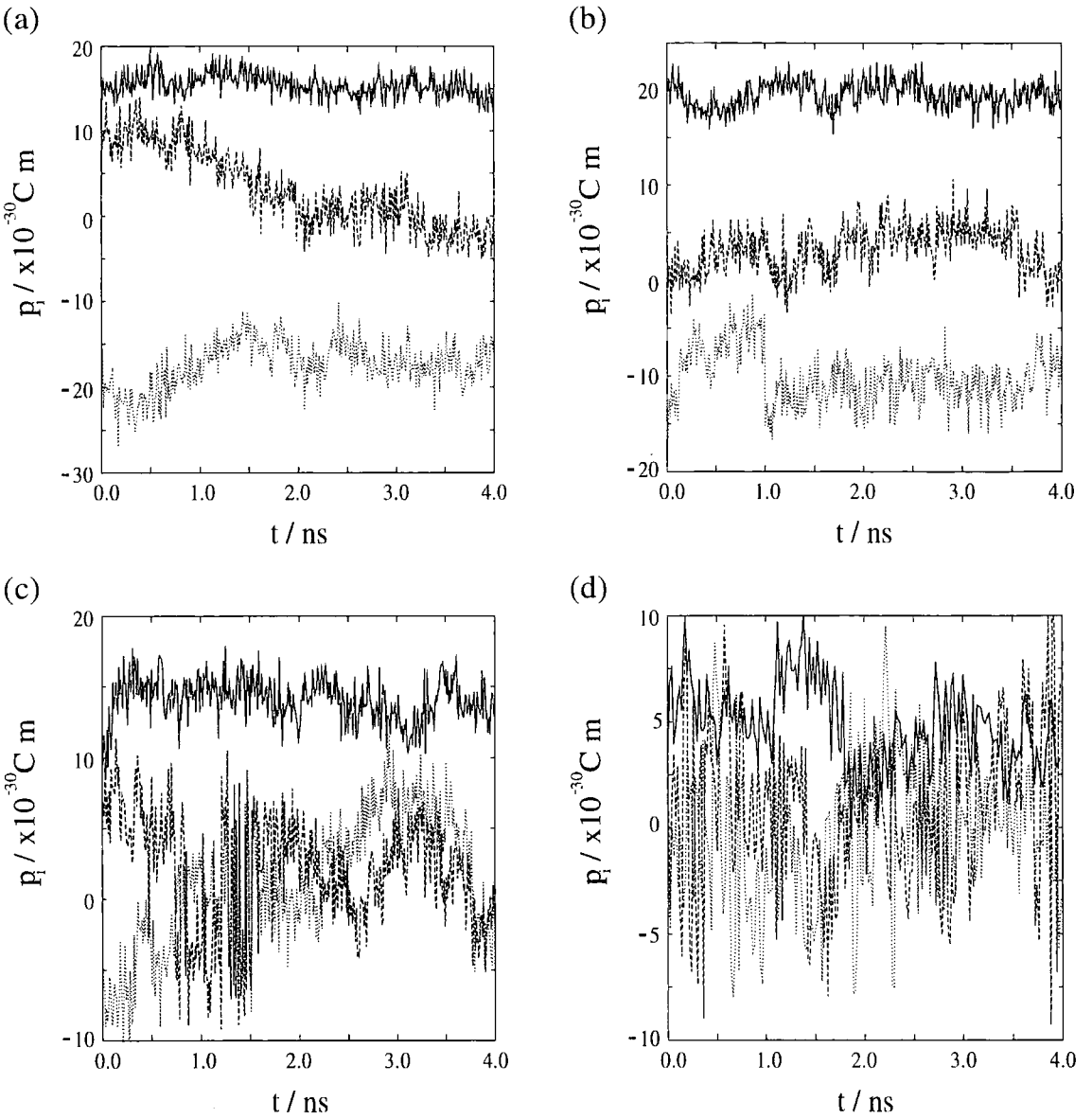

Figure 6.7: System polarization against time for simulated PCH5 at (a) 300 K, (b) 310 K, (c) 320 K, and (d) 330 K. The solid line denotes the polarization parallel to the director, while the dashed and dotted lines show the polarization perpendicular to the director.

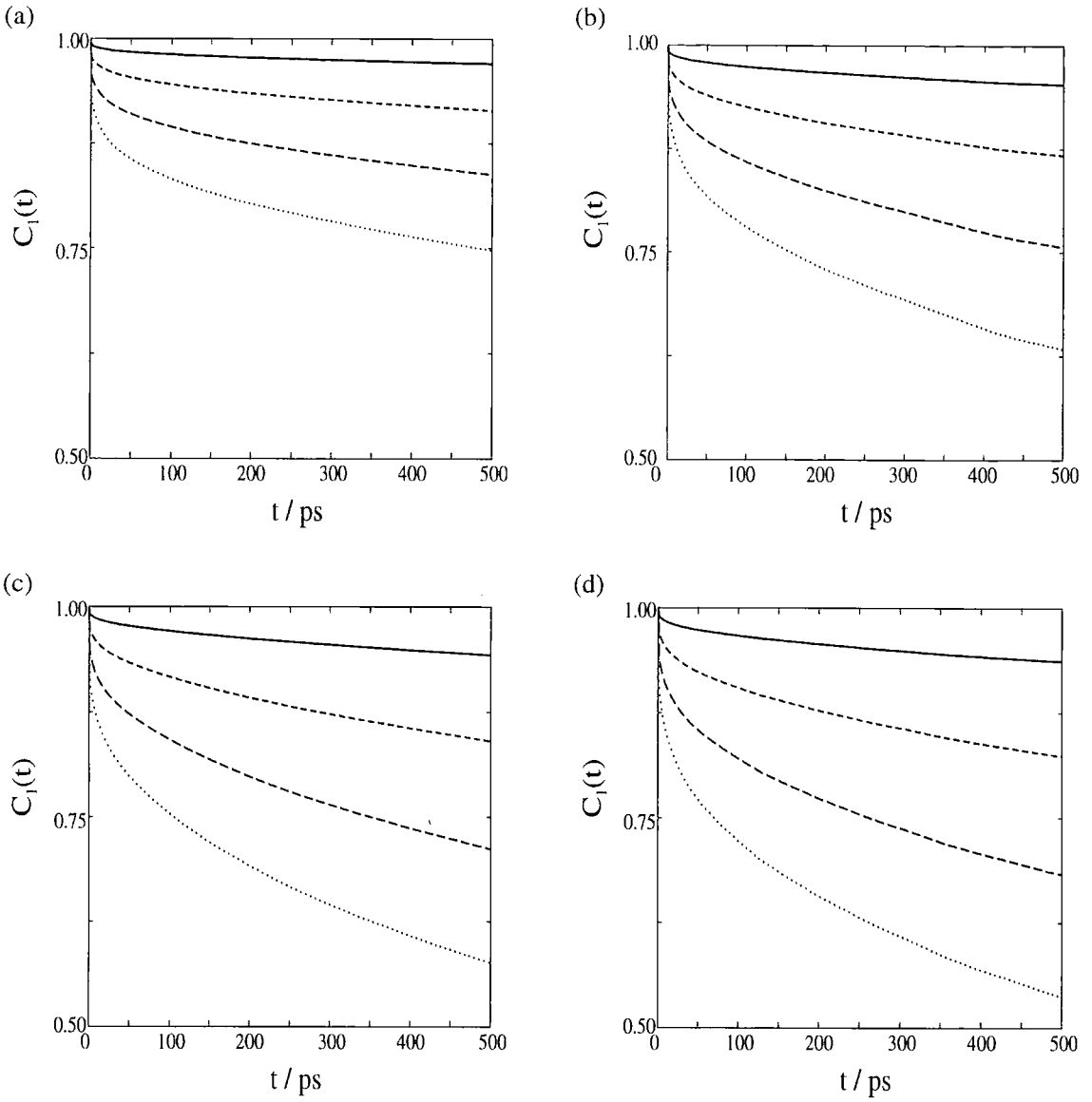

Figure 6.8: Orientational time correlation functions $C_l(t)$ $(l = 1, 2, 3, 4)$ for simulated PCH5 calculated using the para axis of the phenylcyclohexane core. (a) 300 K, (b) 310 K, (c) 320 K, and (d) 330 K. In each graph $C_1(t)$ is shown by the solid line, $C_2(t)$ is shown by the long dashed line, $C_3(t)$ is shown by the short dashed line, and $C_4(t)$ is shown by the dotted line.

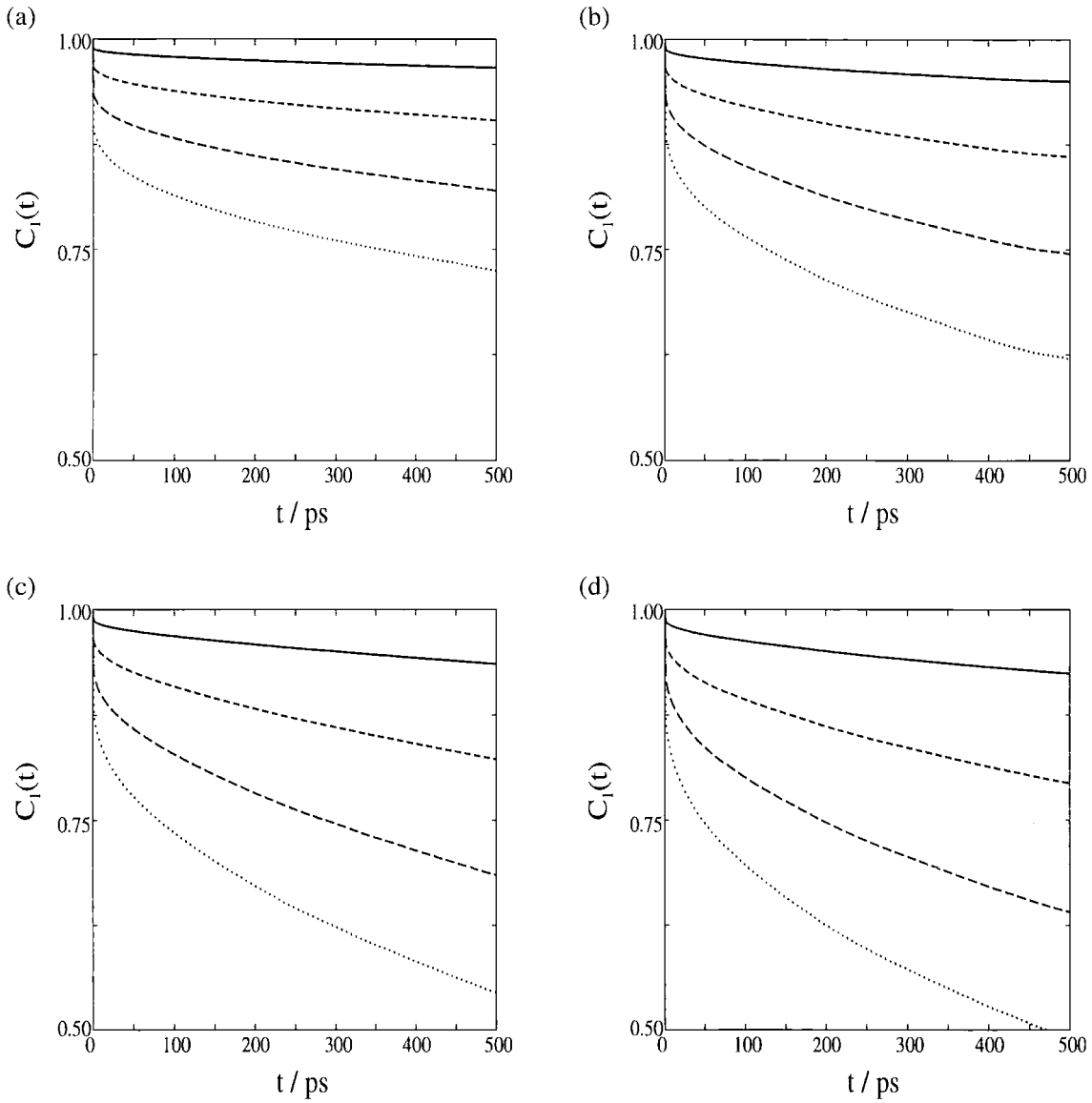

Figure 6.9: Orientational time correlation functions $C_l(t)$ $(l = 1, 2, 3, 4)$ for simulated PCH5 calculated using the CZ-NZ bond. (a) 300 K, (b) 310 K, (c) 320 K, and (d) 330 K. In each graph $C_1(t)$ is shown by the solid line, $C_2(t)$ is shown by the long dashed line, $C_3(t)$ is shown by the short dashed line, and $C_4(t)$ is shown by the dotted line.

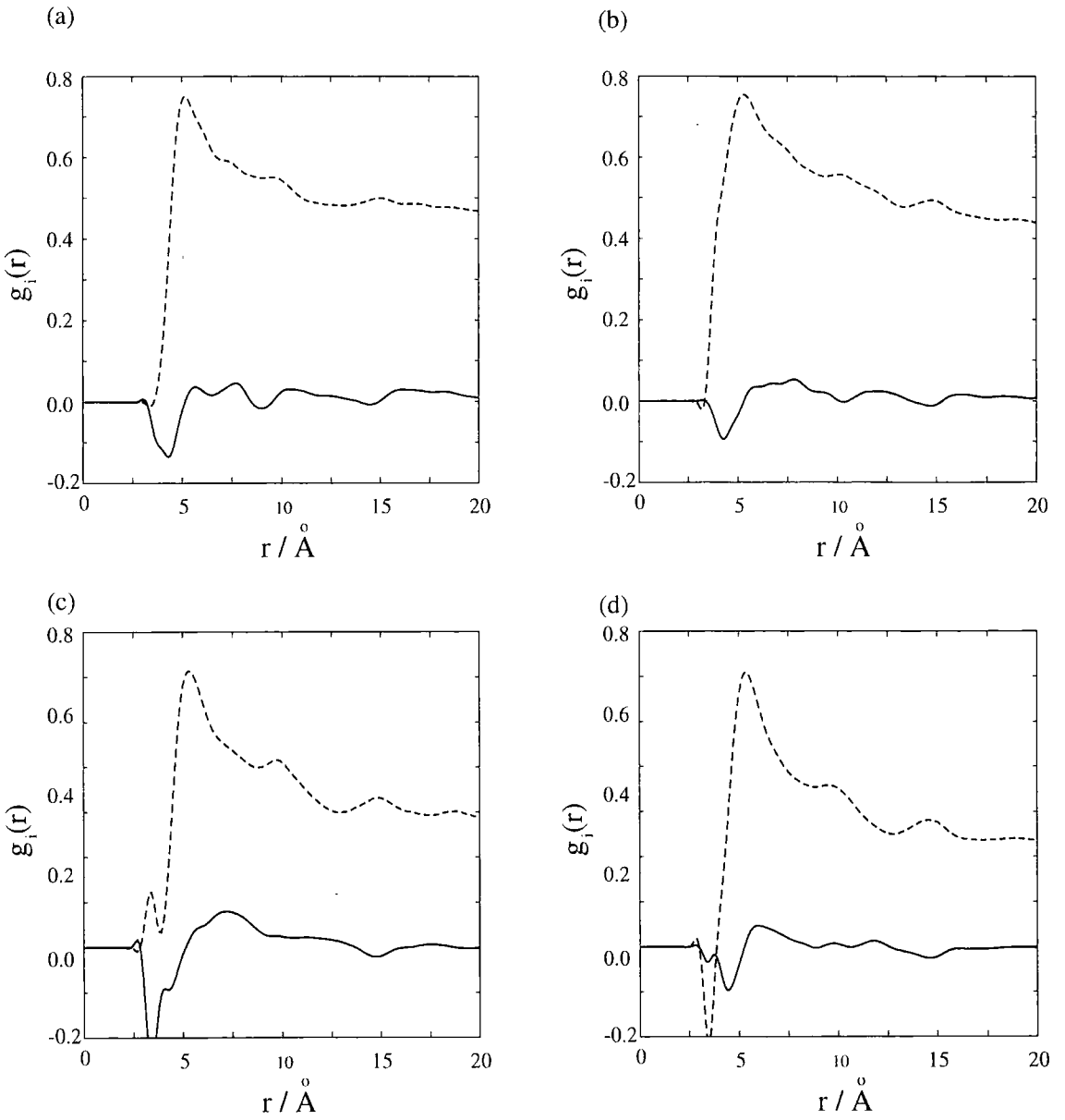

Figure 6.10: Orientational correlation functions $g_1(r)$ (solid line) and $g_2(r)$ (dashed line) at (a) 300 K, (b) 310 K, (c) 320 K, and (d) 330 K.

6.6.5 Flexoelectric Coefficients

The flexoelectric coefficients have been calculated using (6.27) and (6.29) and are shown in Tab. 6.7. Experimental data for e_s and e_b is scarce and often ambiguous [251]. Generally the magnitude is of the order of 10 pC m^{-1}, which agrees with the results presented here. For PCH5, experimental values for the flexoelectric coefficients have been determined [250] with e_s given as 5.3 pC m^{-1} and e_b as 3.3 pC m^{-1} at 303 K, with quoted errors of about 40 %. The temperature dependence of e_s and e_b was not fully considered in that study, the normalized difference of the coefficients $(e_s - e_b)/k_2$, where k_2 is the twist elastic constant, was measured and found to remain constant across the nematic range.

T / K	e_s / pC m^{-1}	e_b / pC m^{-1}
300	14.9±9.9	-1.7±1.8
310	13.2±11.2	1.4±1.0
320	3.9±1.8	2.5±1.2
330	2.7±1.5	0.1±1.2

Table 6.7: Calculated flexoelectric coefficients for simulated PCH5.

The flexoelectric coefficients show markedly different temperature dependences. e_s decays monotonically with temperature. On the other hand, e_b shows a rise with temperature, from -1.7 pC m^{-1} at 300 K to 2.5 pC m^{-1} at 320 K. This behaviour could be rationalized in a number of ways. The polarization of the dimer depends on the angle between the dipoles. Using a simple vector addition as shown in Fig. 6.12, the polarization from deforming a dimer is given by

$$\mathbf{p}_{ij} = \mathbf{m}_i + \mathbf{m}_j \tag{6.39}$$

$$\mathbf{p}_{ij} = \sqrt{|\mathbf{m}_i|^2 + |\mathbf{m}_j|^2 - 2|\mathbf{m}_i||\mathbf{m}_j|\cos\theta}\,\widehat{(\mathbf{m}_i + \mathbf{m}_j)}, \tag{6.40}$$

where $\mathbf{m}_i$ is the dipole moment of molecule i, $\mathbf{p}_{ij}$ is the polarization of the dimer. θ, $\mathbf{m}_i$, and $\mathbf{p}_{ij}$ are shown in Fig. 6.12. $\widehat{(\mathbf{m}_i + \mathbf{m}_j)}$ is the unit vector along $\mathbf{m}_i + \mathbf{m}_j$.

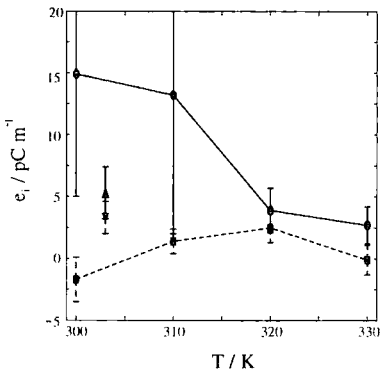

Figure 6.11: Flexoelectric coefficients e_s and e_b. The simulated values of e_s are marked by circles joined by the solid line and the simulated values of e_b are marked by squares joined by the dashed line. The experimental value for e_s is shown by the upward facing triangle and the experimental values for e_b is marked by the downward facing triangle.

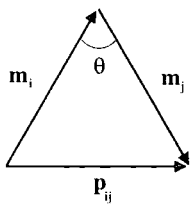

Figure 6.12: Vector diagram showing polarization $\mathbf{p}_{ij}$ caused by distorting molecules with dipole moments $\mathbf{m}_i$ and $\mathbf{m}_j$. For anti-parallel alignment, $\theta = 0$.

The energy cost to deform a dimer depends on the angle between the molecules, hence at higher temperatures the dimer can distort to larger angles, increasing the polarization. This temperature dependence may also be explained by an increase in the transverse dipole moment of the molecule with temperature. As the temperature increases the probability of the tail adopting a *gauche* conformation increases. The increase in the *gauche* populations with temperature can be seen from Fig. 6.6 and Tab. 6.4. This could cause the molecule to become increasingly bow-shaped and increase the transverse dipole moment. To examine this effect, the average molecular dipole moment, and its longitudinal, and transverse components, have

been calculated. The dipole moment of molecule i, $\mathbf{m}_i$, and its longitudinal and transverse components $\mathbf{m}_{li}$ and $\mathbf{m}_{ti}$ are given by

$$\mathbf{m}_i = \sum_j q_j \mathbf{r}_j \tag{6.41}$$

$$\mathbf{m}_{li} = (\mathbf{m}_i.\hat{\mathbf{u}}_i)\hat{\mathbf{u}}_i \tag{6.42}$$

$$\mathbf{m}_{ti} = \mathbf{m}_i - (\mathbf{m}_i.\hat{\mathbf{u}}_i)\hat{\mathbf{u}}_i, \tag{6.43}$$

where q_j is the charge on atom j, $\mathbf{r}_j$ is the position vector of atom j, and $\hat{\mathbf{u}}_i$ is the molecular long axis found from diagonalizing the inertia tensor (3.52). The sum in (6.41) runs over all atoms in molecule i. The average molecular dipoles are shown in Tab. 6.8. The average transverse dipole moment increases between 300 K and 320 K, similar to the temperature dependence of e_b. The longitudinal dipole moment shows a corresponding decrease. However, these changes are small compared to the statistical uncertainty in $\langle|\mathbf{m}_l|\rangle$ and $\langle|\mathbf{m}_t|\rangle$.

T / K	$\langle\|\mathbf{m}\|\rangle$ / $\times 10^{-30}$ C m	$\langle\|\mathbf{m}_l\|\rangle$ / $\times 10^{-30}$ C m	$\langle\|\mathbf{m}_t\|\rangle$ / $\times 10^{-30}$ C m
300	6.47±0.52	3.35±1.94	4.97±1.58
310	6.46±0.53	3.30±1.89	5.02±1.55
320	6.47±0.54	3.13±1.83	5.19±1.42
330	6.47±0.54	3.18±1.87	5.14±1.47

Table 6.8: Average dipole moments per molecule calculated using (6.41), (6.42), and (6.43).

The temperature dependence of e_s and e_b calculated here can be compared with the temperature dependence predicted theoretically. One such study [259] calculated e_s and e_b for the mesogen 5CB, similar in structure to PCH5, with a density functional approach. The molecules were modelled using a dipolar Gay-Berne potential [71] and the direct correlation function was calculated using a modified Bethe theory [279, 280] and the Percus-Yevick closure approximation [132]. This study

found e_s and e_b to be constant. The model used however neglected both molecular flexibility and long range dipole-dipole interactions, only interactions between nearest and next nearest neighbours were considered. The flexoelectric coefficients of the mesogen MBBA have also been calculated using a mean field model [258]. e_s and e_b were both found to decrease monotonically with temperature using this method.

Comparison with previous simulation results [76–78] in possible only on the qualitative level due to the vast differences in the models used. PCH5 is far from the idealized pear-shaped molecules described in §6.3. The simulations of Billeter and Pelcovits, and Zannoni *et al.* found that the splay flexoelectric coefficient decreases with temperature in agreement to the present results.

The dependence of e_s and e_b on the order parameter $\bar{P}_2$ is shown in Fig. 6.13. The order parameter dependence of e_s and e_b from previous studies give ambigu-

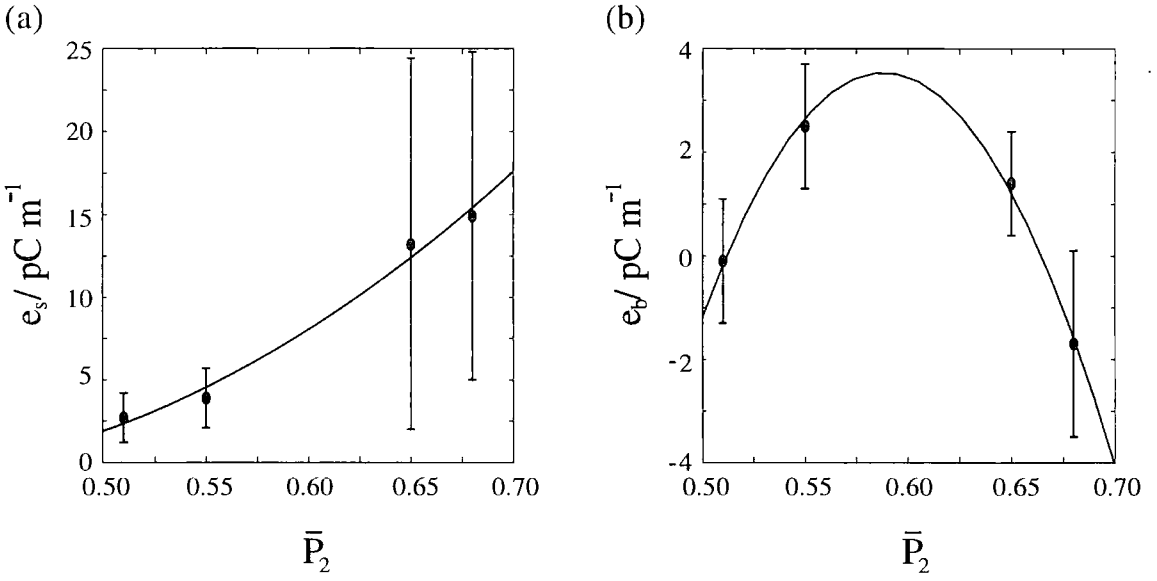

Figure 6.13: Order parameter dependence of (a) e_s and (b) e_b. The circles show the simulated data and the solid lines show the fitted quadratic in $\bar{P}_2$.

ous conclusions. Early work suggested that for dipolar molecules the flexoelectric coefficients are predicted to vary as $\bar{P}_2^2$ [281] while for quadrupolar molecules the flexoelectric coefficients should vary as $\bar{P}_2$ [241]. Using mean-field theory Osipov [253]

showed that both $\bar{P}_2$ and $\bar{P}_2^2$ dependence should be seen. It was also suggested that the effect of molecular flexibility would introduce a $\bar{P}_2^{-1}$ dependence [254]. However, recent experimental studies of 5CB [282] failed to find a simple $\bar{P}_2$ or $\bar{P}_2^2$ dependence.To test this a quadratic in $\bar{P}_2$ has been fitted to e_s and e_b and this is shown in Fig. 6.13. As can be seen these fit the simulated data well. The fitted quadratics are given by $e_s = 21.33 - 122.76\bar{P}_2 + 167.73\bar{P}_2^2$ and $e_b = -206.7 + 714.83\bar{P}_2 - 607.63\bar{P}_2^2$. In both cases the linear and quadratic coefficients are of the same order, suggesting that both the dipolar and quadrupolar flexoelectric effect are present in PCH5.

The contributions from the Van der Waals and electrostatic interactions to the flexoelectric coefficients have also been calculated. These are shown in Tab. 6.9. As can be seen the van der Waals and electrostatic contributions are generally of opposite sign, with the Van der Waals contribution generally the larger of the two. A possible cause of the reduction of the flexoelectric coefficients by the electrostatic interaction is the preference toward anti-parallel alignment of the molecular dipoles, which in the case of PCH5 is largely due to the cyano group. When a dimer is subjected to splay or bend the polar groups are able to bend away from the molecular axis to remain anti-parallel. While this would have a small effect on the van der Waals interaction between two molecules, is would have a larger effect on the electrostatic interaction.

T/ K	e_s^{vdw}	e_b^{vdw}	e_s^{elec}	e_b^{elec}
300	22.0±16.2	6.2±3.5	-7.7±3.6	-7.9±1.6
310	28.8±20.9	3.3±1.7	-15.6±3.0	-1.7±0.8
320	7.1±2.5	2.5±1.2	-3.2±1.6	1.3±0.6
330	2.6±0.9	-0.1±1.0	0.1±0.5	0.2±0.8

Table 6.9: Van der Waals and electrostatic contributions to the flexoelectric coefficients (in pC m^{-1}).

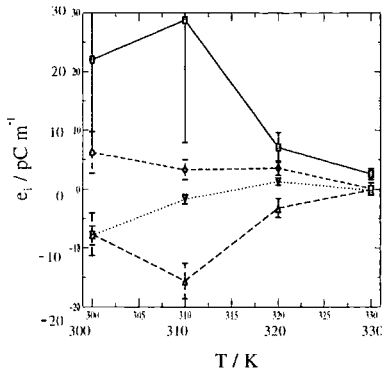

Figure 6.14: Temperature dependence of the van der Waals and electrostatic contributions to e_s and e_b. e_s^{vdw} is shown by the squares, e_s^{elec} is shown by diamonds, e_b^{vdw} is shown by upward pointing triangles, and e_b^{elec} is shown by downward pointing triangles.

6.7 Conclusions

Here the flexoelectric coefficients of a nematic liquid crystal have been calculated from an atomistic molecular dynamics simulation. The temperature dependence of e_s and e_b has been considered as have the contributions from different interactions. This is (to my knowledge) the first calculation of the flexoelectric coefficients from an atomistic simulation and the first attempt to quantify the roles of different interactions in determining the flexoelectric coefficients. As well as the flexoelectric coefficients the simulation data was used to calculate other properties such as the density and order parameters, as well as the molecular and liquid structure. From the results presented in §6.6 the following conclusions may be drawn.

- The order parameter monotonically decreases with temperature (Tab. 6.3) (an improvement over the 125 molecule system studied in Chapter 5). Order parameters of 0.51 to 0.68 and lack of periodic variation in $g_{\|}(r)$ (Fig. 6.5) clearly shows a nematic phase.

- The molecules become slightly longer and thinner with decreasing temperature

(Tab. 6.5 and Fig. 6.6) in accordance with mean-field theory.

- The calculated values of the flexoelectric coefficients (Tab. 6.7) are consistent with experimental data, although the paucity of experimental results makes detailed comparison difficult.

- The temperature dependence of the splay flexoelectric coefficient shows a monotonic decrease with temperature.

- The bend coefficient shows a more complicated temperature dependence. This could be due to an increase in the angle that can be made between molecules in a dimer. An alternative explanation could be that it arises due to an increase in the transverse molecular dipole moment with temperature.

- e_s and e_b show both linear and quadratic dependence on $\bar{P}_2$ suggesting the flexoelectric effect in PCH5 is a combination of the dipolar and quadrupolar effects.

- The contributions from the Van der Waals and electrostatic interactions are of the same order of magnitude and of different sign (Tab. 6.9).

A number of points about errors or deficiencies in this study should be made. The first concerns the overall polarization of the system. While this should not affect the calculated values of the flexoelectric coefficients it would be desirable to avoid this polarization in future simulations. This can be achieved through longer simulation runs. The decay of the orientational time correlation function $C_1(t)$, as presented in Fig. 6.8 and Fig. 6.9, show that re-orientational motion in liquid crystals is incredibly slow compared to other motions in the system. Thus simulation runs about 10 times longer than the present simulations would be needed. Another possibility would be to use Monte Carlo rather than molecular dynamics simulations, as in [76–78]. The ability of MC simulations to undertake unphysical moves such as flipping molecules round would increase the rate at which molecules re-orientate.

The second is the effect of system size on the calculation of the flexoelectric coefficients. This is likely to have most effect on the electrostatic interactions as these are long-ranged. Considering interactions between more molecules could possibly lead to a change in e_s and e_b.

This work can be extend in a number of ways. The effect of increasing system sizes and run lengths can be studied. While this system is quite large for atomistic studies, recently a number of atomistic simulations have been performed on systems of about 1000 molecules [106]. Likewise, while available computer time has restricted the run lengths to 4 ns, with increasing computer power and improved simulation algorithms allow simulation runs of the order of tens of nanoseconds.

A second extension is to different mesogens. Study of molecules possessing wedge or banana shapes (as in the previous simulation studies of idealized molecules [76–78]), or molecules exhibiting quadrupolar flexoelectricity would be possible. Using this method to calculate the flexoelectric coefficients for a range of different molecules would be useful to check its accuracy. It would also be interesting to compare the contribution to e_s and e_b for molecules exhibiting different flexoelectric mechanisms.

A final extension would be the investigation of alternative methods for determining the flexoelectric coefficients. Of the other possible methods the density functional method used by Zannoni and *et al.* [76, 77] combined with a more accurate method for the determination of the direct correlation function [273] could provide a good alternative route to e_s and e_b. The surface tensor model of Ferrarini [258] could also be used. This has the advantage of requiring only single molecule calculations. However for flexible molecules such as PCH5 it is necessary to consider different conformations of the molecule with the correct statistical weighting. Finally it may be possible to calculate the flexoelectric coefficients from a non-equilibrium simulation by applying deformations to the system. However, unlike the case of a twist deformation from which the helicity parameter may be determined, it is impossible to apply uniform splay or bend deformations within periodic boundary conditions.

A geometry similar to a hybrid-aligned nematic cell, which combines splay and bend distortions, may be set up. The polarizations normal and parallel to the surface can then be related to the sum and difference of the flexoelectric coefficients. The equilibration times for this method may be long however (on the order of the molecular re-orientation time). Also to obtain a well defined deformed director field system sizes much larger than that used here would have to be used.

Chapter 7

Summary

The work presented in this thesis concerns the simulation of liquid molcules and the calculation of material properties in a nematic liquid crystal phase.

The first part of this work aimed to construct accurate potential functions for liquid crystal molecules. Construction and parameterization of force fields is a difficult task, and there has been much work in this area. Atomistic modelling of liquid crystals is a particularly demanding task, due to the large amount of conformational freedom. Accurate potentials are needed for internal torsional rotations. Liquid crystals often contain features such as lateral and terminal polar groups and mixed aromatic-aliphatic groups that are absent from many force fields. First principles density functional theory calculations were performed for molecules containing some of these functional groups and these were used to calculate force field parameters. Liquid state molecular dynamics simulations were then performed on these molecules using the derived force field. Important thermodynamic properties (densities and heats of vapourization) were calculated to verify the accuracy of the underlying force field. Good agreement was found between the values calculated from simulation and experimental values.

The second part of this thesis involved the calculation of the rotational viscosity coefficient γ_1 from molecular dynamics simulations. γ_1 is an important parameter in

determining the switching properties of liquid crystalline displays and in the rheology of liquid crystals. Equilibrium molecular dynamics simulations of the nematogen PCH5 were performed and γ_1 was determined using several different methods. Agreement with experimental values of γ_1 was generally good, with two methods, one involving the director angular velocity correlation function and the other the director mean squared displacement, giving particularly good agreement. The effect of increasing system size of the values of γ_1 was also investigated. Generally this resulted in values of γ_1 in better agreement with experiment.

The final part of this work was the study of the flexoelectric effect. This effect is becoming increasingly important for several reasons. It is used in several newly developed types of liquid crystal display. Experimental determination of the flexoelectric coefficients, which determine the polarization response to a director deformation, are poorly determined from experiment. Thus a method for finding these coefficients from simulation is of great interest. Molecular dynamics simulations PCH5 were performed using the force field. The flexoelectric coefficients e_s and e_b were calculated from correlation functions of the polarization and orientational stress. e_s and e_b were found to be consistent with the available experimental data. The temperature and order parameter dependence of e_s and e_b was examined. e_s was found to decay monotonically with temperature, while e_b showed an inital increase with temperature followed by a decay. Both e_s and e_b showed a quadratic dependence on the order parameter $\bar{P}_2$. The contributions from the Van der Waals and electrostatic interactions were also examined. They were found to be of similar magnitude and opposite sign.

In all parts of this work atomistic models were used to model liquid crystalline molecules. This allowed the accurate modelling of such effects as molecular flexibility and long range electrostatic interactions, which is not possible with simpler models such as the Gay-Berne potential. However, computational expense restricted the system sizes studied to 125-216 molecules and simulation times to a few nanoseconds,

increasing computer power (including the increased use of parallel computers) and improvements to simulation techniques, will lead to the simulation of larger system sizes and longer time scales with a consequent improvement in the quality of results.

This work aims to provide some insight into the relationship between molecular structure and material properites in liquid crystals. This is of both academic and industrial interest. As computer power increases the possibility of determining the bulk properties of a material from its molecular structure alone becomes increasingly realistic.

Bibliography

[1] G. W. Gray *Introduction and Historical Introduction* in *Physical Properties of Liquid Crystals*, editors D. Demus, J. Goodby, G. W. Gray, H. W. Spiess, and V. Vill page 1 Wiley-VCH, New York (1998)

[2] F. Reinitzer *Montash. Chem.* **9**, 421 (1888)

[3] G. Friedel *Ann. Physique.* **18**, 273 (1922)

[4] J. W. Goodby *Curr. Opin. Solid State Mater. Sci.* **4**, 361 (1999)

[5] P. G. de Gennes *Physics of Liquid Crystals* Oxford (1976)

[6] M. Baron *Pure Appl. Chem.* **73**, 845 (2001)

[7] D. Demus, J. W. Goodby, G. W. Gray, H. W. Spiess, and V. Vill, editors *Handbook of Liquid Crystals* volume 2B Discotic Liquid Crystals Wiley-VCH, New York (1998)

[8] G. Pelzl, S. Diele, and W. Weissflog *Adv. Mater.* **11**, 707 (1999)

[9] D. Demus, J. W. Goodby, G. W. Gray, H. W. Spiess, and V. Vill, editors *Handbook of Liquid Crystals* volume 3 High Molecular Mass Liquid Crystals Wiley-VCH, New York (1998)

[10] K. Lorenz, D. Holter, B. Stuhn, R. Mulhaupt, and H. Frey *Adv. Mater.* **8**, 414 (1996)

[11] F. Vogtle, S. Gestermann, R. Hesse, H. Schwierz, and B. Windisch *Prog. Polym. Sci.* **25**, 987 (2000)

[12] C. E. Fairhurst, S. Fuller, J. Gray, M. C. Holmes, and G. J. T. Tiddy *Lyotropic Surfactant Liquid Crystals* in *Handbook of Liquid Crystals*, editors D. Demus, J. W. Goodby, G. W. Gray, H. W. Spiess, and V. Vill volume 3 High Molecular Mass Liquid Crystals page 341 Wiley-VCH (1998)

[13] D. Fazio, C. Mongin, B. Donnio, Y. Galerne, D. Guillon, and D. W. Bruce *J. Mater. Chem* **11**, 2852 (2001)

[14] A. Saupe *Angew. Chem. Int. Ed.* **7**, 97 (1968)

[15] R. Eppenga and D. Frenkel *Molec. Phys.* **52**, 1303 (1984)

[16] G. Vertogen and W. H. de Jeu *Thermotropic Liquid Crystals, Fundamentals* Springer-Verlag (1988)

[17] S. J. Picken *Measurements and Valules for Selected Order Parameters* in *Physical Properties of Liquid Crystals: Nematics*, editors D. A. Dunmur, A. Fukuda, and G. R. Luckhurst page 89 INSPEC, the Institution of Electrical Engineers, London (2001)

[18] G. Unger *X-ray Studies of Nematic Systems* in *Physical Properties of Liquid Crystals: Nematics*, editors D. A. Dunmur, A. Fukuda, and G. R. Luckhurst page 177 INSPEC, the Institution of Electrical Engineers, London (2001)

[19] R. M. Richardson *Neutron Scattering Studies of Nematic Mesophase Structures* in *Physical Properties of Liquid Crystals: Nematics*, editors D. A. Dunmur, A. Fukuda, and G. R. Luckhurst page 192 INSPEC, the Institution of Electrical Engineers, London (2001)

[20] C. Tschierske *J. Mater. Chem.* **11**, 2647 (2001)

[21] C. Zannoni *J. Mater. Chem.* **11**, 2637 (2001)

[22] A. Szabo and N. S. Ostlund *Modern Quantum chemistry* MacMillian, New York (1982)

[23] F. J. Jensen *Introduction to Computational Chemistry* Wiley, Chichester (1999)

[24] A. St-Amant, W. D. Cornell, P. A. Kollman, and T. A. Halgren *J. Comput. Chem.* **16**, 1483 (1995)

[25] The 1998 Nobel Prize in chemistry: http://www.nobel.se/chemistry/laureates/1998/

[26] P. Hohenberg and W. Kohn *Phys. Rev.* **136**, B864 (1964)

[27] W. Kohn and L. J. Sham *Phys. Rev.* **140**, A1133 (1965)

[28] L. H. Thomas *Proc. Camb. Phil. Soc.* **23**, 542 (1927)

[29] R. O. Jones and O. Gunnarsson *Rev. Mod. Phys* **61**, 689 (1989)

[30] R. G. Parr and W. Yang *Density Functional Theory of Atoms and Molecules* Oxford University Press, Oxford (1989)

[31] P. Ziesche, S. Kurth, and J. P. Perdew *Comp. Mat. Sci.* **11**, 122 (1998)

[32] P. A. M. Dirac *Proc. Cambridge Phil. Soc.* **26**, 376 (1930)

[33] D. M. Ceperley and B. J. Alder *Phys. Rev. Lett.* **45**, 566 (1980)

[34] S. J. Vosko, L. Wilk, and M. Nusair *Can. J. Phys.* **58**, 1200 (1980)

[35] J. P. Perdew and Y. Wang *Phys. Rev. B* **45**, 13244 (1992)

[36] J. P. Perdew, J. A. Chevary, S. Vosko, K. A. Jackson, M. R. Pederson, D. J. Singh, and C. Fiolhais *Phys. Rev. B* **46**, 6671 (1992)

[37] J. S. Blakemore *Solid State Physics* Cambrige University Press, Cambridge second edition (1985)

[38] M. C. Payne, M. P. Teter, D. C. Allan, T. A. Arias, and J. D. Joannopoulos *Rev. Mod. Phys* **64**, 1045 (1992)

[39] M. T. Yin and M. L. Cohen *Phys. Rev. B* **25**, 7403 (1982)

[40] L. Kleinman and D. M. Bylander *Phys. Rev. Lett.* **48**, 1425 (1982)

[41] D. Vanderbilt *Phys. Rev. B* **41**, 7892 (1990)

[42] M. D. Segall, P. J. D. Linden, M. J. Probert, C. J. Pickard, P. J. Hasnip, S. J. Clark, and M. C. Payne *J. Phys. Condens. Matter* **14**, 2717 (2002)

[43] J. Crain and S. J. Clark *Calculation of structure and dynamical properties of liquid crystal molecules* in *Liquid Crystals I*, editor D. M. P. Mingos volume 94 of *Structure and Bonding* page 1 Springer-Verlag, Berlin (1999)

[44] G. Brocks *Theor. Chem. Acc.* **104**, 116 (1999)

[45] R. Car and M. Parrinello *Phys. Rev. Lett.* **55**, 2471 (1985)

[46] M. P. Teter, M. C. Payne, and D. C. Allan *Phys. Rev. B* **40**, 12255 (1989)

[47] W. H. Press, B. P. Flannery, S. A. Teukolsky, and W. T. Vetterling *Numerical Recipies* Cambridge University Press (1992)

[48] I. Stich, R. Car, M. Parrinello, and S. Baroni *Phys. Rev. B* **39**, 4997 (1989)

[49] R. P. Feynman *Phys. Rev.* **56**, 340 (1939)

[50] P. Pulay *Molec. Phys.* **19**, 197 (1969)

[51] G. P. Francis and M. C. Payne *J. Phys. Condens. Matter* **2**, 4395 (1989)

[52] *Castep version 3.9, Academic Version, licensed under the UKCP-MSI Agreement* (1999)

[53] N. Metropolis, A. W. Rosenbluth, M. N. Rosenbluth, A. H. Teller, and E. Teller *J. Chem. Phys.* **21**, 1087 (1953)

[54] B. J. Alder and T. E. Wainwright *J. Chem. Phys.* **27**, 1208 (1957)

[55] B. J. Alder and T. E. Wainwright *J. Chem. Phys.* **31**, 459 (1959)

[56] B. J. Alder and T. E. Wainwright *J. Chem. Phys.* **33**, 1439 (1960)

[57] W. W. Wood and F. R. Parker *J. Chem. Phys.* **27**, 720 (1957)

[58] A. Rahman *Phys. Rev.* **136A**, 405 (1964)

[59] L. Verlet *Phys. Rev.* **159**, 98 (1967)

[60] L. Verlet *Phys. Rev.* **165**, 201 (1968)

[61] B. J. Alder and T. E. Wainwright *Phys. Rev. A* **1**, 18 (1970)

[62] T. C. Lubensky *Solid State Comm.* **102**, 187 (1997)

[63] P. A. Lebwohl and G. Lasher *Phys. Rev. A* **6**, 426 (1972)

[64] M. P. Allen, G. T. Evans, D. Frenkel, and B. M. Mulder *Adv. Chem. Phys.* **86**, 1 (1993)

[65] M. A. Bates *Results of Hard Particle Simulations* in *Physical Properties of Liquid Crystals: Nematics*, editors D. A. Dunmar, A. Fukuda, and G. R. Luckhurst page 613 INSPEC, the Institution of Electrical Engineers, London (2001)

[66] D. Frenkel, B. M. Mulder, and J. P. McTague *Phys. Rev. Lett.* **52**, 287 (1984)

[67] D. Frenkel and B. M. Mulder *Molec. Phys.* **55**, 1171 (1985)

[68] A. Stroobants, H. N. W. Lekkerkerker, and D. Frenkel *Phys. Rev. Lett.* **57**, 1452 (1986)

[69] J. E. Lennard-Jones *Proc. R. Soc. Lond. Ser. A* **106**, 463 (1924)

[70] J. Corner *Proc. R. Soc. Lond.* **A192**, 275 (1948)

[71] J. G. Gay and B. J. Berne *J. Chem. Phys.* **74**, 3316 (1981)

[72] M. A. Bates and G. R. Luckhurst *Computer simulation of liquid crystal phases formed by Gay-Berne mesogens* in *Liquid Crystals I*, editor D. M. P. Mingos volume 94 of *Structure and Bonding* page 65 Springer-Verlag, Berlin (1999)

[73] C. Zannoni *Results of Generic Model Simulations* in *Physical Properties of Liquid Crystals: Nematics*, editors D. A. Dunmur, A. Fukuda, and G. R. Luckhurst page 624 INSPEC, the Institution of Electrical Engineers, London (2001)

[74] P. J. Camp, M. P. Allen, and A. J. Masters *J. Chem. Phys.* **111**, 9871 (1999)

[75] S. J. Johnson, R. J. Low, and M. P. Neal *Phys. Rev. E* **65**, 051706 (2002)

[76] J. Stelzer, R. Berardi, and C. Zannoni *Chem. Phys. Lett.* **299**, 9 (1999)

[77] J. Stelzer, R. Berardi, and C. Zannoni *Molec. Cryst. Liq. Cryst.* **352**, 186 (2000)

[78] J. L. Billeter and R. A. Pelcovits *Liq. Cryst.* **27**, 1151 (2000)

[79] R. Berardi, M. Ricci, and C. Zannoni *ChemPhysChem* **2**, 186 (2001)

[80] E. Egberts and H. J. C. Berensden *J. Chem. Phys.* **89**, 3718 (1988)

[81] A. V. Komolkin, Y. V. Molchanov, and P. P. Yakutseni *Liq. Cryst.* **6**, 39 (1989)

[82] M. R. Wilson and M. P. Allen *Molec. Cryst. Liq. Cryst.* **198**, 465 (1991)

[83] M. R. Wilson and M. P. Allen *Liq. Cryst.* **12**, 157 (1992)

[84] A. Maliniak *J. Chem. Phys.* **96**, 2306 (1992)

[85] M. Yoneya and H. J. C. Berendsen *J. Phys. Soc. Japan* **63**, 1025 (1994)

[86] D. J. Cleaver and D. J. Tildesley *Molec. Phys.* **81**, 781 (1994)

[87] A. V. Komolkin, A. Laaksonen, and A. Maliniak *J. Chem. Phys.* **101**, 4103 (1994)

[88] C. W. Cross and B. M. Fung *J. Chem. Phys.* **101**, 6839 (1994)

[89] M. A. Glaser, R. Malzbender, N. A. Clark, and D. M. Walba *J. Phys. Condens. Matter* **6**, 261 (1994)

[90] D. J. Cleaver, M. J. Callaway, T. Forester, W. Smith, and D. J. Tildesley *Molec. Phys.* **86**, 613 (1995)

[91] C. W. Cross and B. M. Fung *Molec. Cryst. Liq. Cryst.* **262**, 507 (1995)

[92] S. Y. Yavenko, A. A. Muravski, G. Krömer, and A. Geiger *Molec. Phys.* **86**, 1099 (1995)

[93] S. Hauptmann, T. Mosell, S. Reiling, and J. Brickmann *Chem. Phys.* **208**, 57 (1996)

[94] D. Sandström, A. V. Komolkin, and A. Maliniak *J. Chem. Phys.* **104**, 9620 (1996)

[95] S. Y. Yavenko, A. A. Muravski, F. Eikelschulte, and A. Geiger *J. Chem. Phys.* **105**, 10766 (1996)

[96] D. Sandström, A. V. Komolkin, and A. Maliniak *J. Chem. Phys.* **106**, 7438 (1997)

[97] D. R. Binger and S. Hanna *Molec. Cryst. Liq. Cryst.* **302**, 63 (1997)

[98] S. Y. Yavenko, A. A. Muravski, F. Eikleschulte, and A. Geiger *Liq. Cryst.* **24**, 657 (1998)

[99] C. McBride, M. R. Wilson, and J. A. K. Howard *Molec. Phys.* **93**, 955 (1998)

[100] M. A. Glaser *Atomistic Simulation and Modeling of Smectic Liquid Crystals* in *Advances in the Computer Simulation of Liquid Crystals*, editors P. Pasini and C. Zannoni Kluwer, Dordecht (2000)

[101] K.-J. Lee, G.-H. Hsuie, J.-L. Wu, and J.-H. Chen *Liq. Cryst.* **26**, 46 (1999)

[102] M. J. Cook and M. R. Wilson *Liq. Cryst.* **27**, 1573 (2000)

[103] Y. Lansac, M. A. Glaser, and N. A. Clark *Phys. Rev. E* **64**, 051703 (2001)

[104] W. G. Jang, M. A. Glaser, C. S. Park, K. H. Kim, Y. Lansac, and N. A. Clark *Phys. Rev. E* **64**, 051712 (2001)

[105] M. J. Cook and M. R. Wilson *Molec. Cryst. Liq. Cryst.* **357**, 127 (2001)

[106] M. J. Cook and M. R. Wilson *Molec. Cryst. Liq. Cryst.* **363**, 181 (2001)

[107] Z. Wang, J. A. Lupo, S. Patnaik, and R. Patcher *Comput. Theo. Polymer Sci.* **11**, 375 (2001)

[108] J. S. van Duijneveldt and M. P. Allen *Molec. Phys.* **92**, 855 (1997)

[109] G. La Penna, D. Catalano, and C. A. Veracini *J. Chem. Phys.* **105**, 7097 (1996)

[110] M. R. Wilson *J. Chem. Phys.* **107**, 8654 (1997)

[111] A. V. Lyulin, M. S. Al Barwani, M. P. Allen, M. R. Wilson, I. Neelov, and N. K. Allsop *Macromolecules* **31**, 4626 (1998)

[112] C. McBride and M. R. Wilson *Molec. Phys.* **97**, 511 (1999)

[113] D. J. Cleaver, C. M. Care, M. P. Allen, and M. P. Neal *Phys. Rev. E* **54**, 559 (1997)

[114] N. L. Allinger and U. Burkett *Molecular Mechanics* American Chemical Society, Washington DC (1982)

[115] M. P. Allen and D. J. Tildesley *Computer Simulation of Liquids* Oxford University Press, Oxford (1989)

[116] H. Goldstein *Classical Mechanics* Addison-Wesley, Reading, MA 2nd edition (1980)

[117] J. P. Ryckaert, G. Ciccotti, and H. J. C. Berensden *J. Comput. Phys.* **23**, 327 (1977)

[118] H. J. C. Berensden, J. P. M. Postma, W. F. V. Gunsteren, A. D. Nola, and J. R. Haak *J. Chem. Phys.* **81**, 3864 (1984)

[119] D. J. Evans and G. P. Morris *Phys. Lett* **98A**, 433 (1983)

[120] D. J. Evans and G. P. Morris *Chem. Phys.* **77**, 63 (1983)

[121] H. C. Anderson *J. Chem. Phys.* **72**, 2384 (1980)

[122] S. Nosé *Molec. Phys.* **52**, 1055 (1984)

[123] W. G. Hoover *Phys. Rev. A* **31**, 1695 (1985)

[124] S. Melchonna, G. Ciccotti, and B. L. Holian *Molec. Phys.* **78**, 583 (1993)

[125] W. L. Jorgensen and J. Tirado-Rives *J. Phys. Chem.* **100**, 14508 (1996)

[126] D. Frenkel and B. Smit *Understanding Molecular Simulation* Academic Press second edition (2001)

[127] P. Ewald *Ann. Phys.* **64**, 253 (1921)

[128] J. Eastwood and R. Hockney *J. Comput. Phys.* **16**, 342 (1974)

[129] A. Y. Toukmaji and J. A. Board *Comp. Phys. Comm.* **95**, 73 (1996)

[130] K. Esselink *Comp. Phys. Comm.* **87**, 375 (1995)

[131] J. A. Barker and R. O. Watts *Molec. Phys.* **26**, 789 (1973)

[132] J. P. Hansen and I. R. McDonald *Theory of Simple Liquids* Academic Press, New York second edition (1990)

[133] B. M. Ladanyi and T. Keyes *Molec. Phys.* **33**, 1063 (1977)

[134] M. R. Battaglia, T. I. Cox, and P. A. Madden *Molec. Phys.* **37**, 1413 (1979)

[135] M. R. Wilson *J. Mol. Liq.* **68**, 23 (1996)

[136] C. Zannoni *A Internal Order Parameter Formalism for Non-rigid Molecules* in *Nuclear Magnetic Resonance of Liquid Crystals*, editor J. W. Emsley page 35 Kluwer, Drodecht (1985)

[137] M. R. Wilson, M. J. Cook, and C. McBride *Atomistic Modeling of Liquid Crystal Phases* in *Advances in the Computer Simulation of Liquid Crystals*, editors P. Pasini and C. Zannoni page 251 Kluwer, Dordecht (2000)

[138] M. R. Wilson *Atomistic simulations of liquid crystals* in *Liquid Crystals I*, editor D. M. P. Mingos volume 94 of *Structure and Bonding* page 42 Springer-Verlag, Berlin (1999)

[139] P. M. Morse *Phys. Rev.* **34**, 57 (1929)

[140] A. J. Stone *The Theory of Intermolecular Forces* Oxford University Press, Oxford (1996)

[141] J. R. Hill *J. Chem. Phys.* **16** (1948)

[142] N. L. Allinger, Y. H. Yuh, and J.-H. Lii *J. Am. Chem. Soc.* **111**, 8551 (1989)

[143] W. D. Cornell, P. Cieplak, C. I. Bayly, I. R. Gould, K. M. Merz, D. M. Ferguson, T. Fox, J. W. Caldwell, and P. A. Kollman *J. Am. Chem. Soc.* **117**, 5179 (1995)

[144] N. L. Allinger, K. Chen, and J.-H. Lii *J. Comput. Chem.* **14**, 642 (1996)

[145] N. Nevins, K. Chen, and N. L. Allinger *J. Comput. Chem.* **14**, 669 (1996)

[146] N. Nevins, J.-H. Lii, and N. L. Allinger *J. Comput. Chem.* **14**, 695 (1996)

[147] N. L. Allinger, K. Chen, J. A. Katzeellenbogen, S. R. Wilson, and G. M. Anstead *J. Comput. Chem.* **14**, 747 (1996)

[148] E. Garcia, M. A. Glaser, N. A. Clark, and D. M. Walba *J. Mol. Struct. (Theochem)* **464**, 39 (1999)

[149] N. L. Allinger *J. Am. Chem. Soc.* **99**, 3279 (1977)

[150] T. A. Halgren *J. Comput. Chem.* **14**, 490 (1996)

[151] C. S. Ewig, R. Berry, U. Dinur, J. R. Hill, M. G. Hwang, H. Li, C. Liang, J. Maple, Z. Peng, T. P. Stckfisch, T. S. Thacher, L. Yan, X. Ni, and A. T. Hagler *J. Comput. Chem.* **22**, 1782 (2001)

[152] E. Sigfridsson and U. Ryde *J. Comput. Chem.* **19**, 377 (1998)

[153] W. Damm, J. Tirado-Rives, and W. L. Jorgensen *J. Am. Chem. Soc.* **118**, 11225 (1996)

[154] W. Damm, J. Tirado-Rives, and W. L. Jorgensen *Supporting Information for the OPLS-AA Force Field* (1996)

[155] N. L. Allinger, M. T. T. andd M. A. Miller, and D. H. Wertz *J. Am. Chem. Soc.* **93**, 1637 (1971)

[156] J.-H. Lii and N. L. Allinger *J. Am. Chem. Soc.* **111**, 8566 (1989)

[157] J.-H. Lii and N. L. Allinger *J. Am. Chem. Soc.* page 8576 (1989)

[158] S. J. Weiner, P. A. Kollman, D. A. Case, U. C. Singh, C. Chio, G. Alagona, S. Profeta, and P. Weiner *J. Am. Chem. Soc.* **106** (1984)

[159] R. Brooks, R. E. Bruccoleri, B. D. Olafson, D. J. States, S. Swaminathan, and M. Karplus *J. Comput. Chem.* **4**, 1234 (1983)

[160] T. A. Halgren *J. Comput. Chem.* **14**, 520 (1996)

[161] T. A. Halgren *J. Comput. Chem.* **14**, 553 (1996)

[162] T. A. Halgren and R. B. Nachbar *J. Comput. Chem.* **14**, 587 (1996)

[163] T. A. Halgren *J. Comput. Chem.* **14**, 616 (1996)

[164] T. A. Halgren *J. Comput. Chem.* **20**, 720 (1999)

[165] T. A. Halgren *J. Comput. Chem.* **20**, 730 (1999)

[166] *Cerius*^{2} *is a molecular modelling package distributed by Biosym Molecular Simulations Inc.* (1999)

[167] *DL_POLY is a package of molecular simulation routines written by W. Smith and T. R. Forester, copyright The Council for the Central Laboratory of the Research Councils, Daresbury Laboratory at Daresbury, Nr. Warrington.* (1996)

[168] G. Kaminsky and W. L. .Jorgensen *J. Phys. Chem.* **100**, 18010 (1996)

[169] B. Chen, M. G. Matrin, and J. I. Siepmann *J. Phys. Chem. B* **102**, 2578 (1998)

[170] W. L. Jorgensen, T. B. Nguyen, and J. Tirado-Rives *J. Comput. Chem.* **14**, 195 (1993)

[171] C. J. Adam, S. J. Clark, M. R. Wilson, G. J. Ackland, and J. Crain *Molec. Phys.* **93**, 947 (1998)

[172] S. Tsuzuki, T. Uchimaru, K. Matsumura, M. Mikami, and K. Tanabe *J. Chem. Phys.* **110**, 2858 (1999)

[173] A. Karpfen, C. H. Choi, and M. Kertesz *J. Phys. Chem. A* **101**, 7426 (1997)

[174] S. Arulmozhiraja and T. Fujii *J. Chem. Phys.* **115**, 10589 (2001)

[175] F. Grein *J. Phys. Chem. A* **106**, 3823 (2002)

[176] L. A. Carreira and T. G. Towns *J. Mol. Struct.* **41**, 1 (1977)

[177] A. Almenningen, O. Bastiansen, L. Fernholt, B. N. Cyvin, S. J. Cyvin, and S. Samdal *J. Mol. Struct.* **128**, 59 (1985)

[178] O. Bastiansen and S. Samdal *J. Mol. Struct.* **128**, 115 (1985)

[179] G. Celebre, G. de Luca, M. Longeri, C. Veracini, and J. W. Emsley *J. Chem. Soc. Faraday Trans.* **87**, 2623 (1991)

[180] J. W. Emsley, T. J. Horne, G. Celebre, G. de Luca, and M. Longeri *J. Chem. Soc. Faraday Trans.* **88**, 1679 (1992)

[181] M. J. Cook and M. R. Wilson *Molec. Cryst. Liq. Cryst.* **357**, 149 (2001)

[182] M. J. Cook *Computer Simulations of Liquid Crystals* Ph.D. thesis University of Durham (2000)

[183] A. Almenningen, O. Bastiansen, S. Gunderson, S. Samdal, and A. Skancke *J. Mol. Struct.* **128**, 95 (1985)

[184] E. L. Eliel and M. Manoharan *J. Org. Chem.* **46**, 1959 (1981)

[185] K. S. Pitzer *J. Chem. Phys.* **8**, 711 (1940)

[186] D. A. C. Compton, S. Montero, and W. F. Murphy *J. Phys. Chem.* **84**, 3587 (1980)

[187] M. Rasanen and V. E. Bondybey *J. Chem. Phys.* **82**, 4718 (1985)

[188] R. K. Heenan and L. S. Bartell *J. Chem. Phys.* **78**, 1270 (1983)

[189] S. Tsuzukui, T. Uchimaru, and K. Tanabe *Chem. Phys. Lett.* **246**, 9 (1995)

[190] N. L. Allinger, J. T. Fermann, W. D. Allen, and H. F. Schaefer *J. Chem. Phys.* **106**, 5143 (1997)

[191] P. A. Irvine, D. C. Wu, and P. J. Flory *J. Chem. Soc., Faraday Trans. I* **80**, 1795 (1984)

[192] C. L. Yaws *Chemical Properties Handbook* McGraw-Hill, New York (1999)

[193] P. J. Daivis and D. J. Evans *J. Chem. Phys.* **103**, 4261 (1995)

[194] W. L. Jorgensen *J. Am. Chem. Soc.* **103**, 4721 (1981)

[195] W. L. Jorgensen, J. D. Madura, and C. J. Swenson *J. Am. Chem. Soc.* **106**, 6638 (1984)

[196] K. Toriyama and D. A. Dunmur *Molec. Cryst. Liq. Cryst.* **139**, 123 (1986)

[197] D. A. Dunmur and K. Toriyama *Liq. Cryst.* **1**, 169 (1986)

[198] F. M. Leslie *Quart. J. Mech. Appl. Math.* **19**, 357 (1966)

[199] F. M. Leslie *Arch. Ratl. Mech. Anal.* **28**, 265 (1968)

[200] J. L. Ericksen *Arch. Ratl. Mech. Anal.* **23**, 266 (1966)

[201] J. L. Ericksen *Molec. Cryst. Liq. Cryst.* **7**, 153 (1969)

[202] M. G. Clark and F. M. Leslie *Proc. R. Soc. Lond. A* **361**, 463 (1978)

[203] O. Parodi *J. Phys. (Paris)* **31**, 581 (1970)

[204] W. Helfrich *J. Chem. Phys.* **51**, 4092 (1969)

[205] M. Miesowicz *Bull. Acad. Polon. Sci. Lett., Ser. A, Sci. Math.* page 228 (1936)

[206] S. Hess *Flow Properties and Structure of Anisotropic Fluids Studied by Non-Equilibrium Molecular Dynamics, and Flow Properties of Other Complex Fluids: Polymeric Liquids, Ferro-fluids,and Magneto-Rheological Fluids* in *Advances in the Computer Simulation of Liquid Crystals*, editors P. Pasini and C. Zannoni page 189 Kluwer, Dordecht (2000)

[207] F. Schneider and H. Kneppe *Flow Phenomena and Viscosity* in *Physical Properties of Liquid Crystals*, editors D. Demus, J. Goodby, G. W. Gray, H. W. Spiess, and V. Vill page 352 Wiley-VCH, New York (1998)

[208] H. Hirschmann and V. Reiffenrath *TN and STN Displays* in *Handbook of liquid crystals Vol 2A: Low molecular weight liquid crystals I*, editors D. Demus, J. Goodby, G. W. Gray, and V. Vill Wiley-VCH (1998)

[209] D. Demus and G. Pelzl *Zietschrift Chemie* **1**, 21 (1982)

[210] V. Zwetkoff *Acta. Physiochemica URSS* **10**, 555 (1939)

[211] W. H. de Jeu *Physical Properties of Liquid Crystals* Gordon and Breach, New York (1980)

[212] J. Prost and H. Gasparoux *Phys. Lett. A* **36**, 245 (1971)

[213] F. Brouchard, P. Pieranski, and E. Guyon *Phys. Rev. Lett.* **28**, 1681 (1972)

[214] H. Schad *J. Appl. Phys.* **54**, 4994 (1983)

[215] P. E. Cladis *Phys. Rev. Lett.* **28**, 1629 (1972)

[216] P. R. Gerber *Appl. Phys.* **A26**, 139 (1981)

[217] F. J. Bock, H. Kneppe, and F. Schneider *Liq. Cryst.* **3**, 217 (1988)

[218] S. Kuwajima and A. Manabe *Chem. Phys. Lett.* **332**, 105 (2001)

[219] A. Eich, B. A. Wolf, L. Bennet, and S. Hess *J. Chem. Phys.* **113**, 3829 (2000)

[220] S. Sarman *J. Chem. Phys.* **103**, 10378 (1995)

[221] S. Sarman *J. Chem. Phys.* **103**, 393 (1995)

[222] D. J. Evans and G. P. Morriss *Statistical Mechanics of Non-equilibrium Liquids* Academic Press (1990)

[223] D. Forster *Ann. Phys.* **85**, 505 (1974)

[224] S. Sarman and D. Evans *J. Chem. Phys.* **99**, 9021 (1993)

[225] M. A. Osipov and E. M. Terentjev *Z. Naturforsch. Teil. A* **44**, 785 (1989)

[226] M. A. Osipov and E. M. Terentjev *Phys. Lett. A* **134**, 301 (1989)

[227] A. V. Zakharov *Phys. Lett. A* **193**, 471 (1994)

[228] M. Fialkowski *Phys. Rev. E* **58**, 1955 (1998)

[229] A. V. Zakharov, A. V. Komolkin, and A. Maliniak *Phys. Rev. E* **59**, 6802 (1999)

[230] A. V. Zakhorav and R. Y. Dong *Phys. Rev. E* **63**, 011704 (2000)

[231] A. V. Zakharov and A. Maliniak *Eur. Phys. J. E* **4**, 435 (2001)

[232] C. Zannoni *Quantitative Description of Orientational Order: Rigid Molecules* in *Nuclear Magnetic Resonance of Liquid Crystals*, editor J. W. Emsley page 1 Kluwer, Dordecht (1985)

[233] S. Cozzini, L. F. Rull, G. Ciccotti, and G. V. Paolini *Physica A* **240**, 173 (1997)

[234] N. Kirov, I. Dovoz, and M. P. Fontana *J. Chem. Phys.* **83**, 5267 (1985)

[235] U. Finkenzeller, T. Geelhaar, G. Weber, and L. Pohl *Liq. Cryst.* **5**, 313 (1989)

[236] R.Seeliger, H. Haspeklo, and F. Noack *Molec. Phys.* **49**, 1039 (1983)

[237] S.-T. Wu and C.-S. Wu *Phys. Rev. A* **42**, 2219 (1990)

[238] M. R. Wilson *Parallel Molecular Dynamics Techniques for the Simulation of Anisotropic Systems* in *Advances in the Computer Simulation of Liquid Crystals*, editors P. Pasini and C. Zannoni page 389 Kluwer, Dordecht (2000)

[239] P. Procacci and M. Marchi *Multiple Time Step Algorithms for the Atomistic Simulations of Complex Molecular Systems* in *Advances in the Computer Simulation of Liquid Crystals*, editors P. Pasini and C. Zannoni page 333 Kluwer, Dordecht (2000)

[240] R. B. Meyer *Phys. Rev. Lett.* **22**, 918 (1969)

[241] J. Prost and J. P. Marcerou *J. Phys (Paris)* **38**, 315 (1977)

[242] W. Haase, Z. X. Fan, and H. J. Müller *J. Chem. Phys.* **89**, 3317 (1988)

[243] P. Rudquist and S. T. Lagerwall *Liq. Cryst.* **23**, 503 (1997)

[244] L. M. Blinov and V. G. Chigrinov *Electrooptic Effects in Liquid Crystals* Springer, New York (1993)

[245] C. Denniston and J. Yeomans *Phys. Rev. Lett.* **87**, 275505 (2001)

[246] A. J. Davidson and N. J. Mottram *Phys. Rev. E* **65**, 051710 (2002)

[247] J. S. Patel and R. B. Meyer *Phys. Rev. Lett.* **58**, 1538 (1987)

[248] M. Čepič and B. Žekš *Phys. Rev. Lett.* **87**, 085501 (2001)

[249] A. G. Petrov *Biochim. Biophys. Acta* **85535**, 1 (2001)

[250] P. R. M. Murthy, V. A. Raghunathan, and N. V. Madhusudana *Liq. Cryst.* **14**, 483 (1993)

[251] A. G. Petrov *Measurements and Interpretation of Flexoelectricity* in *Physical Properties of Liquid Crystals: Nematics*, editors D. A. Dunmar, A. Fukuda, and G. R. Luckhurst page 251 INSPEC, the Institution of Electrical Engineers, London (2001)

[252] J. P. Straley *Phys. Rev. A* **14**, 1835 (1976)

[253] M. A. Osipov *Sov. Phys. JETP* **85**, 1167 (1983)

[254] M. A. Osipov *J. Phys. Lett* **45**, 823 (1984)

[255] M. A. Osipov and V. B. Nemtsov *Sov. Phys. Crstallogr.* **31**, 125 (1986)

[256] Y. Singh and U. P. Singh *Phys. Rev. A* **39**, 4254 (1989)

[257] A. M. Somoza and P. Tarazona *Molec. Phys.* **72**, 911 (1991)

[258] A. Ferrarini *Phys. Rev. E* **64**, 021710 (2001)

[259] A. V. Zahkarov and R. Y. Dong *Eur. Phys. J. E* **6**, 3 (2001)

[260] G. Z. Zhu, Y. Jin, and J. B. Song *Phys. Lett. A* **109**, 279 (1985)

[261] L. Blinov, D. Z. Radzhabov, S. V. Yablonski, and S. S. Yakovenko *Nuovo Cimento D* **12**, 1353 (1990)

[262] L. M. Blinov, M. I. Barnik, H. Okaha, M. Ozaki, N. M. Shtykov, and K. Yoshino *Eur. Phys. J. E* **4**, 183 (2001)

[263] A. G. Petrov, A. T. Ionescu, C. Versace, and N. Scaramuzza *Liq. Cryst.* **19**, 169 (1995)

[264] I. Dozov, P. Martinot-Lagarde, and G. Durand *J. Phys. Lett. (Paris)* **43**, 365 (1982)

[265] I. Dozov, P. Martinot-Lagarde, and G. Durand *J. Phys. Lett. (Paris)* **44**, 817 (1982)

[266] D. R. Link, M. Nakata, Y. Takanishi, K. Ishikawa, and H. Takezoe *Phys. Rev. E* **65**, 010701 (2002)

[267] J.-P. Marcerou and J. Prost *Molec. Cryst. Liq. Cryst.* **58**, 259 (1980)

[268] M. P. Allen, C. P. Mason, E. de Migeul, and J. Stelzer *Phys. Rev. E* **52**, 25 (1995)

[269] B. Tjipto-Margo, G. T. Evans, M. P. Allen, and D. Frenkel *J. Phys. Chem.* **96**, 3942 (1992)

[270] J. Stelzer, L. Longa, and H.-R. Trebin *J. Chem. Phys.* **103**, 3098 (1995)

[271] J. Stelzer, L. Longa, and H.-R. Trebin *Molec. Cryst. Liq. Cryst.* **262**, 455 (1995)

[272] M. P. Allen, M. A. Warren, M. R. Wilson, A. Sauron, and W. Smith *J. Chem. Phys.* **107**, 2850 (1996)

[273] N. H. Phuong, G. Germano, and F. Schmid *J. Chem. Phys.* **115**, 7227 (2001)

[274] R. Kubo *Rep. Prog. Phys.* **29**, 255 (1966)

[275] J. Prost and P. S. Pershan *J. Appl. Phys* **47**, 2298 (1976)

[276] M. P. Allen and A. J. Masters *J. Mater. Chem* **11**, 2678 (2001)

[277] G. R. Luckhurst *Molecular Field Theories of Nematics* in *Nuclear Magnetic Resonance of Liquid Crystals*, editor J. W. Emsley Kluwer, Dordecht (1985)

[278] D. J. Tildesley and P. A. Madden *Molec. Phys.* **48**, 129 (1983)

[279] A. V. Zakharov *Phys. Rev. E* **51**, 5880 (1995)

[280] A. V. Zakharov and S. Romano *Phys. Rev. E* **58**, 7428 (1998)

[281] A. Derzhanski and A. G. Petrov *Phys. Lett. A* **34**, 483 (1971)

[282] L. M. Blinov, M. Ozaki, and K. Yoshino *JETP Lett.* **69**, 236 (1999)

Appendix A

Conferences, Courses, and Seminars

Conferences

EPS 5th Liquid Matter Conference

University of Konstanz, Germany, 14th-18th September, 2002

Poster presentation: 'Calcaultion of Rotational Viscosity and Flexoelectric Co-efficients of a Nematic Liquid Crystal'.

CCP5 Annula Meeting, Advances in Simulations of Molecules and Materials

University of Durham, UK, 9th-13th September, 2002

Poster presentation: 'Calculation of Rotational Viscosity and Flexoelectric Co-efficients of a Nematic Liquid Crystal'. Poster presentation: 'Paraemterization and Validation of a Force Field for Liquid Crystal Molecules'

International School of Liquid Crystals 9th Workshop, Computational Models of Liquid Crystals and Complex Systems *Erice, Sicily, 13th-18th July, 2002*

Poster presentation: 'Calculation of Rotational Viscosity and Flexoelectric Co-efficients of a Nematic Liquid Crystal'.

International Liquid Crystal Conference

Edinburgh, UK, 30th June-5th July, 2002

Poster presentation: 'Calculation of Rotational Viscosity and Flexoelectric Co-efficients of a Nematic Liquid Crystal'. Poster presentation: 'Parameterization and Validation of a Force Field for Liquid Crystal Molecules'

IoP Workshop Liquid Crystal Colliods

Sheffield Hallam University, UK, xxx th April, 2002

CCP5 Annual Meeting Liquids and Liquid Interfaces

Warwick University, UK, 16th-19th September 2001

Poster presentation: 'Calculation of Rotational Viscosity Co-efficient of a Nematic Liquid Crystal'.

Royal Society of Chemistry Materials Discusion 4: Molecular Topology in Liquid Crystals

Grasmerer, UK, 11th-14th September 2001

Poster presentation: 'Calculation of Rotational Viscosity Co-efficient of a Nematic Liquid Crystal'.

CCP5 Summer School in Methods in Molecular Simulation

UMIST, UK, 1st-7th July, 2001

Poster presentation: 'Calculation of Rotational Viscosity Co-efficient of a Nematic Liquid Crystal'.

British Liquid Crystal Society Annual Conference

University of Oxford, UK, 19th-21st March, 2001

Poster presentation: 'Calculation of Rotational Viscosity Co-efficient of a Ne-

matic Liquid Crystal'. Poster presentation: 'Parameterization and Validation of a Force Field for Liquid Crystal Molecules'

Condensed Matter and Materials Physics 2000

University of Bristol, UK, 19th-21st December 2000

Poster Presentation: 'Combined *Ab Initio* and Molecular Dynamics Studies of Liquid Crystal Fragments'

Britich Liquid Crystal Society Annual Conference

Starthclyde University, UK, 17th-19st March, 2001

Poster Presentation: 'Combined *Ab Initio* and Molecular Dynamics Studies of Liquid Crystal Fragments'

British Liquid Crystal Society Winter Workshop

Hull University, UK, 19th-21st December 1999

Courses

FORTRAN Programming

Information Technology Service, University of Durham

Structure-Property Relationships

Department of Chemistry, University of Durham

Practical Electronic Structure Calculations

Department of Chemistry, University of Durham

Postgraduate Course in Condensed Matter Physics

Department of Physics, University of Durham

Seminars

Covalent Effects in 'Ionic' Systems

Prof. P. A. Madden, Oxford University,8th May 2002

Gas Phase Chemistry and CVD Diamond Growth

Prof. M. Ashcroft, Bristol University, 20th March, 2002

Polymers as Building blocks in Nanotechnology

Dr W. Huck, Cambridge University, 23rd Janurary 2002

Supermolecular Liquid Crystals: Multipodes and Dendrimers

Prof. J. W. Goodby, Hull University, 14th November, 2001

Photonic Crystals

Prof. R. Denning, University of Oxford, 24th October 2001

Towards accurate ab initio electronic structure for large molecules

Prof. P. Knowles, University of Birmingham, 17th October, 2001

Probing Structural Disorder with Diffuse Neutron Scattering

Dr D. Keen, ISIS, Rutherford Appleton Laboratory, 14th March 2001

Modelling Meso- and Molecular Scale Interactions in Polymeric Systems

Prof. A. Balzas, Univ. of Pittsburgh, 28th February 2001

Liquid Crystals of All Shapes and Sizes

Prof. R. Richardson, Bristol University, 21st February 2001,

Distribution of Bonding Energy in Polyatomic Molecules

Dr S. T. Howard, Cardiff University, 14th February 2001

Chemical Integrated Circuits: organic synthesis and analysis on a small scale

Dr A deMello, Imperial College London, 24th Janurary 2001

Application of Polarised NEXAFS Spectroscopy to the Structural Characterisation of Soft Molecular Interfaces

Prof. K. Roberts, Leeds University, 17th January 2001

Cosmic: a universal, DNA-based language for communicating with aliens and other intelligent lifeforms

Dr J. P. L. Cox, Bath Unversity, 8th November 2000

Science, Art, and Drug Discovery: A Personal Perspective

Dr S. F. Campbell, Former Sen. Vice President Pfizer, 25th October 2000

Recent Developments in Organic LED Technology: Organolanthanide Phosphors

Dr V. Christou, Oxford University, 11th October 2000

Joining the Dots- Optoelectronic Devices Using Colliodal Semiconductor Nanocrystals

Dr N. Greenham, Cambrigde University, 10th May 2000

Ultrafast Molecular and Protein Dynamics Seen Through Their Vibrations

Prof. R. Hochstrasser, University of Pennsylvania, 5th May 2000

Computer SImulation of Interfaces: Fact or Friction

Prof. D. J. Tildesley, Unilever, 1st March 2000

Flow of Polymer Blends

Dr N. Clarke, UMIST, 23rd February 2000

Protons in Motion: Neutron Diffraction Studies of Hydrogen Atoms in Organic Crystal Structures

Dr C. Wilson, ISIS, 2nd February 2000

Quantum Evaporation and the Interaction of He Atoms with the Surface of Liquid Helium

Prof. A. F. G. Wyatt, Exeter University, 2nd February 2000

Miniturised Chemical Analysis (Lab on a Chip): Functional or Merely Fasshionable

Dr P. R. Fielden, UMIST, 19th January 2000

Delving into the Structure of Ferroelectric Liquid Crystals

Dr H. Gleeson, Manchester University, 19th January 2000

Improving Organic Light Emitting Diodes by Molecular, Optical and Device Design

Dr I. Samuel, Universiy of Durham, 10th November 1999

Strengths of C-C and C-H Bonds in Organic and Organometalic Molcules: Empirical, Semi-empirical, and *ab initio*Calculations

Prof. D. W. Smith, University of waitikato, 3rd November 1999

Novel Catalysts for Atom Ecomnomic Trnsfers

Dr C. Baddock, Imperial College, 27th October 1999

Nanomagenetism and Quantum Computing

Dr R. Cowburn, Cambridge University, 20th October 1999